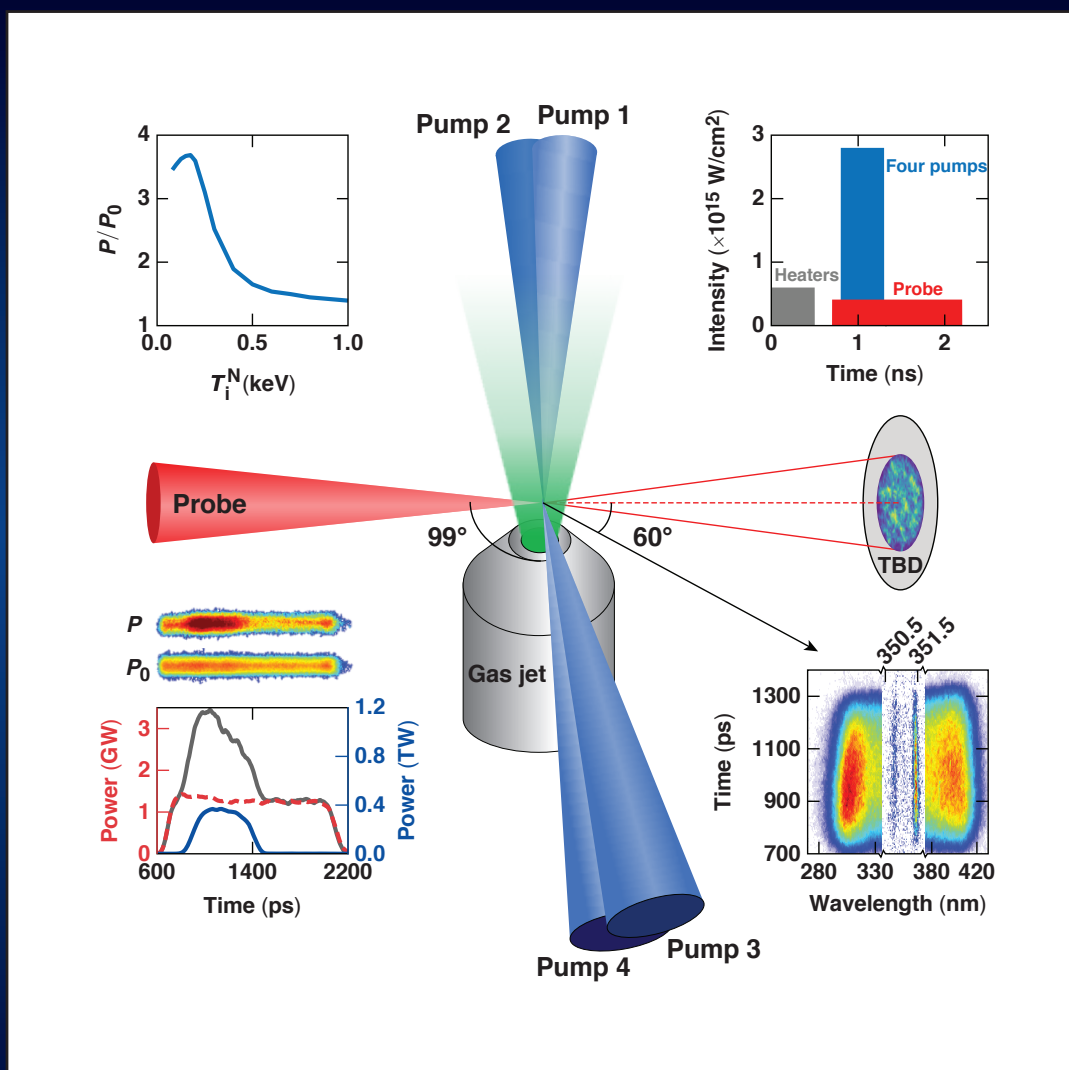# LLE Review

Quarterly Report

UR
LLE
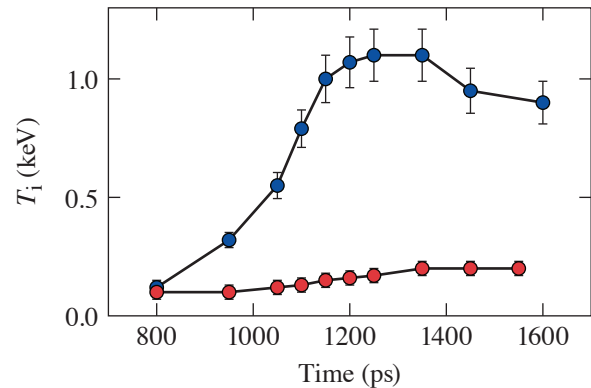
About the Cover:

The cover depicts the experimental configuration used to study cross-beam energy transfer (CBET) saturation on OMEGA. In this setup, several pump laser beams (blue) transfer energy into the tunable Omega Port 9 (TOP9) probe laser (red) by resonantly driving an ion-acoustic wave grating in a gas-jet plasma. The top left figure shows the ratio of the output power (P) to the incident power (P_0) of the probe beam calculated using a linear kinetic CBET model for the conditions of these experiments over a range of nitrogen ion temperatures. The top right figure shows the total laser intensity, pulse shapes, and beam timings for each of the beam groups. The bottom left figure shows the transmitted beam diagnostic data showing the input- (dashed red curve) and output- (solid black curve) probe and pump (solid blue curve) powers. The bottom right figure shows the time-resolved Thomson-scattering spectrum that was used to infer the background plasma conditions.

The figure (right) shows the measured ion temperatures for shots at low and high intensities. For the low-intensity shot (red circles), the ion temperature remained low throughout the experiment, consistent with hydrodynamic predictions. For the high-intensity shot (blue circles), the ion temperature increased during the CBET interaction and the final ion temperature ($T_i \approx 1$ keV) significantly exceeded the electron temperature ($T_e \approx 0.6$ keV). This ion heating is a direct result of energy conservation in the CBET interaction and must be accounted for in hydrodynamic simulations to accurately predict the ion temperature in the presence of significant CBET.

E29632J1

LLE Review

Quarterly Report

UR
LLE

Contents

PUBLICATIONS AND CONFERENCE PRESENTATIONS

In Brief

This volume of LLE Review 165 covers the period from October–December 2020. Articles appearing in this volume are the principal summarized results for long-form research articles. Readers seeking a more-detailed account of research activities are invited to seek out the primary materials appearing in print, detailed in the publications and presentations section at the end of this volume.

Highlights of research presented in this volume include:

- R. S. Craxton *et al.* describe polar-direct-drive exploding-pusher experiments at the National Ignition Facility (NIF). These targets are of interest as high-fluence sources of fusion neutrons (p. 1).

- D. H. Edgell *et al.* report on unabsorbed light measurements on OMEGA implosions using the 3ω gated optical imager diagnostic. The measurements are used to investigate absorption nonuniformity and coronal density profiles (p. 5).

- O. M. Mannion *et al.* use nuclear diagnostics to infer mode-one drive asymmetries in OMEGA implosions imparted by drive-beam mispointing (p. 8). A target offset was introduced to compensate the drive asymmetry and significantly improve hot-spot uniformity.

- J. J. Ruby *et al.* report on a Bayesian inference technique for inferring hot-spot plasma conditions and the corresponding uncertainties using a limited set of known parameters and a simplified physics model (p. 11).

- A. Shvydky *et al.* use density functional theory to calculate more-accurate values for the ionization state and index of re-fraction in the partially ionized material that is released after shock breakout (p. 13). The index of refraction is needed for inferring density profiles from interferograms of shock release taken on OMEGA EP.

- A. M. Hansen *et al.* report on measurements of cross-beam energy transfer saturation resulting from trapping-induced ion heating in TOP9 experiments (p. 16).

- R. K. Follett *et al.* use the *LPSE* code to calculate absolute thresholds for stimulated Raman scattering and two-plasmon decay driven by multiple broadband lasers at conditions relevant to OMEGA- and NIF-scale implosions (p. 19).

- J. Zhang *et al.* develop an analytic approach to calculating the reflection and transmission of light at a temporal boundary inside of a dispersive medium (p. 22).

- L. E. Crandall *et al.* report on equation-of-state measurements of CO_2 up to 800 GPa using laser-driven diamond-anvil-cell targets (p. 26).

- S. X. Hu *et al.* use density functional theory (DFT) calculations to determine stable high-pressure carbonaceous sulfur hydride compounds and to calculate their critical temperature for superconductivity (p. 29). The results are in good agreement with recent observations of room-temperature superconductivity at 270 GPa.

- V. V. Karasiev and S. X. Hu develop a novel free-energy DFT-based methodology for calculating x-ray absorption in warm dense plasmas. The new technique is used to build a first-principles opacity table for use in inertial confinement fusion (ICF) and high-energy–density physics applications (p. 32).

- J. Katz *et al.* build a transmitted beam diagnostic for diagnosing the time-resolved power spectrum of the wavelength-tunable TOP9 beam on OMEGA (p. 35).

- O. M. Mannion *et al.* develop a technique for reconstructing the hot-spot velocity, apparent ion temperature, and areal density in ICF implosions using the various neutron spectrometers on OMEGA (p. 39).

- Z. L. Mohamed *et al.* develop a forward-fitting technique for analyzing neutron time-of-flight data that includes an energy-dependent instrument response function (p. 42).

- M. J. Rosenberg *et al.* describe the progress in developing and implementing the scattered-light time-history diagnostic on the NIF (p. 46). The diagnostic will be deployed at 15 locations around the NIF target chamber for the purpose of measuring scattered light associated with stimulated Brillouin scattering, stimulated Raman scattering, and two-plasmon decay.

- C. Dorrer *et al.* develop a novel two-wavelength phase-matching technique for measuring the deuteration level of partially deuterated KPD crystals (p. 49). Precise knowledge of the deuteration level is required for modeling and optimizing of optical parametric amplifiers.

- I. A. Begishev *et al.* achieve high-efficiency fifth-harmonic generation in large-aperture ADP crystals cooled to 200 K in a two-chamber cryostat (p. 52).

- K. R. P. Kafka *et al.* report on laser-induced–damage testing of silica and hafnia monolayers. A pump-probe configuration is used to show the presence of two different time scales for defect initiation in silica (p. 57).

- J. Puth *et al.* summarize operations of the Omega Laser Facility during the first quarter of FY21 (p. 60).

- G. Pien *et al.* implement the remotePI protocol to allow for continued OMEGA 60 and OMEGA EP shot operations while complying with COVID-19 restrictions (p. 62). Both facilities were able to achieve pre-COVID levels of effectiveness with reduced on-site staffing and without requiring principal investigators to be on site.

Russell K. Follett
Editor

High-Yield Polar-Direct-Drive Fusion Neutron Sources at the National Ignition Facility

R. S. Craxton,[1] C. B. Yeamans,[2] G. E. Kemp,[2] Z. B. Walters,[2] H. D. Whitley,[2] P. W. McKenty,[1] E. M. Garcia,[1] Y. Yang,[1] and B. E. Blue[2]

[1]Laboratory for Laser Energetics, University of Rochester
[2]Lawrence Livermore National Laboratory

Direct-drive implosions at the National Ignition Facility (NIF) that produce high neutron yields from DT-filled targets are of substantial current interest as high-fluence fusion neutron sources. These sources are routinely used for neutron radiation effects experiments in support of programs at the national laboratories. This summary describes the development of these sources, focusing on the target designs and the high-yield experimental results that have been obtained to date.

The targets used for these experiments, typically thin shells of glow-discharge-polymer plastic (CH)[1] filled with DT gas, are sometimes known as "exploding pushers"[2] because they resemble the targets that have consistently been used since the earliest implosions[3] to maximize neutron yield. The earliest targets were irradiated with short pulses of IR laser light that deposited energy largely into energetic electrons. These electrons passed back and forth through the shell, depositing their energy throughout the shell. The shell exploded, causing its inner portion to compress the fuel. Later experiments using UV laser light, including the current experiments, differ in that the shell is ablatively accelerated by the laser, but the shell still decompresses (explodes) as it moves inward, producing high ion temperatures through shock convergence but precluding the high densities needed for ignition. Cryogenic designs, in contrast, provide a path to ignition and gain, but the most convenient source on the NIF of high neutron fluxes is the exploding pusher.

A typical target is shown in Fig. 1(a): a 4-mm-diam, ~25-μm-thick CH shell, filled with 8 atm of DT. Experiments have typically used diameters ranging from 3 mm to 5 mm, depending on the laser energy. The design of an experiment at a given laser energy entails a number of considerations, particularly the 1-D design to optimize the yield and the pointing design to optimize implosion uniformity. The 1-D designs were done using *HYDRA*.[4] Figure 1(b) summarizes the results of thousands of 1-D runs in the form of a contour plot of yield as a function of the shell diameter and thickness for a laser energy of 585 kJ. The optimum design calls for a diameter of 3 mm and a thickness of 18 μm, the parameters of the shot known as "Little Guy." Targets that are too thin or have a diameter that is too small are fully imploded before all of the laser energy can be delivered. Targets in the upper-right quadrant are too massive to be accelerated sufficiently with the available laser energy. The hatched region represents targets that are too thin to reliably hold the 8-atm fill pressure.

The pointing designs were done using the 2-D hydrodynamics code *SAGE*, which includes a 3-D ray-tracing capability.[5] The need for beam pointing optimization arises because the NIF beams (grouped into 48 quads) are located in four rings in each hemisphere at angles ranging between 23.5° and 50° from the vertical axis. Most of the beams must be repointed toward the equator in order to provide close-to-uniform drive at all angles on the surface of the target, a concept known as polar direct drive.[6] The problem is complex because the best-focus phase-plate spot profiles, chosen to meet the requirements of indirect-drive designs, are different in size and shape for each ring of beams. The beams also need to be defocused so that their focal spots better match the target diameter, especially for the larger targets. It was shown in Ref. 7 that reasonable implosion uniformity can be achieved using the indirect-drive phase plates by a combination of appropriate repointings and beam-defocus distances.

(a)

(b) Contours: yield/10^{16}
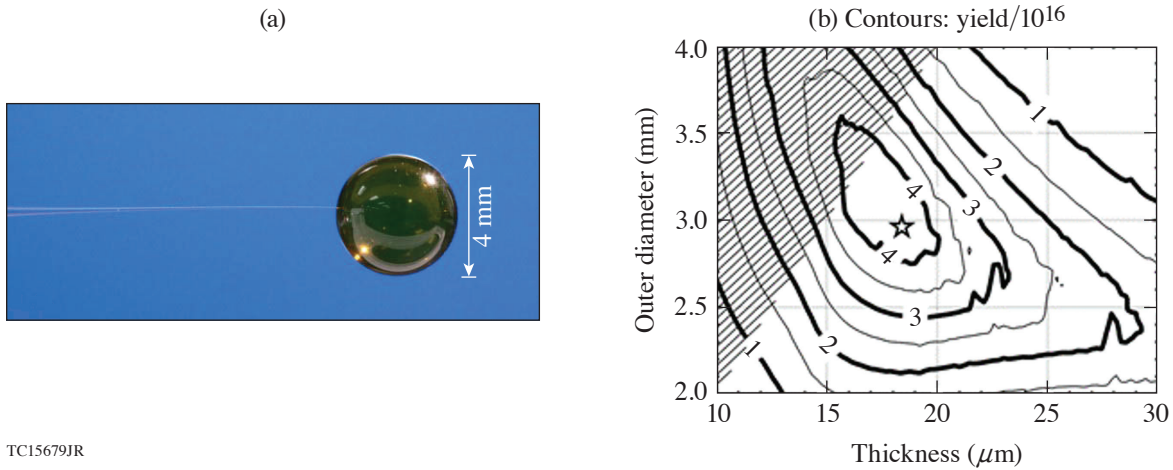
TC15679JR

Figure 1

(a) A typical 4-mm-diam plastic target supported by a glass microcapillary fill-tube stalk. (b) Contour plot of neutron yield as a function of target thickness and diameter, based on a large number of 1-D simulations using the code *HYDRA*. This scan was done for a laser pulse delivering 585 kJ; the optimum parameter combination, indicated by the star, was used for the "Little Guy" shot.

Combining its 2-D hydrodynamics with its 3-D ray trace, *SAGE* is able to predict the 3-D implosion uniformity pattern over the target surface. Figure 2 is a contour plot of the deviation from the mean of the center-of-mass radius of the imploding shell, with red indicating overdriven and blue underdriven. The plot also shows the locations of the 192 beam ports (green squares) and their aim points (black circles) on the target surface. The rms deviation is just 20.5 μm after the shell has imploded 923 μm, corresponding to a 2.22% nonuniformity in the distance traveled, or equivalently in the average velocity. This is made up of a quadrature sum of 1.23% in the θ direction and 1.85% in the azimuthal (φ) direction, illustrating the importance of spreading the beams appropriately in the azimuthal direction.
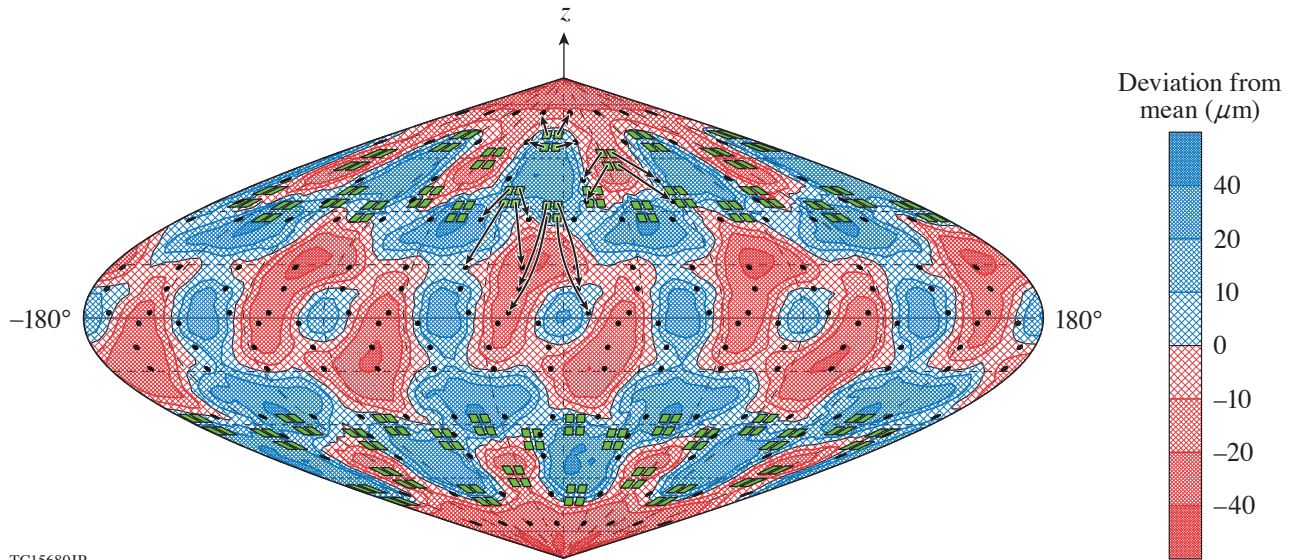
TC15680JR

Figure 2

Contour plot, relative to the spherical coordinate angles (θ,φ), of the deviation from the mean of the center-of-mass radius of a 4-mm-diam plastic target after implosion through 923 μm, predicted using the code *SAGE*. The plot shows that the average velocity variation over the sphere is 2.22% rms, the quadrature sum of 1.23% in the θ direction and 1.85% in the φ direction. The green squares indicate the 192 NIF beams, the black circles their aim points, and the arrows the beam repointings in θ and φ.

Experimental results for the neutron yield are shown in Fig. 3. Neutron images viewing in the polar and equatorial directions are given in Figs. 3(a) and 3(b), respectively, for Little Guy. The images are approximately round, indicating very acceptable uniformity. Figure 3(c) gives a compilation of the yields obtained on a large number of shots, including direct-drive shots using 3-mm- and 4-mm-diam CH shells and some (at lower energy) using ~2-mm-diam SiO_2 shells. The highest yields come from indirect-drive cryogenic targets close to the nominal 1.8-MJ NIF energy. However, the direct-drive targets provide significantly higher neutron fluxes: test objects can be placed much closer to the source because of the decrease in debris load from the much smaller target vaporized mass.[8] In addition, the direct-drive targets are non-cryogenic and therefore much simpler to field.

Basic parameters and yield results are given in Table I for the three particularly noteworthy shots highlighted in Fig. 3. Little Guy, a 3-mm target, produced 4.81×10^{15} neutrons at an energy of 585 kJ that was low enough to incur no damage to NIF optics. "Orange," an optimized 4-mm target driven by 1.1 MJ, produced 1.11×10^{16} neutrons with an efficiency (fusion energy divided by incident laser energy) of 2.85%, the yield scaling with energy from OMEGA experiments according to the predictions of

TC15681JR
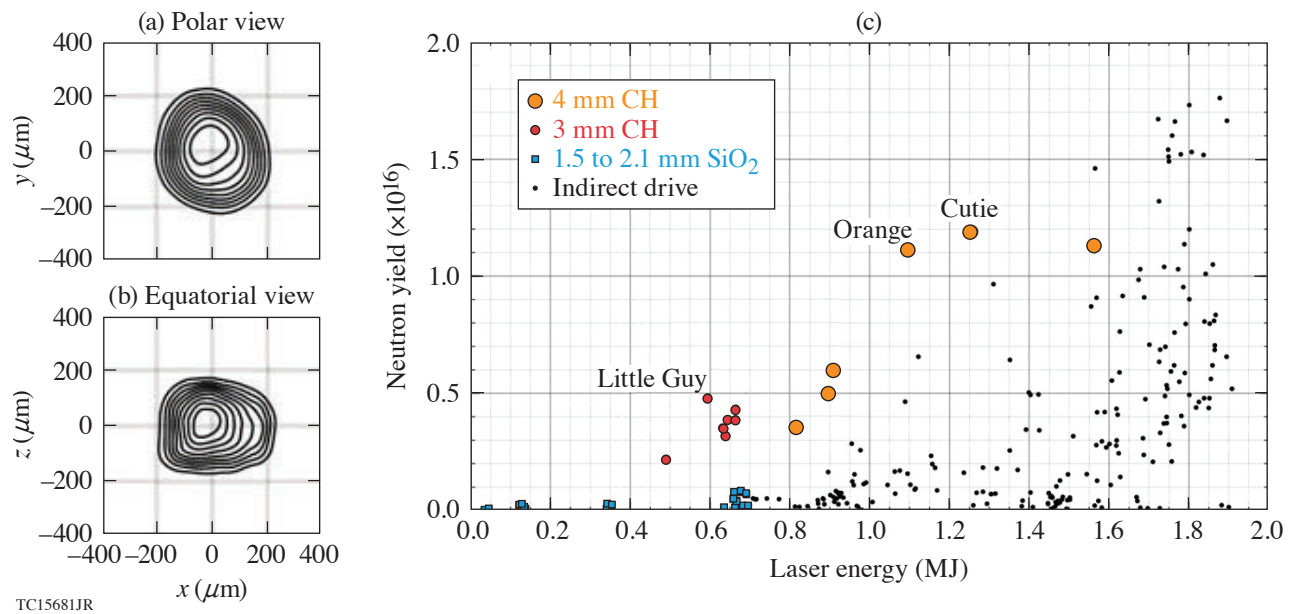
Figure 3
[(a),(b)] Experimental time-integrated neutron images at 10-μm resolution of the 3-mm Little Guy target, with contours in units of 10% of the peak intensity. (c) Yield from a variety of NIF neutron sources (through October 2020) as a function of target energy. Details of the three labeled shots are given in Table I.

Table I: Selected parameters of three NIF shots of particular interest. Each target is filled with 8 atm of DT (~64% D).

		Little Guy	Orange	Cutie
	NIF shot	N190707-001	N190227-001	N191027-003
Capsule	Outer radius (μm)	1480	1971	1978
	Thickness (μm)	18.4	25	22.7
Laser	Laser energy (kJ)	585	1097	1256
	Peak power (TW)	328	390	425
Results	Yield (#DT neutrons)	4.81×10^{15}	1.11×10^{16}	1.19×10^{16}
	Fusion conversion efficiency G_L	2.28%	2.85%	2.67%
	Ion temperature (keV)	11.14	8.94	10.22

Ref. 7. "Cutie," a little thinner than Orange and irradiated with a higher peak power, was somewhat overdriven and produced a slightly higher yield with lower efficiency. All three targets produced high ion temperatures of ~10 keV, measured by four neutron time-of-flight detectors with different viewing angles.[9] Further information on this work can be found in Ref. 10. Work on the modeling of these targets is in progress and will be reported elsewhere.

This platform is being routinely used for neutron effects experiments. Further work on platform development is focused on optimizing designs that deliver the full NIF energy to larger targets subject to the maximum power constraints of the NIF.

1. A. Nikroo *et al.*, Fusion Sci. Technol. **41**, 214 (2002).

2. M. D. Rosen and J. H. Nuckolls, Phys. Fluids **22**, 1393 (1979).

3. G. Charatis *et al.*, in *Plasma Physics and Controlled Nuclear Fusion Research 1974* (IAEA, Vienna, 1975), Vol. II, pp. 317–335.

4. M. M. Marinak *et al.*, Phys. Plasmas **8**, 2275 (2001).

5. R. S. Craxton and R. L. McCrory, J. Appl. Phys. **56**, 108 (1984).

6. S. Skupsky *et al.*, Phys. Plasmas **11**, 2763 (2004).

7. A. M. Cok, R. S. Craxton, and P. W. McKenty, Phys. Plasmas **15**, 082705 (2008).

8. N. D. Masters *et al.*, J. Phys.: Conf. Ser. **717**, 012108 (2016).

9. V. Yu. Glebov *et al.*, Rev. Sci. Instrum. **81**, 10D325 (2010).

10. C. B. Yeamans *et al.*, Nucl. Fusion **61**, 046031 (2021).

Unabsorbed Light Beamlets for Diagnosing Coronal Density Profiles and Absorption Nonuniformity in Direct-Drive Implosions on OMEGA

D. H. Edgell, A. M. Hansen, J. Katz, D. Turnbull, and D. H. Froula

Laboratory for Laser Energetics, University of Rochester

Laser-direct-drive implosions require spherically symmetric compression to avoid low-mode asymmetries and hydrodynamic instabilities.[1,2] Absorption efficiency is known to be severely degraded by cross-beam energy transfer (CBET),[3,4] and scattered-light observations with the diagnostic described in this summary have revealed significant asymmetry during OMEGA implosions. The most-direct diagnostic for laser absorption is the light scattered from the implosion. Isolating the unabsorbed light from each individual OMEGA beam using the 3ω gated optical imager (GOI) diagnostic[5] has facilitated our understanding of the effect that CBET and other physics have on absorption.

The imaged scattered light appears as a pattern of distinct spots, each corresponding to a single beam (Fig. 1). Each spot can be thought of as the end of a "beamlet"—a small component of the beam originating from a specific point in the beam's far-field spatial profile and following a path through the plasma determined by refraction. The intensity of the beamlet varies along its path due to absorption and CBET until it exits the plasma and ultimately reaches the diagnostic. An important component of the 3ω GOI is a Wollaston prism that splits the collected light into orthogonal polarization components, resulting in two separate beamlet spot images at every camera exposure time.

E29422JR
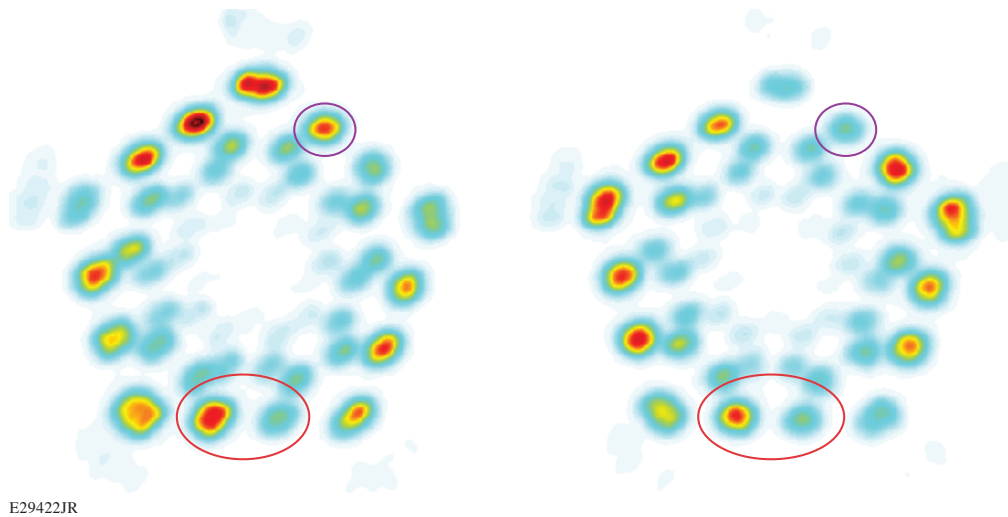
Figure 1
3ω GOI beamlet images collected during an OMEGA implosion for two orthogonal polarizations. The magenta circles highlight a beamlet that is strongly polarized. The red ovals highlight two beamlets that are in the same angular group but clearly have much different intensities.

In a symmetric implosion, all beamlets collected from beams at the same angular distance from the diagnostic should have traveled equivalent paths. With polarization smoothing, each beamlet in the group will have identical CBET and absorption along their paths. All spots in the group are expected to have similar intensities and be equally split between the two orthogonal polarization sub-images. Diagnostic images show that neither of these assumptions is true (Fig. 1). Nonuniformities in the scattered light from an implosion suggest that corresponding nonuniformities may occur in the laser absorption that could severely impact implosion performance. The nonuniformity is believed to be a result of the effect of CBET on the polarization smoothing method used by OMEGA.[6]

The positions of the beamlet spots in the images are determined by the refraction of each beamlet though the plasma and can be used as a density profile diagnostic. In Figs. 2(a)–2(c), the measured beamlet radii are compared to predictions using ray tracing through density profiles calculated by the *LILAC* code using three different physics models. The outer spot positions are most sensitive to the model used. The flux-limited no-CBET[7] model does not predict spot locations for the outer beam groups similar to those measured [Fig. 2(a)]. The Goncharov nonlocal electron transport model[8] is better at predicting the actual spot positions [Fig. 2(b)], and the match is further improved [Fig. 2(c)] when a CBET model is included. Least-square fitting of the density profile was performed to find the best fit to the measured spot positions and to gain further insight into the accuracy of the density profile modeling. The best fits suggest that even the Goncharov/CBET model underpredicts the plasma density farther out in the corona [Fig. 2(d)].
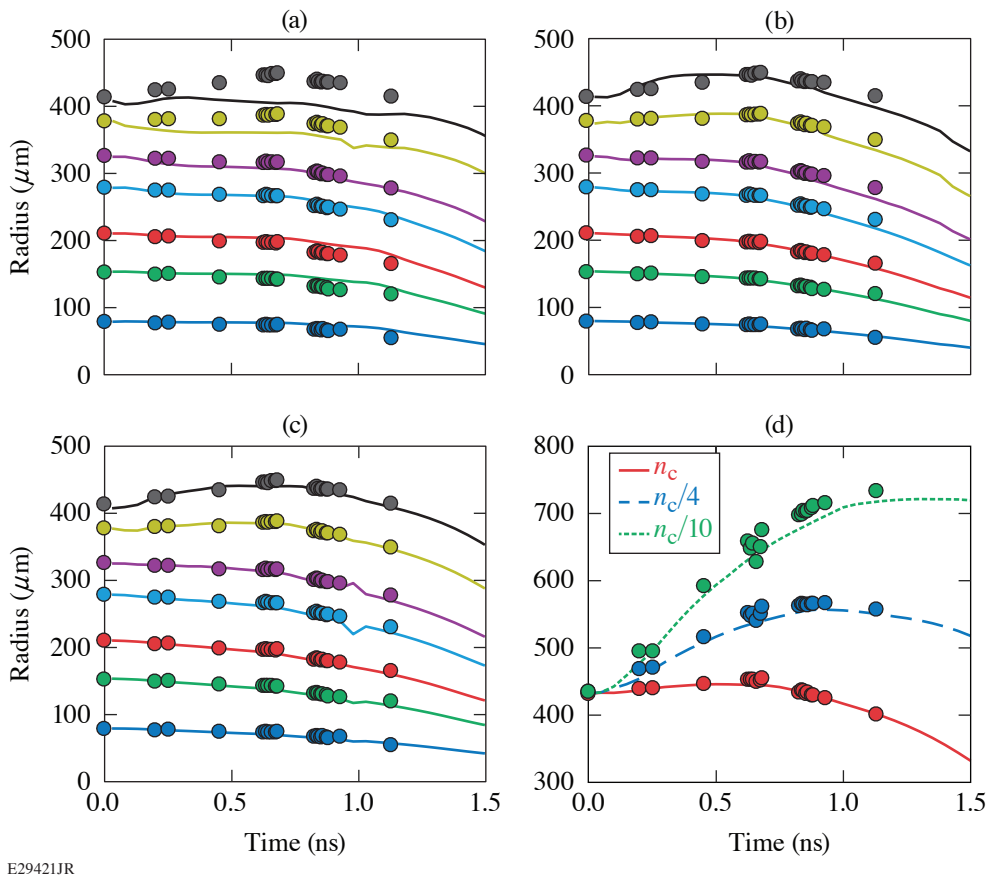
E29421JR

Figure 2

A comparison between the measured beamlet radii (circles, each beam group in a different color) and the predictions using ray tracing through the coronal plasma density profiles (curves) predicted using different physics models: (a) flux-limited ($f = 0.06$) electron heat transport, no CBET; (b) Goncharov nonlocal electron heat transport, no CBET; and (c) Goncharov nonlocal electron heat transport with CBET. (d) Predictions using the same model as in (c) for the time-varying positions of the plasma critical density (n_c) radius, along with the $n_c/4$ and $n_c/10$ surfaces (curves). The circles show the surface radii given by a best fit to the actual measured spot positions.

The 3ω GOI diagnostic was used in conjunction with the wavelength-tunable TOP9 laser[9] to measure the effect of wavelength detuning on CBET.[10] TOP9 appears in the 3ω GOI image as an additional spot. The intensity of the TOP9 beamlet depends strongly on CBET with the other beams. Shifting the TOP9 wavelength with respect to the OMEGA beams alters the magnitude (and even the direction) of energy exchange between TOP9 and the other OMEGA beams. Figure 3(a) shows the predicted TOP9 beamlet intensity versus the wavelength detuning (solid red curve). The measured TOP9 beamlet intensity [Fig. 3(a), magenta circles] supports these predicted trends in general but not in all of the specific details. Since polarization smoothing was used on TOP9, the beamlet polarization was predicted to always be at 45°, but the measurements show significant polarization variation [Fig. 3(b)]. Like the implosion nonuniformity discussed above, these discrepancies may be due to the polarization smoothing method used on OMEGA.

E29461JR
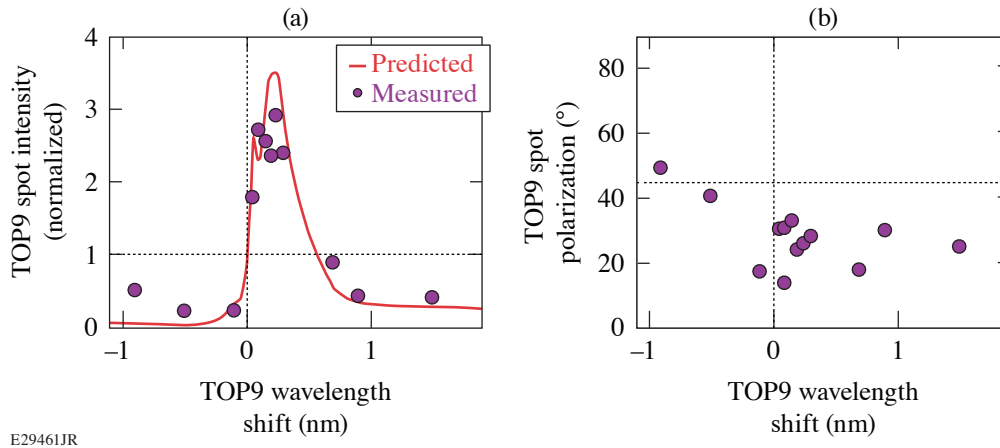
Figure 3

(a) Intensity of the TOP9 beamlet and (b) polarization of the TOP9 beamlet versus the wavelength shift of the TOP9 beam with respect to the 60 OMEGA beams. Predicted intensity was normalized to the intensity when $\Delta\lambda = 0$ and the uncalibrated measured intensity is arbitrarily scaled to match the predicted range.

1. S. E. Bodner *et al.*, Phys. Plasmas **5**, 1901 (1998).

2. S. Skupsky and R. S. Craxton, Phys. Plasmas **6**, 2157 (1999).

3. W. L. Kruer *et al.*, Phys. Plasmas **3**, 382 (1996).

4. C. J. Randall, J. J. Thomson, and K. G. Estabrook, Phys. Rev. Lett. **43**, 924 (1979).

5. D. H. Edgell *et al.*, Rev. Sci. Instrum. **89**, 10E101 (2018).

6. D. H. Edgell *et al.*, "Low-Mode Asymmetry due to Polarization Smoothing in OMEGA Implosions," to be submitted to Physical Review Letters.

7. R. C. Malone, R. L. McCrory, and R. L. Morse, Phys. Rev. Lett. **34**, 721 (1975).

8. V. N. Goncharov *et al.*, Phys. Plasmas **15**, 056310 (2008).

9. B. E. Kruschwitz *et al.*, Proc. SPIE **10898**, 1089804 (2019).

10. D. H. Edgell *et al.*, Phys. Plasmas **24**, 062706 (2017).

Mitigation of Mode-One Asymmetry in Laser-Direct-Drive Inertial Confinement Fusion Implosions

O. M. Mannion,[1] I. V. Igumenshchev,[1] K. S. Anderson,[1] R. Betti,[1] E. M. Campbell,[1] D. Cao,[1] C. J. Forrest,[1] M. Gatu Johnson,[2] V. Yu. Glebov,[1] V. N. Goncharov,[1] V. Gopalaswamy,[1] S. T. Ivancic,[1] D. W. Jacobs-Perkins,[1] A. Kalb,[1] J. P. Knauer,[1] J. Kwiatkowski,[1] A. Lees,[1] F. J. Marshall,[1] M. Michalko,[1] Z. L. Mohamed,[1] D. Patel,[1] H. G. Rinderknecht,[1] R. C. Shah,[1] C. Stoeckl,[1] W. Theobald,[1] K. M. Woo,[1] and S. P. Regan[1]

[1]Laboratory for Laser Energetics, University of Rochester
[2]Plasma Science and Fusion Center, Massachusetts Institute of Technology

Mode-one ($\ell = 1$) asymmetries have been identified as one of the most detrimental to inertial confinement fusion implosion performance[1] and have been observed in laser-indirect-drive implosions at the National Ignition Facility.[2] Mode-one asymmetries can be described as those asymmetries that cause the initial radial implosion velocity of the shell to have the form $v_r(\theta) = v_0 - \Delta v \cos(\theta)$, where v_0 is the average implosion velocity, Δv is the variation in the implosion velocity, and θ is the angle between the mode-one direction and a direction on the target. As the target implodes, this asymmetry causes the formation of a jet within the hot spot.[1] This jet undergoes a Helmholtz instability, which results in the formation of vortices within the hot spot and an asymmetric fuel areal density around the hot spot. The asymmetric fuel distribution leads to poor confinement of the hot spot, while the motion within the hot spot represents residual kinetic energy not used to heat and compress the target.[1] The poor confinement and residual kinetic energy present in the target result in a severe reduction in the fusion yield of the implosion.

To diagnose mode-one asymmetries in laser-direct-drive (LDD) implosions performed on the OMEGA laser, 3-D nuclear and x-ray diagnostics have been developed.[3–5] Neutron time-of-flight (nTOF) and charged-particle spectrometers are used to measure the neutron energy spectrum emitted from the target from which the fusion yield, hot-spot velocity, apparent ion temperature, and fuel areal density are inferred. X-ray imaging diagnostics are used to measure the x-ray self-emission from the hot spot and to infer the size and shape of the hot spot. These diagnostics have been fielded strategically around the OMEGA target chamber to provide a set of 3-D measurements of the hot spot and fuel conditions near peak compression. Using measurements from these diagnostics, the magnitude and direction of mode-one asymmetries are determined.

Measurements made with these detectors have revealed that large mode-one drive asymmetries can be introduced when laser-alignment errors exist. For the experiments described below, defects in the targets used for laser alignment result in the OMEGA Laser System having abnormally large laser-alignment errors. In particular, the aluminum oxide coating on the target used during the laser-alignment process had unintentional coating defects, which caused gross mispointing of the laser beams to be introduced. Furthermore, the Au spheres used during the laser-pointing procedure for these experiments had unintentional nonuniform Au coatings as a result of target fabrication issues. The nonuniform Au coating resulted in weak x-ray signals being generated by specific beams. The weak signals led to large uncertainties in identifying the position of these beams and resulted in large beam-pointing errors being introduced during the beam-pointing procedure. The compounding errors in the alignment of the laser system during these experiments resulted in a large laser mode-one asymmetry being present.

Figure 1(a) shows the laser illumination perturbation on target for shot 94712. The laser illumination on target was determined from a hard sphere calculation, which determines the overlap intensity of all 60 beams on the initial target radius, accounting for the laser beam pointing, laser beam energy, and target offset. The laser beam pointing was determined during the beam-alignment procedure prior to the shot, the laser beam energy was measured using a calorimeter, and the target offset was measured by both

(a) Shot 94712 (b) Shot 94715

Illumination perturbation (%)

E29543JR
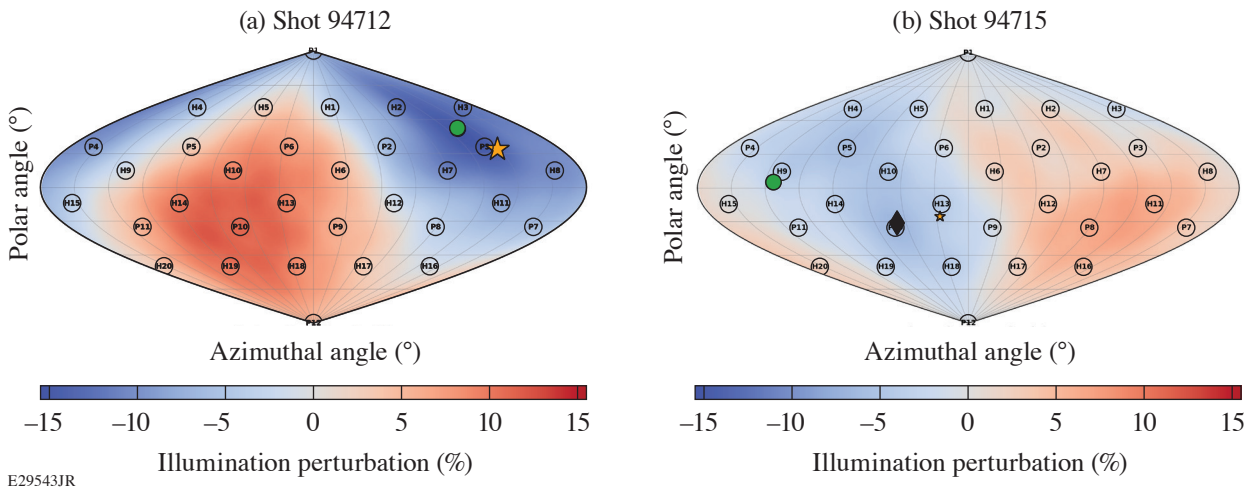
Figure 1

A sinusoidal projection of the OMEGA target chamber showing the illumination perturbation from the mean for (a) shot 94712 and (b) shot 94715 determined from a hard sphere calculation that used the measured laser beam pointing, energy, and target offset. The direction of the measured hot-spot velocity is shown as the orange star and had a magnitude of 146 km/s for shot 94712 and 27 km/s for shot 94715. The laser mode-one illumination asymmetry σ_{rms} amplitude was 7.3% for shot 94712 and 4.3% for shot 94715; the directions are shown as the green circles. The target offset correction for shot 94715 was 43 μm and is shown as the black diamond.

a high-speed video camera and an x-ray pinhole camera. For this experiment, the target offset was <5 μm and nonuniformities in the individual laser beam energies did not contribute significantly to the on-target illumination nonuniformity, which was dominated by the beam-pointing errors. The calculated on-target illumination nonuniformity shows a large mode-one drive asymmetry present with a total peak to valley variation of 27.3% across the target and a mode-one illumination asymmetry σ_{rms} amplitude of 7.3% in the direction $\theta = 51°$ and $\phi = 122°$.

This initial drive asymmetry in the laser resulted in a strong mode-one being present in the experiment, which was observed in both the nuclear and x-ray diagnostics. A hot-spot velocity of 146±12 km/s was inferred from the nTOF's in the direction $\theta = 64±7°$ and $\phi = 133±4°$. The apparent ion temperature asymmetry was 1.8±0.5 keV as measured from the nTOF detectors and the areal-density asymmetry was 104±18 mg/cm^2 as measured by the nTOF and magnetic recoil spectrometer detectors. The direction of the hot-spot velocity, apparent ion temperature asymmetry, and areal-density asymmetry were all aligned with the initial mode-one drive asymmetry identified in the laser. Furthermore, the mode-one asymmetry was observed in the x-ray self-emission images shown in Fig. 2.

Relative x-ray intensity (arbitrary units)
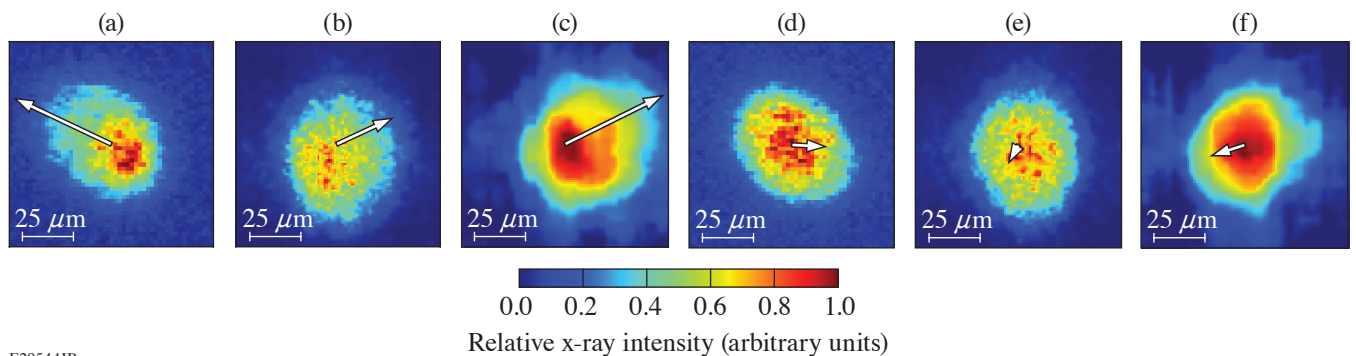
E29544JR

Figure 2

X-ray self-emission images measured for [(a)–(c)] shot 94712 and [(d)–(f)] shot 94715. The [(a) and (d)] single-line-of-sight time-resolved x-ray imager and [(b) and (e)] KBframed images are time resolved and averaged over a 40- and 15-ps time window around peak neutron production, respectively. The [(c) and (f)] gated monochromatic x-ray image is time integrated. The projection of the measured hot-spot velocity onto the detector plane is indicated by the white arrow. The magnitude of the projection is indicated by the length of the arrow. The elongation observed in the x-ray images from shot 94712 has been eliminated by applying the offset correction on shot 94715.

With the mode-one asymmetry characterized on shot 94712, we used a mitigation strategy that employed an intentional target offset to compensate for the observed asymmetry. When a target offset is present in an experiment, it results in a geometric redistribution of the beam overlap intensity on the target and can be used to mitigate mode-one drive asymmetries present in the laser. To determine the appropriate target offset required to mitigate a given mode-one observed on shot 94712, the measured hot-spot velocity was used. The hot-spot velocity $\vec{u}_{hs}$ is assumed to have a linear relationship with the target offset $\vec{o}$ and is given by

$$\vec{u}_{hs} = \alpha \vec{o} = \alpha(\vec{r} + \vec{c}), \tag{1}$$

where α is the offset-to-velocity conversion in km/s/μm, and the total offset is assumed to be the sum of the measured offset $\vec{r}$ from the high-speed video camera and some unknown effective target offset $\vec{c}$. The unknown effective target offset is the component of the hot-spot velocity generated from an assumed static mode-one present in the laser.

These calculations were performed using the results from the experiments discussed above, and the target was positioned to the calculated location to eliminate the mode-one asymmetry. The offset-to-velocity conversion for these experiments was found to be 4.1±0.2 km/s/μm. The unknown effective target offset was determined to be $\vec{c} = \langle -26, 33, 17 \rangle \, \mu$m. This corresponds to a total target offset of 45 μm in the direction $\theta = 112°$ and $\phi = 308°$. For shot 94715, the target was positioned at $\vec{r} = \langle 28, -35, -19 \rangle \, \mu$m, which was within a few microns away from the requested location of $\langle 26, -33, -17 \rangle \, \mu$m. With the target positioned to this location, the asymmetry present in the previous experiments was greatly mitigated. In particular, the hot-spot velocity was reduced to 27±11 km/s in the direction $\theta = 109±35°$ and $\phi = 341±26°$ and is shown in Fig. 1(b). The apparent ion-temperature asymmetry was greatly reduced to 0.5±0.5 keV and the areal-density asymmetry was reduced to 37±12 mg/cm^2. Finally, the hot-spot x-ray self-emission images were found to be significantly more symmetric with the mode-one mitigation and are shown in Fig. 2.

To understand how this target-offset correction was able to mitigate the mode-one asymmetry, it is instructive to analyze the hard sphere illumination nonuniformity for shot 94715. Figure 1(b) shows that when the target correction was applied, the on-target illumination uniformity was improved by a factor of 2 as compared to shot 94712. In particular, the total peak-to-valley variation around the target was reduced to 14%. This technique therefore is a viable mitigation strategy for LDD implosions that have large mode-one drive asymmetries.

1. B. K. Spears *et al.*, Phys. Plasmas **21**, 042702 (2014).
2. H. G. Rinderknecht *et al.*, Phys. Rev. Lett. **124**, 145002 (2020).
3. O. M. Mannion *et al.*, Nucl. Instrum. Methods Phys. Res. A **964**, 163774 (2020).
4. F. J. Marshall *et al.*, Rev. Sci. Instrum. **88**, 093702 (2017).
5. W. Theobald *et al.*, Rev. Sci. Instrum. **89**, 10G117 (2018).

High-Energy-Density–Physics Measurements in Implosions Using Bayesian Inference

J. J. Ruby,[1,2] J. A. Gaffney,[3] J. R. Rygg,[1,2,4] Y. Ping,[3] and G. W. Collins[1,2,4]

[1]Department of Physics and Astronomy, University of Rochester
[2]Laboratory for Laser Energetics, University of Rochester
[3]Lawrence Livermore National Laboratory
[4]Department of Mechanical Engineering, University of Rochester

Convergent high-energy-density experimental platforms are used to study matter under some of the most extreme conditions that can be produced on Earth, comparable to the interior of stars. There are many challenges in using these systems for fundamental measurements currently being addressed by new analysis methods, such as the combination of a reduced-physics model and Bayesian inference,[1,2] allowing for a self-consistent inference of physical quantities with a robust error analysis. These methods in combination with simple [as compared to inertial confinement fusion (ICF)] implosion platforms, which can be modified to show sensitivity to different physical mechanisms of interest, can be used to study the physical properties of matter under extreme conditions and analysis.

One example of simplified implosion designs includes shock-dominated systems, such as thin-shelled, gas-filled targets sometimes known as "exploding pushers" and solid-sphere targets, while another includes thick-shelled, gas-filled implosions that create a compressive hot spot much like modern ICF experiments but at lower convergence ratios for high stability. These systems are able to access different regimes where different physical mechanisms are most relevant.

This work discusses these different regimes and gives a detailed example of an experimental design of a thick-shelled implosion informed by Bayesian inference. A reduced-physics model informed by many of the previously published hot-spot models in literature[3,4] is constrained by a suite of synthetic measurements generated from a *LILAC* simulation using Bayesian inference. (*LILAC* is a radiation-hydrodynamics code.)

The reduced model parameterizes the hot spot in terms of the time history of the total internal energy and the trajectory of the outer edge of the hot spot (in this case defined by the fuel–shell interface) while assuming an isobaric hot spot. This parameterization is used in combination with boundary conditions for the temperature profiles, an ideal gas equation of state, and a Spitzer-like conductivity of the form

$$\kappa = \kappa_0 \left(\frac{\rho}{\rho_0}\right)^a \left(\frac{T}{T_0}\right)^b,$$ (1)

where κ is the thermal conductivity, κ_0 is a constant factor, ρ is the mass density, T is the temperature, and both a and b are constant exponents that define the conductivity response to temperature and density. Using this conductivity along with conservation relations and the equation of state results in a radial temperature profile that depends on the quantity $(1 + b - a)^{-1}$, meaning that the details of the temperature profile provide information on the thermal conductivity of the hot-spot plasma.

Three key details determine the efficacy of this process: (1) The full-physics model being used (in this case *LILAC*) is able to reasonably represent the experimental system; (2) the reduced-physics model accurately represents quantities of interest from the full-physics model; and (3) the reduced-physics model can be constrained by the available measurements. The (synthetic) measurements used in this work include x-ray framing camera measurements, x-ray temporal histories in different spectral channels, the neutron temporal history, and the neutron spectrum.

Figure 1 shows the inferred profiles informed by all of the above measurements compared to the underlying truth from *LILAC*, showing that the thermodynamic conditions within the hot spot can be reconstructed using readily available measurements, assuming that a 1-D model is appropriate to describe the system, i.e., the system is sufficiently stable that asymmetries are not a significant perturbation on the conditions.
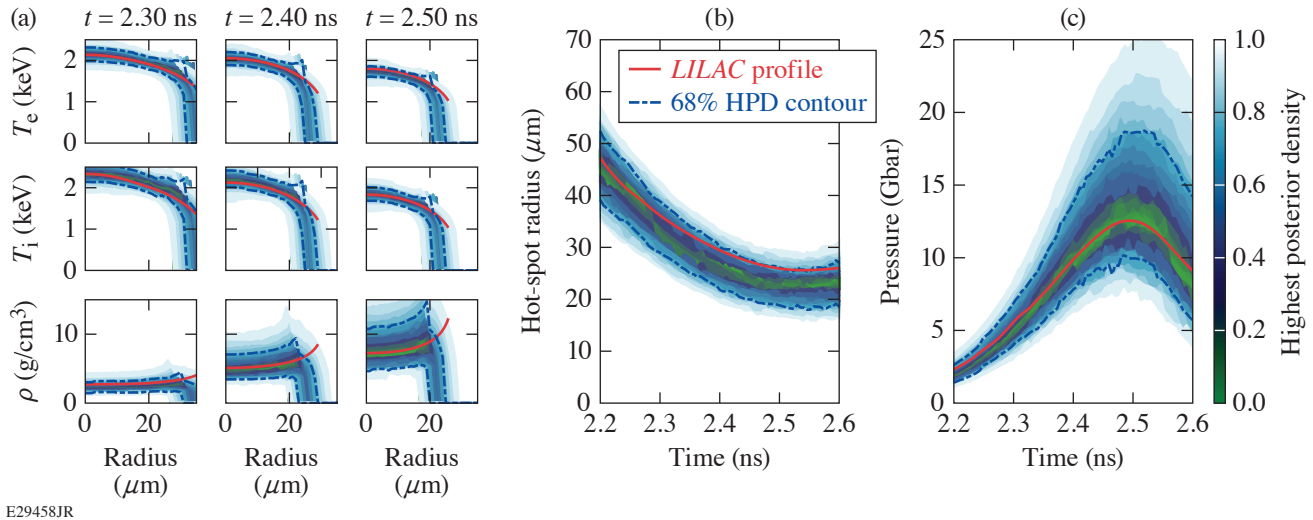
E29458JR

Figure 1

The inferred profiles for (a) the radial distribution of electron temperature, ion temperature, and mass density at three different times around peak emission; (b) the temporal history of the hot-spot radius; and (c) the temporal history of the hot-spot pressure. The color map shows the highest posterior density intervals for the inferred profiles, essentially producing credible intervals where the dashed blue line represents the 68.7% credible interval. The solid red curve shows the profile from the underlying *LILAC* simulation used to generate the synthetic diagnostics. In all cases the profiles are in excellent agreement with the underlying simulation with the exception of the edges of the hot spot where the radius is underpredicted by about 10% at later times, likely due to the fact that there is very little emission coming from the edge of the hot spot and therefore little information about its location. HPD: highest posterior density.

1. J. J. Ruby *et al.*, Phys. Rev. E **102**, 053210 (2020).
2. J. J. Ruby *et al.*, Phys. Rev. Lett. **125**, 215001 (2020).
3. R. Betti *et al.*, Phys. Plasmas **9**, 2277 (2002).
4. P. T. Springer *et al.*, Nucl. Fusion **59**, 032009 (2019).

Ionization State and Dielectric Constant in Cold Rarefied Hydrocarbon (CH) Plasmas of Inertial Confinement Fusion

A. Shvydky, A. V. Maximov, V. V. Karasiev, D. Haberberger, S. X. Hu, and V. N. Goncharov

Laboratory for Laser Energetics, University of Rochester

Inertial confinement fusion (ICF) has been an active field of research for more than 50 years because of its application as a future energy source. In laser-driven ICF, a cryogenically cooled, thin spherical shell of deuterium–tritium (DT) fuel is imploded and compressed by material ablation to form a high-density confinement around a central core where the conditions for thermonuclear ignition can be created. During the implosion, the ablation pressure launches multiple shocks through the DT shell and accelerates it inward. Later, the buildup of pressure in the compressing vapor region decelerates the shell and, at stagnation, creates the conditions in the central core closest to ignition. The pressure buildup and the temperature and density in the core at stagnation are strongly affected by the amount of material that is released from the shell into the vapor region during the implosion.

It is very challenging to measure the material released from the inner surface of the shell in the imploding capsule. However, in a planar geometry, one can access similar conditions with a CH foil and probe it using optical interferometry.[1] This technique was used for the first time in recent experiments[2] to diagnose the low-density part of the rarefaction wave formed when the shock driven by two OMEGA EP laser beams breaks out of a CH foil. The optical interferometry produces images in the focal plane that are proportional to the optical path (phase) that is accumulated by the wavefront of the probe laser propagating through the region of interest. The images are analyzed to obtain spatial profiles of the index of refraction. In low-density and low-temperature conditions, such as in the shock-release material, the plasma is partially ionized and the index of refraction is expected to have contributions from bound and free electrons and to depend on densities of atoms and free electrons which are connected to each other by the ionization state Z. Therefore, the index of refraction and Z are required to deduce the free-electron (plasma) density profiles from the interferograms.

The index of refraction at low densities and temperatures of shock-release material at a specific frequency of the laser probe is not generally expected to be available. While there are many studies of the optical properties of CH at solid or few times solid density,[3] no experimental data are available for rarefied CH gas at 10^{-5} to 10^{-2} g/cm^3 and few-eV temperatures. Recently *ab initio* simulations have become popular, are now accessible for calculating optical properties of arbitrary materials, and can be used to obtain the index of refraction at a desired laser frequency and thermodynamic conditions, i.e., mass density ρ and temperature T. The ionization state Z for CH material as a function of ρ and T is traditionally available via numerous Z tables used in ICF radiation-hydrodynamic codes. The simulations and analysis of the shock-release experiments[2] used the astrophysical opacity tables (AOT's) and collisional radiative equilibrium (CRE) tables, which predict different Z's for the release conditions, and plasma index of refraction, which has no atomic contribution. These shortcomings motivated the present investigation.

In this summary we calculate the ionization state Z and the dielectric constant (which we use to obtain the index of refraction) as a function of density and temperature under conditions relevant to shock release. The conditions span several orders of magnitude in density $\rho = 10^{-5}$ to 10^{-2} g/cm^3 at a few-eV temperatures. We develop an algorithmically transparent, easy-to-follow method for calculating Z [which we call the Saha–Fermi–Debye–Hückel (SFDH) method] based on the free-energy minimization approach,[4] with free energy containing nonideal terms accounting for binary collisions and Coulomb interactions. We also obtain Z using *ab initio* calculations based on the Mermin–Kohn–Sham density functional theory (DFT) and test it against the semi-analytical method. After verifying the DFT-calculated ionization state against the semi-analytical method, we use the electron population

states obtained with the DFT and Kubo–Greenwood formulation to calculate the dielectric constant. Using the combined approach outlined above, we found that (a) Z calculated with the developed method and DFT agrees well with each other and is in reasonable agreement with that from CRE and AOT tables; (b) DFT-calculated atomic polarizabilities were within 20% of the reference data; and (c) a fit to the DFT-calculated dielectric constant contains an extra term due to atomic polarizabilities (i.e., contributions from bound states of electrons in atoms) that dominate the dielectric constant at low temperatures and Z. Based on these calculations, we revisited the shock-release experiments[2] and found more-accurate electron density profiles that, however, have not changed the main conclusions of Ref. 2.

Figure 1 shows the average ionization state Z as a function of temperature T for three mass densities ρ. The ionization state in Fig. 1 was obtained using four different sources: AOT tables, CRE tables, results of our SFDH method, and *ab initio* calculations. The *ab initio* calculations of Z used Kohn–Sham DFT and were performed using the Vienna *ab initio* simulation package (VASP) with the Perdew–Burke–Ernzerhof exchange-correlation (XC) functional. The DFT method calculates the electron states and their populations for each thermodynamic condition. Optical properties at each thermodynamic condition, which are used in the following sections, were calculated using the Kubo–Greenwood formulation[5] implemented in the KGEC@*Quantum Espresso*[6] package with the strongly constrained and appropriately normed XC functional.
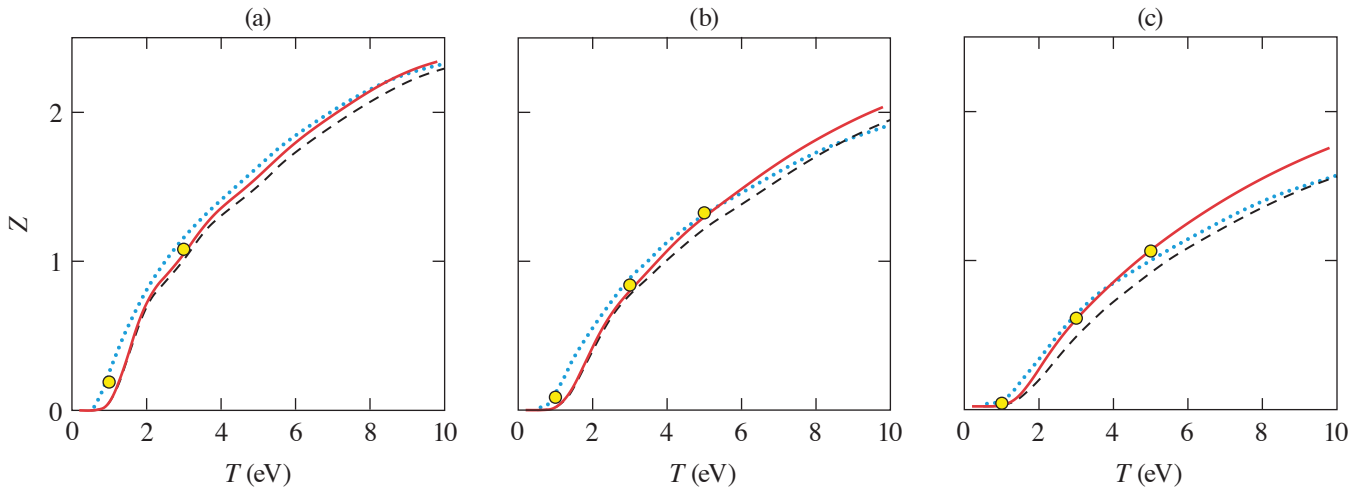
TC15641JR

Figure 1

Average ionization state Z as a function of temperature from four different models: AOT (dashed black curves), CRE (dotted blue curves), our SFDH method (solid red curves), and the DFT calculations (yellow circles) for three mass densities: (a) 10^{-4} g/cm^3, (b) 10^{-3} g/cm^3, and (c) 10^{-2} g/cm^3.

As one can see from Fig. 1, the *ab initio* calculations (yellow circles) are in very good agreement with the calculations using the SFDH method (solid red curves) at 3- and 5-eV temperatures, while Z from AOT (dashed black curves) and CRE (dotted blue curves) are up to 20% off. At lower temperatures (1 eV), the DFT method predicts noticeably higher Z than SFDH. The discrepancy is caused by the self-interaction error inherent in the DFT local and semi-local approximations for the XC energy.[7] The electron self-interaction decreases the ionization energy of H and to a lesser degree C atoms and leads to an artificial increase in Z, which is more apparent for temperatures much smaller than the ionization energies.

Figure 2 shows the dependence of the dielectric constant of CH on the temperature for two densities at the OMEGA EP laser probe wavelength of $\lambda = 263$ nm. Analysis of the index of refraction of CH at 1-, 3-, and 5-eV temperatures and 0.01- and 0.001-g/cm^3 densities leads to the following approximate formula for the real part of the dielectric constant (dashed red curves in Fig. 2):

$$\varepsilon_{\text{DFT}} = 1 + 4\pi \left(1.7\,\text{Å}^3 \cdot n_{\text{i}} - 4.9\,\text{Å}^3 \cdot n_{\text{e}} \right), \tag{1}$$

TC15645JR
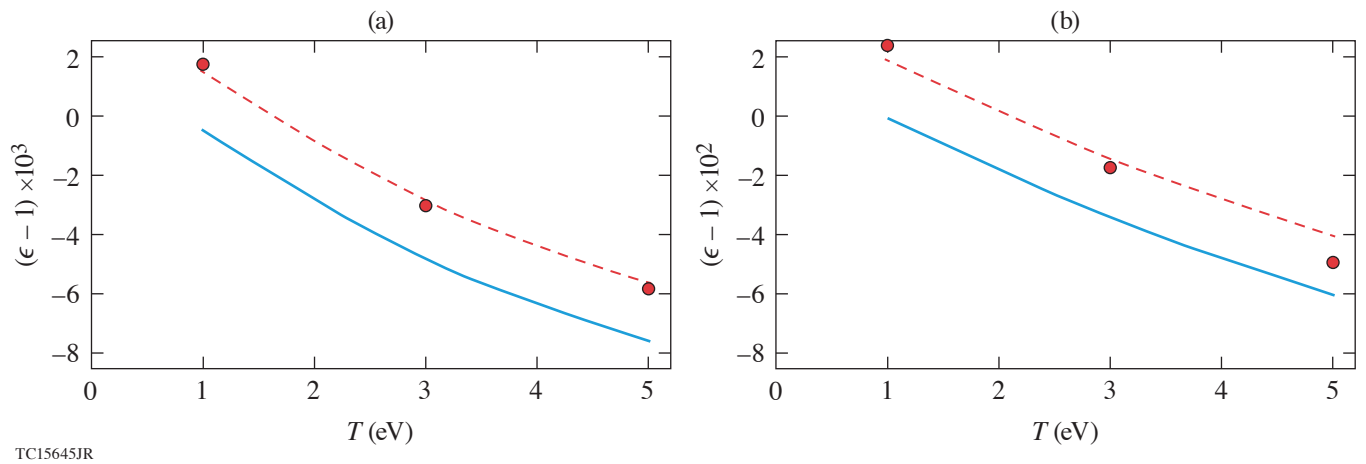
Figure 2

The real part of the dielectric permittivity in CH as a function of temperature from DFT calculations (red circles), from Eq. (1) (dashed red curves), and from Eq. (2) (solid blue curves) for mass densities of (a) 10^{-3} g/cm^3 and (b) 10^{-2} g/cm^3.

where $n_e = Z n_i$ is the electron density in Å^{-3} and n_i is the ion density in Å^{-3}, $n_i = \rho \langle A \rangle$, where $\langle A \rangle = 6.5$ amu is the average ion mass for 50% C – 50% H. The dielectric constant from Eq. (1) should be compared to the dielectric constant (solid blue curves in Fig. 2)

$$\varepsilon_p = 1 - 4\pi \cdot 4.9\,\text{Å}^3 \cdot n_e \qquad (2)$$

that was previously used in the analysis of the shock-release experiments.[2] The formula in Eq. (2) is the high-frequency plasma dielectric constant $\varepsilon_p = 1 - n_e / n_c$ (referred to below as the plasma dielectric constant),[8] where n_c is the critical density and $n_c = 1/(4\pi \times 4.9)$ Å^{-3} for $\lambda = 263$ nm. The fit of Eq. (1) to the DFT-calculated dielectric constant contains a term $\sim n_i$, which is the contribution from atomic polarizabilities (i.e., the contribution from bound states of electrons in atoms) and is not present in the plasma dielectric constant [Eq. (2)].

The index of refraction calculated with the DFT method, $n_{DFT} = \sqrt{\varepsilon_{DFT}}$, was used to revisit the interferometry data from the shock-release experiments.[2] Electron densities were found to be up to 40% higher and the position of the rarefaction wave up to 20 μm further than reported in Ref. 2. It is important to note that for a laser drive of lower intensity than in Ref. 2, the plasma index of refraction is not valid and the DFT index of refraction must be used in the analysis of the shock-release experiments.

1. A. Howard *et al.*, Rev. Sci. Instrum. **89**, 10B107 (2018).
2. D. Haberberger *et al.*, Phys. Rev. Lett. **123**, 235001 (2019).
3. W. Theobald *et al.*, Phys. Plasmas **13**, 122702 (2006).
4. D. G. Hummer and D. Mihalas, Astrophys. J. **331**, 794 (1988).
5. R. Kubo, J. Phys. Soc. Jpn. **12**, 570 (1957); D. A. Greenwood, Proc. Phys. Soc. Lond. **71**, 585 (1958).
6. L. Calderín, V. V. Karasiev, and S. B. Trickey, Comput. Phys. Commun. **221**, 118 (2017); V. V. Karasiev, T. Sjostrom, and S. B. Trickey, Comput. Phys. Commun. **185**, 3240 (2014).
7. J. P. Perdew and A Zunger, Phys. Rev. B **23**, 5048 (1981).
8. J. D. Jackson, *Classical Electrodynamics*, 3rd ed. (Wiley, New York, 1999).

Cross-Beam Energy Transfer Saturation by Ion Heating

A. M. Hansen,[1,2] K. L. Nguyen,[1,2] D. Turnbull,[1] B. J. Albright,[3] R. K. Follett,[1] R. Huff,[1] J. Katz,[1] D. Mastrosimone,[1] A. L. Milder,[1] L. Yin,[3] J. P. Palastro,[1] and D. H. Froula[1,2]

[1]Laboratory for Laser Energetics, University of Rochester
[2]Department of Mechanical Engineering, University of Rochester
[3]Los Alamos National Laboratory

Cross-beam energy transfer (CBET) saturation by ion heating was measured in a gas-jet plasma characterized using Thomson scattering. A wavelength-tunable UV probe laser beam interacted with four intense UV pump beams to drive large-amplitude ion-acoustic waves. For the highest-intensity interactions, the power transferred to the probe laser dropped, demonstrating ion-acoustic–wave saturation. Over this time, the ion temperature was measured to increase by a factor of 7 during the 500-ps inter-action. Particle-in-cell simulations show ion trapping and subsequent ion heating consistent with measurements. Linear kinetic CBET models were found to agree well with the observed energy transfer when the measured plasma conditions were used.

In laser-driven inertial confinement fusion (ICF), high-intensity lasers are used to drive capsules that reach pressure and temperature conditions required for nuclear fusion.[1] This requires multiple overlapping laser beams to propagate through plasmas surrounding the fusion capsule. The plasma mediates energy transfer between the laser beams, which can disrupt the energy coupling and/or cause irradiation nonuniformity.[2,3] To account for this CBET, linear models have been implemented in the hydrodynamic codes used to simulate ICF experiments.[4,5] The ability to predict this transfer of energy is critical to the success of all laser-driven ICF concepts.

The experiment was performed on the OMEGA laser–plasma interaction platform. Figure 1 illustrates the experimental configuration that consisted of a gas-jet system that produced a gas plume, which was heated by nine 500-ps-long UV beams. The target gas was a mixture of 45% nitrogen and 55% hydrogen to approximately reproduce the ion-acoustic wave damping from typical ICF experiments. The probe beam used the tunable OMEGA port 9 (TOP9) laser, which was wavelength tunable over ~3 nm around the pump beams' wavelength of 351.11 nm. The resonant wavelength of the probe beam (351.40 nm) was used for all experiments and was determined by maximizing the energy transfer while scanning its wavelength. The four CBET pump beams used half-wave plates to align their linear polarizations to the probe beam's polarization and had single-beam averaged intensities of $\sim 7 \times 10^{14}$ W/cm^2. The power in the probe beam was measured before and after the CBET interaction using the transmitted beam diagnostic (TBD). The time-resolved plasma conditions were measured using the streaked Thomson-scattering system.

Shots were performed for a range of incident probe-beam intensities, and time-resolved measurements of the plasma conditions and outgoing probe intensity were made. Figure 2 shows the amplification of the probe beam due to CBET at four initial probe intensities. Although the ion-acoustic wave (IAW) amplitudes are expected to increase with increasing probe intensity, linear CBET theory predicts a constant P/P_0 (pump depletion was negligible in the experiment by design). The fact that the power ratio P/P_0 decreases with increasing probe intensity with minimal pump depletion suggests nonlinear saturation. Furthermore, every probe-beam intensity greater than 0.1×10^{14} W/cm^2 exhibits a strong time-dependent reduction in amplification. For the three highest initial probe-beam intensities, the amplification started high (~1000 ps) but decreased over time before plateauing toward the end of the pump pulse (~1300 ps).
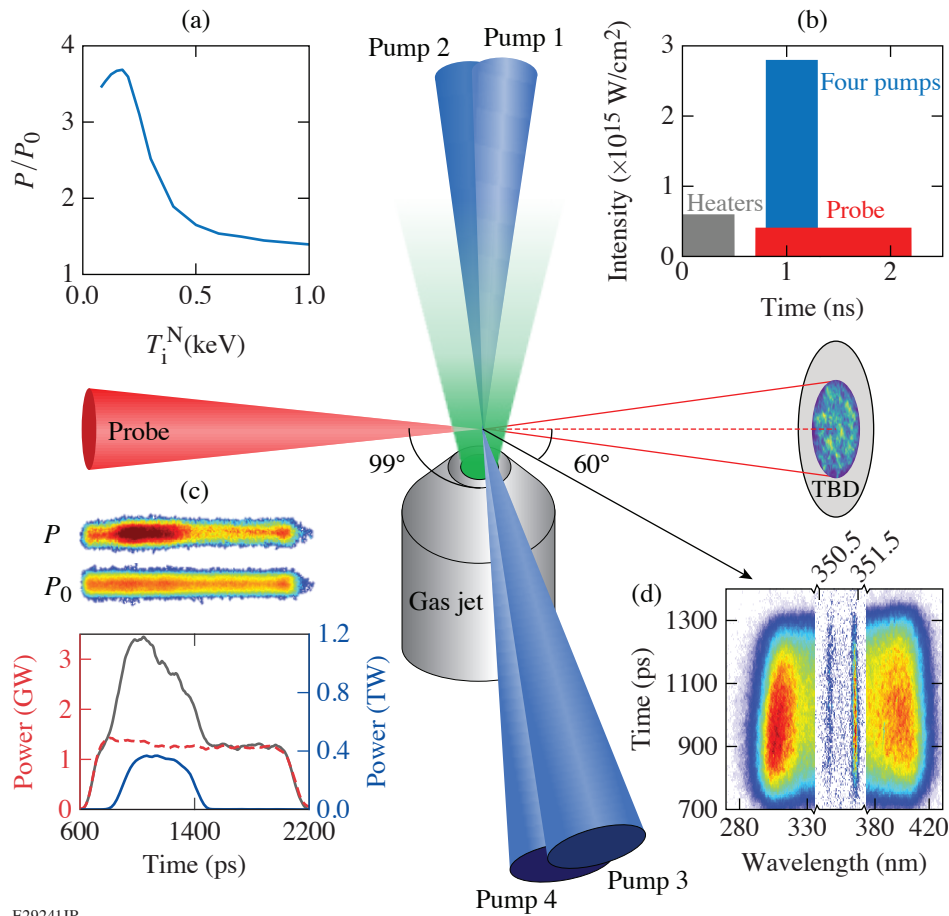
Figure 1

(a) The ratio of the output power (P) to the incident power (P_0) of the probe beam was calculated using a linear kinetic CBET model for the conditions of these experiments over a range of nitrogen ion temperatures. (b) The laser intensity, pulse shapes, and beam timings for each of the beam groups. (c) TBD data showing the input- (dashed red curve) and output- (solid black curve) probe and pump (solid blue curve) powers. (d) Time-resolved Thomson-scattering data showing the electron plasma wave and ion-acoustic wave spectra of a pump beam with minimal ion heating.

The plasma conditions measured using Thomson scattering revealed ion heating due to CBET in the high-intensity probe-beam shots ($I_0 > 0.1 \times 10^{14}$ W/cm^2). Kinetic linear theory predictions of CBET were in excellent agreement with the measured energy transfer when these increased ion temperatures were considered. As the ions were heated, the IAW dispersion evolved along a new branch with increased frequency at the wave number determined by the beam crossing angle. Because the driving frequency was fixed, the driven IAW was no longer at a resonant frequency, which increased the wave damping and saturated CBET.

Simulations of the high-intensity CBET interaction using the code VPIC were performed and found to qualitatively reproduce the measured energy transfer and ion heating. These simulations showed that at high probe-beam intensities, the large driven IAW's trapped and accelerated ions to the wave's phase velocity. The trapped ions were then detrapped through ion–ion collisions on short time scales (~10 ps), which resulted in bulk ion heating on ~100-ps time scales.

Although significant nonlinear CBET physics is occurring at the high probe-beam intensities, it is interesting that the linear CBET theory reproduces the measured results when accounting for the instantaneous plasma conditions. The plasma conditions are affected by CBET, however, suggesting that feedback from laser–plasma instabilities on hydrodynamics must be accounted for in modeling to accurately predict the energy transfer.[5]

E29243JR
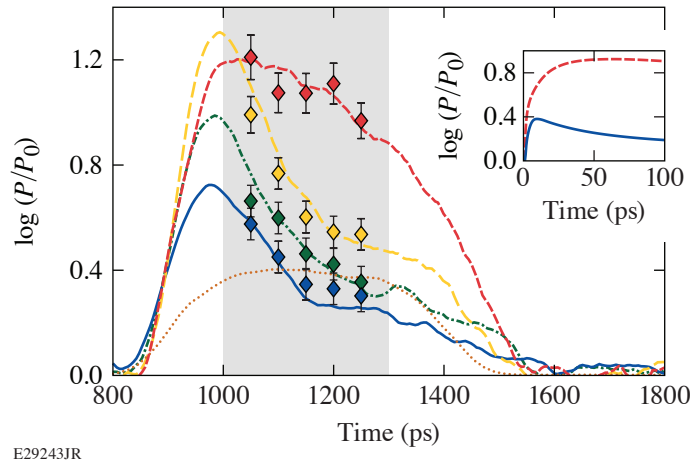
Figure 2

The power transferred into the probe beam for four different initial probe-beam intensities [0.1×10^{14} W/cm^2 (dashed red curve), 0.9×10^{14} W/cm^2 (dashed yellow curve), 2.0×10^{14} W/cm^2 (dashed–dotted green curve), 4.1×10^{14} W/cm^2 (solid blue curve)], and the corresponding calculated power transfer using linear kinetic theory for the measured plasma conditions (diamonds). The pulse shape of the pump beams is overlayed for reference (dotted orange curve). The inset shows VPIC simulated probe beam amplification corresponding to the lowest (dashed red curve) and highest (solid blue curve) experiment probe intensities.

1. R. Betti and O. A. Hurricane, Nat. Phys. **12**, 435 (2016).
2. V. N. Goncharov *et al.*, Phys. Plasmas **15**, 056310 (2008).
3. D. J. Strozzi *et al.*, Phys. Rev. Lett. **118**, 025002 (2017).
4. P. Michel *et al.*, Phys. Rev. Lett. **102**, 025004 (2009).
5. P. Michel *et al.*, Phys. Rev. Lett. **109**, 195004 (2012).

Thresholds of Absolute Two-Plasmon–Decay and Stimulated Raman Scattering Instabilities Driven by Multiple Broadband Lasers

R. K. Follett,[1] J. G. Shaw,[1] J. F. Myatt,[2] H. Wen,[1] D. H. Froula,[1] and J. P. Palastro[1]

[1]Laboratory for Laser Energetics, University of Rochester
[2]Department of Electrical and Computer Engineering, University of Alberta

In direct-drive inertial confinement fusion (ICF), a millimeter-scale spherical capsule is illuminated by symmetrically oriented laser beams.[1] The lasers ablate the outer layer of the capsule, which generates pressure to implode the fuel. In addition to depositing thermal energy in the ablator, the lasers can resonantly drive various laser–plasma instabilities that can degrade the quality of the implosion. Large-amplitude electron plasma waves (EPW's) are particularly problematic because they accelerate electrons to suprathermal energies, which can prematurely heat the fuel and impede compression of the capsule. The primary instabilities that generate EPW's in ICF experiments are stimulated Raman scattering (SRS) and two-plasmon decay (TPD).[2]

It has been known since the 1970s that broadband lasers can be used to suppress parametric instabilities,[3,4] but all of the large-scale lasers used in ICF experiments use neodymium glass amplifiers and have very little native bandwidth (<0.1%). There have been a number of studies on parametric instability suppression using excimer gas lasers that have sufficient native bandwidth (~0.1%) to suppress slowly growing instabilities, like filamentation, but not enough to suppress TPD and SRS.[5] Experiments have demonstrated the use of stimulated rotational Raman scattering to significantly increase the bandwidth of both solid-state and gas lasers.[6,7] Another potential path toward high-energy broadband lasers is through the use of optical parametric amplifiers, where a high-energy narrowband laser is used to pump a broadband seed beam. This technique has demonstrated ~70% conversion efficiency to a seed beam with ~5% relative bandwidth at 1053 nm (Ref. 8).

These laser-technology developments have led to a resurgence of interest in using broadband lasers to suppress parametric instabilities in ICF experiments.[9,10] The majority of existing numerical studies considered only one or a few beams in 1-D or 2-D. In actual ICF experiments, many overlapping laser beams are focused onto the target surface. Although the single-beam intensities are typically low, overlapping beams can drive the same plasma waves, resulting in instability even when the intensities of the individual beams are below the single-beam thresholds.[11,12] To assess the viability of using bandwidth to suppress parametric instabilities in ICF experiments, the existing results need to be extended to realistic multibeam geometries.

This summary presents a numerical study of the bandwidth required to suppress absolute TPD and SRS under conditions relevant to direct-drive ICF. Multibeam absolute instability thresholds are obtained for SRS (backscatter and sidescatter) and TPD using 3-D simulations with realistic ICF drive-beam configurations including phase plates and polarization smoothing. Bandwidth is found to be more effective at mitigating multibeam absolute TPD and SRS backscatter than the corresponding single-beam instabilities. The effectiveness of bandwidth at mitigating multibeam absolute SRS sidescatter is found to be similar to the single-beam instability. Despite having the largest fractional increase in threshold relative to the monochromatic case, absolute SRS backscatter has the lowest absolute instability threshold for ignition-relevant plasma conditions over the range of bandwidths considered. Studies of the sensitivity to beam geometry and spectral dispersion suggest that the main results presented here are applicable to a broad range of potential ICF driver geometries.

Figure 1 shows the absolute TPD and SRS thresholds near $n_c/4$ as a function of laser bandwidth for $L_n = 200~\mu$m, $T_e = 2$ keV [Fig. 1(a)] and $L_n = 400~\mu$m, $T_e = 4$ keV [Fig. 1(b)]. The thresholds are normalized to the zero-bandwidth thresholds to highlight

E29414JR
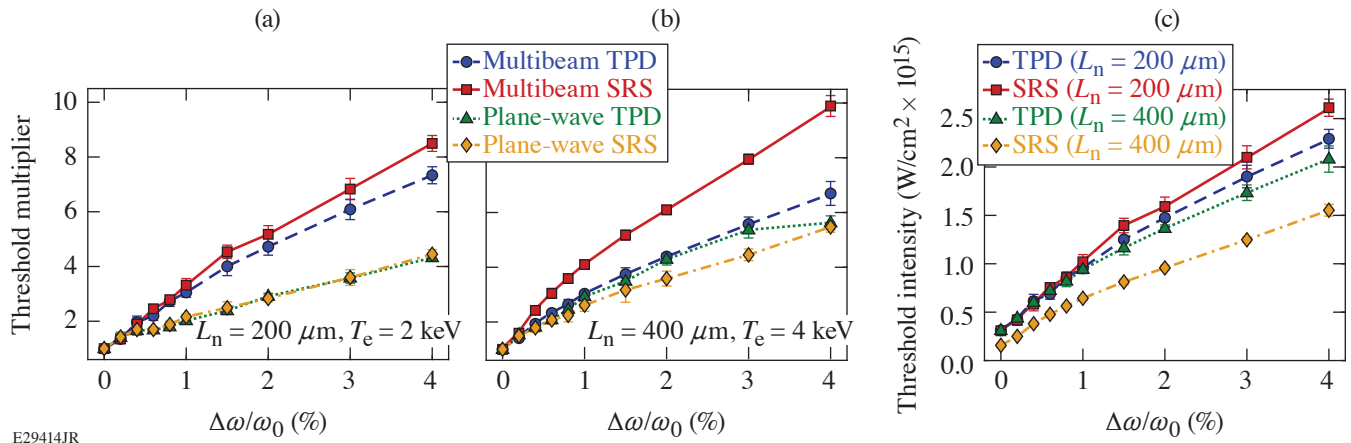
Figure 1
Absolute instability thresholds as a function of the laser normalized to the monochromatic threshold for (a) $L_n = 200\ \mu$m, $T_e = 2$ keV and (b) $L_n = 400\ \mu$m, $T_e = 4$ keV. The various curves correspond to multibeam TPD (blue circles), multibeam SRS (red squares), single-beam TPD (green triangles), and single-beam SRS (yellow diamonds). (c) The multibeam thresholds from (a),(b) in W/cm^2 for TPD (blue circles) and SRS (red squares) at $L_n = 200\ \mu$m and TPD (green triangles) and SRS (yellow diamonds) at $L_n = 400\ \mu$m.

the relative effectiveness of bandwidth mitigation. The error bars correspond to the standard deviation from an ensemble of four threshold calculations with random realizations of polarization, speckle pattern, and spectral phase.

The thresholds for a single plane-wave drive beam are plotted in Figs. 1(a) and 1(b) to show the relative effectiveness of using bandwidth to mitigate single-beam and multibeam instabilities. Intuitively we might expect that the impact of bandwidth on the instability thresholds is independent of the multibeam coupling. If that were the case, the plane-wave and multibeam curves for a given instability would be the same, and only the monochromatic multibeam thresholds and the broadband single-beam thresholds would be needed to calculate the broadband multibeam thresholds. However, the single-beam threshold multipliers are always less than the corresponding multibeam threshold multipliers. This suggests that in addition to increasing the single-beam instability thresholds, broadband lasers reduce the effectiveness of multibeam coupling.

Figure 1(c) shows the multibeam threshold curves from Figs. 1(a) and 1(b) in terms of the absolute overlapped laser intensity (W/cm^2). For the $L_n = 200$-μm case, the TPD and SRS thresholds are similar at all laser bandwidths. Despite having the largest fractional increase in threshold for a given bandwidth, multibeam SRS with $L_n = 400\ \mu$m always has the lowest absolute threshold because of its low monochromatic threshold.

1. J. Nuckolls *et al.*, Nature **239**, 139 (1972).
2. W. L. Kruer, *The Physics of Laser Plasma Interactions*, Frontiers in Physics, Vol. 73, edited by D. Pines (Addison-Wesley, Redwood City, CA, 1988).
3. J. J. Thomson and J. I. Karush, Phys. Fluids **17**, 1608 (1974).
4. G. Laval *et al.*, Phys. Fluids **20**, 2049 (1977).
5. T. A. Peyser *et al.*, Phys. Fluids B **3**, 1479 (1991).
6. D. Eimerl, D. Milam, and J. Yu, Phys. Rev. Lett. **70**, 2738 (1993).
7. J. Weaver *et al.*, Appl. Opt. **56**, 8618 (2017).
8. C. Dorrer, E. M. Hill, and J. D. Zuegel, Opt. Express **28**, 451 (2020).

9. J. W. Bates *et al.*, Phys. Rev. E **97**, 061202(R) (2018).

10. R. K. Follett *et al.*, Phys. Plasmas **26**, 062111 (2019).

11. D. F. DuBois, B. Bezzerides, and H. A. Rose, Phys. Fluids B **4**, 241 (1992).

12. C. Stoeckl *et al.*, Phys. Rev. Lett. **90**, 235002 (2003).

Temporal Reflection and Refraction of Optical Pulses Inside a Dispersive Medium: An Analytic Approach

J. Zhang,[1] W. R. Donaldson,[2,3] and G. P. Agrawal[1,2]

[1]The Institute of Optics, University of Rochester
[2]Laboratory for Laser Energetics, University of Rochester
[3]Department of Electrical and Computer Engineering, University of Rochester

Reflection of electromagnetic waves at a temporal boundary has attracted considerable attention in several contexts over the last 20 years.[1] Most of these studies have focused on a nondispersive medium and ignored the frequency dependence of the refractive index on each side of the temporal boundary. The dispersive effects were included in a 2015 study[2] that considered the reflection and refraction of optical pulses at a moving boundary.

We develop an analytic approach for reflection of light at a temporal boundary inside a dispersive medium and derive frequency-dependent expressions for the reflection and transmission coefficients. Using the analytic results, we study the temporal reflection of an optical pulse and show that our results agree fully with a numerical approach used earlier. Our approach provides approximate analytic expressions for the electric fields of the reflected and transmitted pulses; where the width of transmitted pulse is modified, the reflected pulse is a mirrored version of the incident pulse. When a part of the incident spectrum lies in the region of total internal reflection, both the reflected and transmitted pulses are considerably distorted.

We consider propagation of optical pulses inside a dispersive medium (such as an optical fiber) with the propagation constant $\beta(\omega)$. We assume that the pulse's spectrum is relatively narrow (quasi-monochromatic approximation), and we can expand $\beta(\omega)$ around a reference frequency in a Taylor series as

$$\beta(\omega) = \beta_0 + \beta_1(\omega - \omega_0) + \frac{1}{2}\beta_2(\omega - \omega_0)^2, \tag{1}$$

where ω_0 is a reference frequency close to the central frequency of the pulse and we neglected the third- and higher-order dispersive terms. We assume that the pulse is approaching a temporal boundary moving at the speed v_B. The refractive index changes across this boundary by a constant amount Δn and the propagation constant after the boundary becomes

$$\beta_t(\omega) = \beta_0 + \beta_B + \beta_1(\omega - \omega_0) + \frac{1}{2}\beta_2(\omega - \omega_0)^2, \tag{2}$$

where $\beta_B = (\omega_0/c)\Delta n$.

The evolution of the pulse across the temporal boundary is governed by the following Eq. (2) satisfied by the slowly varying envelope $A(z,t)$ of the pulse:

$$\frac{\partial A}{\partial z} + \Delta\beta_1 \frac{\partial A}{\partial t} + i\frac{\beta_2}{2}\frac{\partial^2 A}{\partial t^2} = i\beta_B H(t - T_B)A, \tag{3}$$

where we work in a frame in which the temporal boundary appears stationary, i.e., $t = t' - z/v_B$, where t' is the time in the laboratory frame; $\Delta\beta_1 = \beta_1 - 1/v_B$ is the relative group delay of the pulse in this time frame. In Eq. (3), $H(t–T_B)$, is the heaviside step

function taking the value 1, when $t > T_B$, and 0, when $t < T_B$. Given the initial pulse shape $A(0,t)$, numerical solutions of Eq. (3) show that the pulse splits into two parts moving at different speeds because of the spectral shifts induced at the boundary.[2]

Our objective is to solve Eq. (3) analytically. The numerical solutions of Eq. (3) indicate that any input pulse is partially reflected and partially transmitted at the temporal boundary such that the two parts have spectra shifted from that of the input pulses. We expect the same to occur for a plane wave. In other words, a plane wave at the frequency $\omega_0 + \Delta\omega$ is also reflected and transmitted at the boundary with different frequency shifts such that the slowly varying amplitude takes the form:

$$A = \begin{cases} e^{i(\beta' z - \Delta\omega t)} + R e^{i(\beta'_r z - \Delta\omega_r t)}, & t < T_B \\ T e^{i(\beta'_t z - \Delta\omega_t t)}, & t > T_B \end{cases} , \tag{4}$$

where R and T are the reflection and transmission coefficients that depend on $\Delta\omega$. Here $\Delta\omega$ is the frequency shift of the input plane wave from the reference frequency ω_0, and $\Delta\omega_r$ and $\Delta\omega_t$ are frequency shifts of the reflected and transmitted plane waves, respectively. These frequency shifts depend on $\Delta\omega$.

We note that Eq. (4) does not violate causality because it is based on plane waves and the time variable $t = t' - z/v_B$ is defined in a moving frame with t' representing the real time. Causality requires only that the wave packets, representing the reflecting and transmitted parts of the incident pulse, form only after the pulse has arrived at the temporal boundary located at $z_B = T_B/\Delta\beta_1$. As discussed later, this is indeed the case.

We find the frequency shifts $\Delta\omega_r$ and $\Delta\omega_t$ by substituting the solution in Eq. (4) into Eq. (3) for $z < z_B$ and $z > z_B$. This yields the following relations:

$$\begin{cases} \beta'(\Delta\omega) = \Delta\beta_1 \Delta\omega + \dfrac{\beta_2}{2} \Delta\omega^2 \\[2ex] \beta'_r(\Delta\omega_r) = \Delta\beta_1 \Delta\omega_r + \dfrac{\beta_2}{2} \Delta\omega_r^2 \\[2ex] \beta'_t(\Delta\omega_t) = \beta_B + \Delta\beta_1 \Delta\omega_t + \dfrac{\beta_2}{2} \Delta\omega_t^2 \end{cases} . \tag{5}$$

These are the dispersion relation in the moving frame. From Eq. (3), $A(z,t)$ should be continuous for all values of z. This happens when the three propagation constants are equal, i.e.,

$$\beta' = \beta'_r = \beta'_t. \tag{6}$$

As discussed in Ref. 2, these conditions result from the conservation of momentum in the moving frame. Combining Eqs. (5) and (6), we find two quadratic equations whose solutions determine $\Delta\omega_r$ and $\Delta\omega_t$ for a given $\Delta\omega$. The solution for $\Delta\omega_r$ is

$$\Delta\omega_r = -\frac{2\Delta\beta_1}{\beta_2} - \Delta\omega. \tag{7}$$

The solution for $\Delta\omega_t$ is a more complicated and is given by[2]

$$\Delta\omega_t = -\frac{\Delta\beta_1}{\beta_2} + \frac{1}{\beta_2}\sqrt{(\Delta\beta_1 + \beta_2 \Delta\omega)^2 - 2\beta_2 \beta_B}. \tag{8}$$

To find the reflection and transmission coefficients, R and T, we make use of the temporal boundary conditions at $t = T_B$. Specifically, we demand that both A and $\partial A / \partial t$ are continuous across the time boundary for any z. This requirement results in the following two equations:

$$e^{i(\beta' z - \Delta\omega T_B)} + R e^{i(\beta'_r z - \Delta\omega_r T_B)} = T e^{i(\beta'_t z - \Delta\omega_t T_B)},$$

$$-i\Delta\omega e^{i(\beta' z - \Delta\omega T_B)} - i\Delta\omega_r R e^{i(\beta'_r z - \Delta\omega_r T_B)} = -i\Delta\omega_t T e^{i(\beta'_t z - \Delta\omega_t T_B)}. \tag{9}$$

Using $\beta' = \beta'_r = \beta'_t$ from Eq. (6), we obtain the following analytic expressions for R and T:

$$\begin{cases} R(\Delta\omega) = \dfrac{\Delta\omega_t - \Delta\omega}{\Delta\omega_r - \omega_t} e^{i(\Delta\omega_r - \Delta\omega)T_B} \\[2em] T(\Delta\omega) = \dfrac{\Delta\omega_r - \Delta\omega}{\Delta\omega_r - \omega_t} e^{i(\Delta\omega_t - \Delta\omega)T_B} \end{cases} \tag{10}$$

These expressions contain a linear phase shift that depends on the boundary's location T_B. This phase shift is not important and can be removed by choosing $T_B = 0$; however, R and T can still be complex quantities. Figure 1 shows how their moduli and phases vary as a function of the physically measured frequency shift $\Delta\nu = (\Delta\omega/2\pi)$ using the notation $R = |R| e^{i\phi(R)}$ and $T = |T| e^{i\phi(T)}$. The parameters used in Fig. 1 are appropriate for an optical fiber acting as a dispersive medium[2] and have values $\Delta\beta_1 = 0.1$ ps/m, $\beta_2 = 5$ ps^2/km, and $\beta_B = 0.5$ m^{-1}.
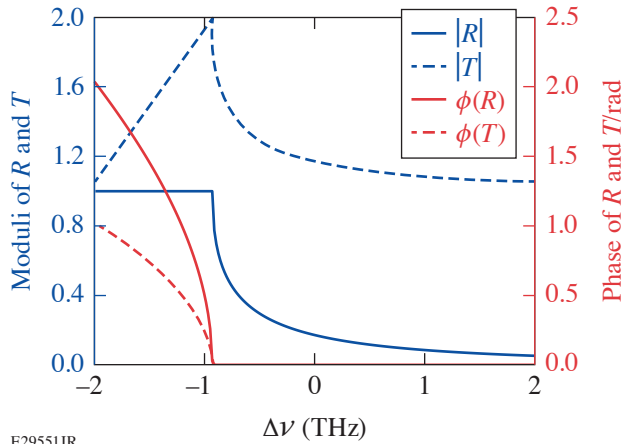
Figure 1
Frequency dependence of the reflection and transmission coefficients for $\Delta\beta_1 = 0.1$ ps/m, $\beta_2 = 5$ ps^2/km, and $\beta_B = 0.5$ m^{-1}. The solid blue curve represents the modulus of reflected wave and the solid red curve is the phase of the reflected wave. Likewise, the dashed blue curve is the modulus of the transmitted wave and the dahed red curve is the phase of the transmitted wave.

E29551JR

The most-striking feature in Fig. 1 occurs near $\Delta\nu_c = \sqrt{2\beta_2\beta_B} - \Delta\beta_1 / 2\pi\beta_2 = -0.93$ THz. When $\Delta\nu > \Delta\nu_c$, both R and T are real quantities; when $\Delta\nu < \Delta\nu_c$, they become complex. The reason for this change is related to the form of Eqs. (7) and (8). While $\Delta\omega_r$ is always real, $\Delta\omega_t$ can be complex depending on the sign of the discriminant in Eq. (8). The condition for this to occur is given by $(\Delta\beta_1 + \beta_2\Delta\omega)^2 < 2\beta_2\beta_B$. In this situation, $\Delta\omega_t$ becomes complex and the transmitted wave becomes evanescent. It can be shown that $|R| = 1$ holds for $\Delta\omega < \Delta\omega_c$. This is the temporal analog of total internal reflection discussed in Ref. 2. We call $\Delta\nu_c$ the critical frequency.

The preceding discussion applies to each specific frequency component of a pulse. We can use it to study how an incident pulse gets reflected and transmitted at the temporal boundary. Consider an incident pulse with the slowly varying amplitude

$$A(z = 0, t) = A_{in}(t). \tag{11}$$

We can decompose it into plane waves of different frequencies using the Fourier transform:

$$\tilde{A}(\Delta\omega) = \int A_{\mathrm{in}}(t)e^{i\Delta\omega t}\,\mathrm{d}t. \tag{12}$$

The evolution of each plane-wave component is governed by Eq. (4). The total field can be calculated by integrating over the input pulse's spectrum to obtain:

If $t < T_{\mathrm{B}}$,

$$A(z,t) = \frac{1}{2\pi}\int \tilde{A}(\Delta\omega)e^{i\left[\beta'(\Delta\omega)z - \Delta\omega t\right]}\mathrm{d}\Delta\omega$$

$$+\frac{1}{2\pi}\int \tilde{A}(\Delta\omega)R(\Delta\omega)e^{i\left[\beta'_{\mathrm{r}}(\Delta\omega)z - \Delta\omega_{\mathrm{r}}t\right]}\,\mathrm{d}\Delta\omega. \tag{13}$$

If $t > T_{\mathrm{B}}$,

$$A(z,t) = \frac{1}{2\pi}\int \tilde{A}(\Delta\omega)T(\Delta\omega)e^{i\left[\beta'_{\mathrm{t}}(\Delta\omega_{\mathrm{t}})z - \Delta\omega_{\mathrm{t}}t\right]}\mathrm{d}\Delta\omega. \tag{14}$$

This being our main result, it can be used to find the shapes and spectra of the reflected and transmitted parts of any input pulse.

1. J. T. Mendonça and P. K. Shukla, Phys. Scr. **65**, 160 (2002).
2. B. W. Plansinis, W. R. Donaldson, and G. P. Agrawal, Phys. Rev. Lett. **115**, 183901 (2015).

Equation of State, Sound Speed, and Reshock
of Shock-Compressed Fluid Carbon Dioxide

L. E. Crandall,[1,2] J. R. Rygg,[1,2,3] D. K. Spaulding,[4] M. F. Huff,[1,2] M. C. Marshall,[5] D. N. Polsin,[1] R. Jeanloz,[6] T. R. Boehly,[1] M. Zaghoo,[1] B. J. Henderson,[1,2] S. Brygoo,[7] P. M. Celliers,[5] J. H. Eggert,[5] D. E. Fratanduono,[5] A. Lazicki,[5] M. Millot,[5] and G. W. Collins[1,2,3]

[1]Laboratory for Laser Energetics, University of Rochester
[2]Department of Mechanical Engineering, University of Rochester
[3]Department of Physics and Astronomy, University of Rochester
[4]University of California, Davis
[5]Lawrence Livermore National Laboratory
[6]University of California, Berkeley
[7]Commissariat à l'energie atomique et aux energies alternatives, France

Mechanical equation-of-state data of initially liquid and solid CO_2 shock compressed to terapascal conditions are reported. Diamond–sapphire anvil cells were used to vary the initial density and state of CO_2 samples, which were then further compressed with laser-driven shock waves, resulting in a data set from which precise derivative quantities including Grüneisen parameter and sound speed are determined. Reshock states were measured to 800 GPa and map the same pressure–density conditions as the single shock using different thermodynamic paths. The compressibility data reported here do not support current density-functional-theory (DFT) calculations but are better represented by tabular equation-of-state models.

The covalent double bonds that bind the atoms in a CO_2 molecule at ambient conditions are among the strongest of chemical bonds, but at pressures reaching tens of GPa, the compression energy becomes comparable to this bonding energy (hundreds of kJ/mol) and the previously stable molecule exhibits complex chemical behavior.[1,2] Laser-heated diamond-anvil cell experiments have characterized the solid phase diagram of CO_2 up to 120 GPa, which exhibits five molecular crystalline polymorphic phases before transforming into both crystalline and amorphous polymeric phases.[1–7]

The fluid phase diagram of CO_2 has been experimentally explored to 1 TPa (Refs. 8–14) and is proposed to exhibit similar chemical complexity to the solid phase diagram.[15] When shock compressed, molecular liquid CO_2 (Fluid I) is stable up to 40 GPa, above which it transforms into an insulating 3- and 4-coordinated polymeric fluid (Fluid II).[12,15] Above 100 GPa, CO_2 transitions into the Fluid-III phase and begins to ionize.[14] The present work is a study of the Fluid-III phase of CO_2.

The pressure, density, temperature, and reflectivity of shocked CO_2 have been measured to 1 TPa and 93,000 K in Ref. 14. Experimental evidence indicates that CO_2 at the highest pressures and temperatures studied is in a complex bonded state as opposed to the previously predicted[13] fully atomic C, O fluid. This work reports further details of the study presented in Ref. 14, and it additionally reports the experimentally determined Grüneisen parameter and isentropic sound speed of shocked CO_2 and the mechanical behavior of CO_2 under reshock.

The pressure and density results from these experiments are plotted in Fig. 1(a) (triangles); the present measurements support LEOS[16] over current DFT[17] calculations in the high-pressure fluid regime. Variation in initial density was leveraged to measure multiple Hugoniot curves, from which derivative quantities were probed using a difference method.[18] The theoretical Grüneisen parameter is systematically higher than the experimental result, but all curves tend to the ideal gas limit of 2/3. The Eulerian

sound speed, plotted in Fig. 1(b), can be directly calculated from the measured Hugoniot and Grüneisen parameter.[19] LEOS 2274 (Ref. 16) shows excellent agreement with our experimental data. This is expected given the good agreement between LEOS 2274 (Ref. 16) and our Hugoniot data. The present work measured four reshock states in CO_2 and shows strong agreement with LEOS, as shown in Fig. 1(c).

To summarize, this work provides additional details on recently published[14] equation-of-state measurements of shock-compressed CO_2 to 1 TPa and 93,000 K from varying initial densities and presents new information on the Grüneisen parameter, sound speed, and reshock behavior of high-pressure shocked CO_2. We find that the compressibility, Grüneisen parameter, and sound speed of shocked CO_2 are well represented by LEOS;[16] this work does not support the extreme curvature in compressibility
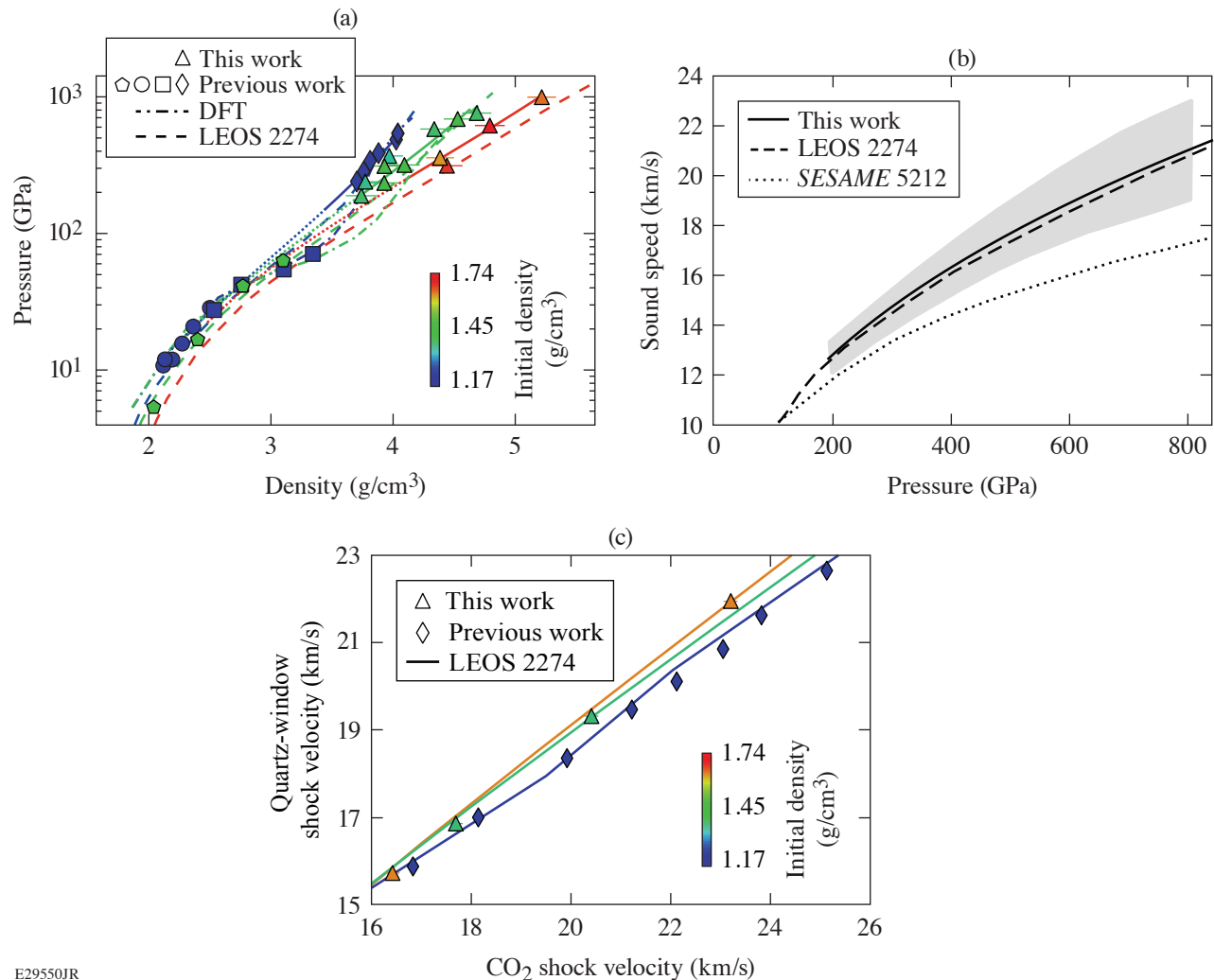
Figure 1

(a) Log pressure versus density for shocked CO_2: OMEGA data (triangles), Sandia Z data[13] (diamonds), and gas-gum data (pentagons,[8] circles,[10] and squares[12]). LEOS[16] (dashed curves) and density functional theory (DFT)[17] (dashed–dotted curves) are also calculated. Solid curves are fits to the OMEGA and Z data; dotted curves extrapolate this fit to lower pressure. The initial density of all data points and curves is given by the color bar. (b) Sound speed of shocked CO_2. This work (solid curve) calculates the sound speed from the measured Hugoniot and Grüneisen parameter. LEOS[16] (dashed curve) shows excellent agreement with these results, while *SESAME* (dotted curve) underpredicts the sound speed. (c) Shock velocity in the quartz window versus shock velocity in the CO_2 sample on either side of their respective interfaces. A reshock is launched back into the CO_2 sample when the shock traverses into the higher-impedance quartz window. These OMEGA data are represented by triangles and the Sandia Z data by diamonds. Solid lines are LEOS curves based on the modeled reshock intersecting with the experimental quartz Hugoniot.[20,21]

modeled by DFT.[17] Notably, lower-pressure gas-gun data support DFT over LEOS. This complexity in the compressibility behavior of shocked CO_2 warrants further study since there is currently a gap between 71 and 189 GPa where no data exist to constrain theory. We report four reshock states of CO_2 and discuss the effect of the Grüneisen parameter on the reshock curve. This work provides significant new benchmarks for theoretical calculations of fluids in the warm-dense-matter regime.

1. F. Datchi and G. Weck, Z. Kristallogr. **229**, 135 (2014).
2. C.-S. Yoo, Phys. Chem. Chem. Phys. **15**, 7949 (2013).
3. K. D. Litasov, A. F. Goncharov, and R. J. Hemley, Earth Planet. Sci. Lett. **309**, 318 (2011).
4. K. F. Dziubek *et al.*, Nat. Commun. **9**, 3148 (2018).
5. V. M. Giordano *et al.*, J. Chem. Phys. **133**, 144501 (2010).
6. V. M. Giordano, F. Datchi, and A. Dewaele, J. Chem. Phys. **125**, 054504 (2006).
7. H. Shimizu, T. Kitagawa, and S. Sasaki, Phys. Rev. B **47**, 11,567 (1993).
8. V. N. Zubarev and G. S. Telegin, Sov. Phys.-Dokl. **7**, 34 (1962).
9. Zubarev and Telegin[8] report two different initial densities for their solid CO_2: 1.45 and 1.54 g/cm^3. Cited in Schott[10] are "verbal inquires and replies conveyed through C. L. Mader and A. N. Dremin, ca. 1983" that confirm that 1.54 g/cm^3 is a misprint, and the initial density of the data published by Zubarev and Telegin is 1.45 g/cm^3.
10. G. L. Schott, High Press. Res. **6**, 187 (1991).
11. Each measurement of the shock velocity in Ref. 8 is the average of 4 to 12 independent measurements with a 1% to 2% deviation from the mean. Reference 10 similarly presents duplicate measurements of transit times but does not indicate uncertainty. No rigorous systematic uncertainty analysis associated with the data in Refs. 8 and 10 was reported.
12. W. J. Nellis *et al.*, J. Chem. Phys. **95**, 5268 (1991).
13. S. Root *et al.*, Phys. Rev. B **87**, 224102 (2013).
14. L. Crandall *et al.*, Phys. Rev. Lett. **125**, 165701 (2020).
15. B. Boates, A. M. Teweldeberhan, and S. A. Bonev, Proc. Natl. Acad. Sci. **109**, 14808 (2012).
16. C. J. Wu *et al.*, J. Chem. Phys. **151**, 224505 (2019).
17. B. Boates *et al.*, J. Chem. Phys. **134**, 064504 (2011).
18. D. G. Hicks *et al.*, Phys. Rev. Lett. **97**, 025502 (2006).
19. R. G. McQueen, S. P. Marsh, and J. N. Fritz, J. Geophys. Res. **72**, 4999 (1967).
20. M. P. Desjarlais, M. D. Knudson, and K. R. Cochrane, J. Appl. Phys. **122**, 035903 (2017).
21. S. Brygoo *et al.*, J. Appl. Phys. **118**, 195901 (2015).

Carbon-Doped Sulfur Hydrides as a Room-Temperature Superconductor at 270 GPa

S. X. Hu,[1,2] R. Paul,[1,2] V. V. Karasiev,[1] and R. P. Dias[2,3]

[1]Laboratory for Laser Energetics, University of Rochester
[2]Department of Mechanical Engineering, University of Rochester
[3]Department of Physics and Astronomy, University of Rochester

Superconductivity is the property of the complete absence of electrical resistance at temperatures below a critical transition temperature (T_c). For conventional superconductors, the electron–phonon coupling mediates the formation of a Cooper pair of electrons with opposite spins, as described in the Bardeen–Cooper–Schrieffer (BCS) theory. However, the highest transition temperature attained by any conventional superconductors so far is $T_c = 39$ K in MgB_2. In the past five years, exciting high-T_c superconducting materials have been discovered. In particular, the first experimental synthesis of H_3S gave an unprecedentedly high $T_c = 203$ K at a pressure of $P \approx 150$ GPa (Ref. 1). Most recently, a room-temperature superconductor has been experimentally realized in a carbonaceous sulfur hydride (CSH) system,[2] which demonstrated $T_c = 287.7\pm1.2$ K at 267 ± 10 GPa. This experimental finding has excited the condensed-matter and high-pressure physics communities to understand this "puzzling" ternary CSH system since recent studies[3,4] prior to the experiment[2] did not predict room-temperature T_c behavior.

We used the evolutionary structure searching code USPEX combined with the density-functional-theory code VASP to determine the possible stoichiometry and stable crystal structures, in a wide pressure range from 20 to 300 GPa, for various combinations of $C_iS_jH_k$ using the electronic formation enthalpy ΔH (eV/atom) < 0 as the criterion. These results showed a general trend: CSH compounds composed of one CH_4 "guest" molecule and integer numbers of H_3S "host" molecules tend to have lower formation enthalpy. This energetics observation prompted us to look into the binary components of C_iH_k, S_jH_k, and C_iS_j. These binary searches resulted in the following conclusion: the basic unit of H_3S in its *Im-3m* cubic structure gives the lowest formation enthalpy of $\Delta H_{H_3S} \approx -0.125$ eV/atom among all such binary compounds. From a thermodynamic stability point of view, these results unambiguously suggest that a higher H_3S concentration in a ternary CSH compound should drive the system to lower formation enthalpy (more stable). This led us to explore the energetics and stability of carbon doping in H_3S systems.

To examine the formation enthalpy of carbon-doped H_3S systems, we varied the ratio of carbon to sulfur in a "supercell" composed of an integral number of H_3S units in its *R3m* or *Im-3m* structure, i.e., taking systems like $C_1S_{15}H_{48}$ and $C_1S_{17}H_{54}$ as examples. We then calculated the total formation enthalpy (including the zero point energy of ions: ΔE_{ZPE}) for these energetically optimized CSH compounds in the pressure range of 80 to 300 GPa. The H_3S system has the lowest formation enthalpy for all the structures examined in this pressure range. Carbon-doped sulfur hydrides, varying from $C_1S_{35}H_{108}$ to $C_1S_{19}H_{30}$, are energetically second to the pure H_3S system within an ~50-meV difference of ΔH_{total}. Nevertheless, these carbon-doped sulfur hydrides are both thermodynamically and dynamically stable since they all have $\Delta H_{total} < 0$ and no imaginary components in their phonon spectra. At low pressures (<80 GPa), the CSH system takes the most-stable stoichiometry of $C_2S_2H_{10}$, composed of one C_2H_6 (ethane) molecule linked by hydrogen bonding with two H_2S molecules in P_1 symmetry.

To examine if these identified carbon-doped sulfur hydrides exhibit any high-temperature superconductivity, we employed the Allen–Dynes–McMillian equation implemented in the density functional theory code *Quantum Espresso* to estimate the T_c for compounds varying from $C_1S_9H_{30}$ to $C_1S_{35}H_{108}$ in the pressure range of 150 to 300 GPa, with the virtual crystal approximation. The T_c results from these calculations for $C_1S_{15}H_{48}$ and $C_1S_{17}H_{54}$, as shown in Fig. 1(b) as a function of pressure, showed good

agreement with experiment and a room-temperature $T_c = 280 \pm 10$ K at ~270 GPa. Figure 1(c) plots the estimated maximum T_c variation as a function of carbon-doping level, corresponding to the stable CSH compounds ranging from $C_1S_9H_{30}$ to $C_1S_{35}H_{108}$ at 270 GPa. A peak of $T_c \sim 290$ K appears at an *optimal* carbon-doping level of ~5.56% (corresponding to $C_1S_{17}H_{54}$). In the CSH experiment[2] there was no intentional control of the carbon-doping level. Therefore, the experimentally synthesized CSH samples
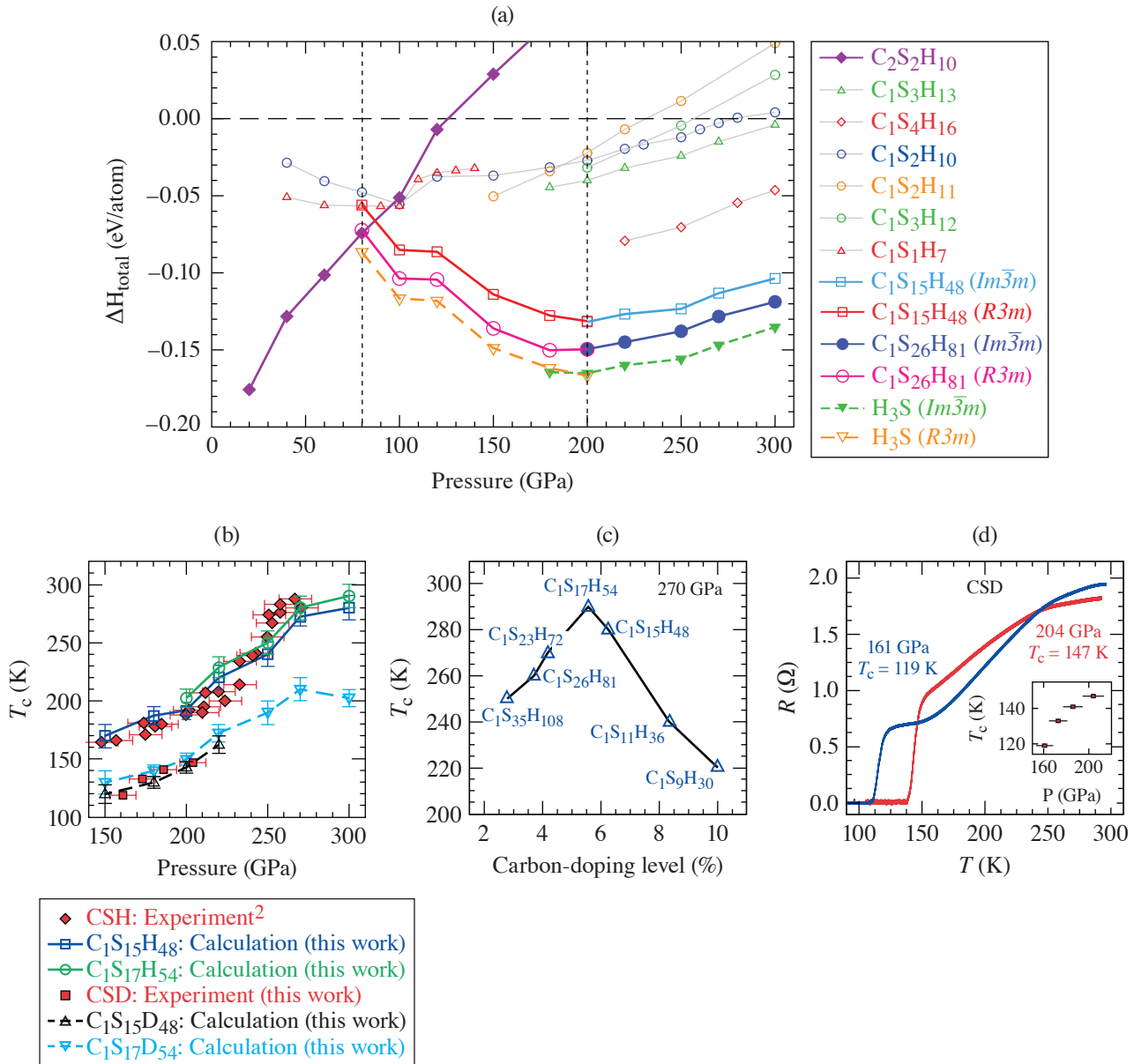
Figure 1
(a) The Convex Hull Analysis of CSH compounds: the total formation enthalpy versus pressure for different CSH compounds in the pressure range of 20 to 300 GPa. (b) The calculated superconducting transition temperature T_c versus pressure for compounds $C_1S_{15}H_{48}/C_1S_{17}H_{54}$ and $C_1S_{15}D_{48}/C_1S_{17}D_{54}$ compared to both the CSH experiment[2] and the new CSD (carbon sulfur deuterium) experiment. (c) The maximum T_c as a function of carbon doping level in different CSH compounds at the same pressure of 270 GPa. (d) The measured temperature-dependent electrical resistance of carbonaceous sulfur deuteride at high pressures, showing the superconducting transitions as high as 147 K at 204 GPa, the highest pressure measured in this experimental run. Inset: The pressure dependence of the T_c as determined by the sharp drop in electrical resistance, showing the increase in T_c with pressure.

in the diamond-anvil cell might contain around 5%–6% carbon doping that should dominantly contribute to the measured zero resistance. The new CSD experimental results in Fig. 1(d) show good agreement between CSD experiments and calculations for $C_1S_{15}H_{48}$ and $C_1S_{17}D_{54}$, and demonstrate a pronounced shift of T_c from an isotopic substitution. The substitution of deuterium lowers T_c, indicating phonon-assisted superconductivity. This is a result of carbon doping contributing more to the higher-frequency phonon mode due to its strong covalent bonding to hydrogen atoms. This leads to a significant enhancement of the logarithmic averaged phonon frequency, changing from $\omega_{ln} \sim 1010$ K at 200 GPa to $\omega_{ln} \sim 1550$ K at 270 GPa, with the transition temperature T_c being saturated at above ~270 GPa. For $C_1S_{17}D_{54}$, the logarithmic averaged phonon frequency ω_{ln} is overall lower than that of $C_1S_{17}H_{54}$ at the same pressure due to the heavier deuterium mass. This suggests that the synthesized carbonaceous sulfur hydride superconducts via an electron–phonon mechanism consistent with the BCS theory of conventional superconductors.

1. A. P. Drozdov *et al.*, Nature **525**, 73 (2015).
2. E. Snider *et al.*, Nature **586**, 373 (2020).
3. W. Cui *et al.*, Phys. Rev. B **101**, 134504 (2020).
4. Y. Sun *et al.*, Phys. Rev. B **101**, 174102 (2020).

Unraveling the Intrinsic Atomic Physics Behind X-Ray Absorption Line Shifts in Warm Dense Silicon Plasmas

V. V. Karasiev and S. X. Hu

Laboratory for Laser Energetics, University of Rochester

Accurate knowledge of radiative properties of matter in a wide range of material densities across different temperature regimes is of growing importance in many areas of research such as planetary science, astrophysics, and inertial confinement fusion (ICF).[1–4] Our current incomplete understanding of atomic physics in dense plasmas has been demonstrated by the measurements (in Refs. 5–7) of the ionization potential depression (IPD) in warm/hot dense aluminum plasmas, which have called into question the traditional continuum-lowering plasma physics models such as Ecker–Kröll[8] and Stewart–Pyatt.[9]

In this work, we develop a novel methodology based on *all-electron* density functional theory (DFT) for calculating the optical properties of warm dense plasmas of mid-Z materials in a broad range of x-ray photon energies (up to $h\nu \sim 10$ keV). To demonstrate its applicability, we have used this novel method to systematically calculate the x-ray absorption of dense silicon plasmas for a wide range of densities and temperatures ($\rho = 0.5$ to 500 g/cm^3 and $T = 5 \times 10^3$ to 10^7 K). Based on these data, a first-principles opacity table (FPOT) of silicon has been built for ICF and high-energy-density physics applications. These *ab initio* results revealed interesting trends of density/temperature–induced red-to-blue shifts of K-edge and $1s \rightarrow 2p$ absorption lines along both the isotherm and isochore. These absorption-line shifts provide a ubiquitous measure of the competition between screening of deep bound electrons and screening of outer-shell electrons due to the warm-dense-plasma environment. Our data indicate that one can use the absorption ratio of $1s \rightarrow 2p$ to K edge for characterizing thermodynamic conditions of warm dense plasmas through x-ray spectroscopy measurements coupled with DFT calculations.

These shifts for the $T = 500$-kK isotherm are summarized in Fig. 1(a) for different silicon densities [solid red and dashed curves (circles) labeled "DFT (this work)"], where the solid and dashed horizontal lines refer to the K edge and $1s \rightarrow 2p$ locations for silicon at ambient density 2.33 g/cm^3 and $T = 500$ kK. It is clearly seen that both absorption lines have the similar trend of red-to-blue shift as ρ increases. This behavior underlines the competition between electron screening and ion–ion interaction effects on the deeply bound electrons and the outer-shell electrons. Figure 1(b) shows results for the $\rho = 35$-g/cm^3 isochore [solid red and dashed curves (circles) labeled "DFT (this work)"]. Along this thermodynamic path, the deeply bounded $1s$ states move down as temperature increases as a consequence of the decreased screening by upper-bound electrons (due to thermal-induced ionization). As a result, the K edge shifts upward overall, except for an ~40-eV red shift at temperatures between 125 kK and 250 kK, shown in Fig. 1(b); meanwhile, the $1s \rightarrow 2p$ absorption line exhibits a monotonic blue shift. To further understand these interesting features, we examine the widely used continuum-lowering models. These plasma-physics models predict the IPD for a given plasma condition (density, temperature, and an ion charge state $\overline{Z}$) with respect to an isolated ion. Figure 1(a) indicates that the atomic models of Stewart–Payatt,[9] corrected Stewart–Pyatt,[10] modified ion sphere,[11] and Crowley[12] fail to predict the K-edge red shift, providing only a qualitatively correct trend for the blue shift occurring at $\rho > 50$ g/cm^3.

Finally, we plot the ratio of the $1s \rightarrow 2p$ absorption to the K-edge absorption coefficients in Figs. 1(c) and 1(d), as the function of thermodynamic conditions varies. Figure 1(c) shows this ratio peaks at $\rho \sim 5$ to 7 g/cm^3 for $T = 500$ kK, then decreases to zero as the density increases. For the constant density shown in Fig. 1(d), the ratio monotonically increases as plasma temperature increases. Guided by such DFT calculations, one can measure this absorption ratio to infer the density and temperature in experiments.
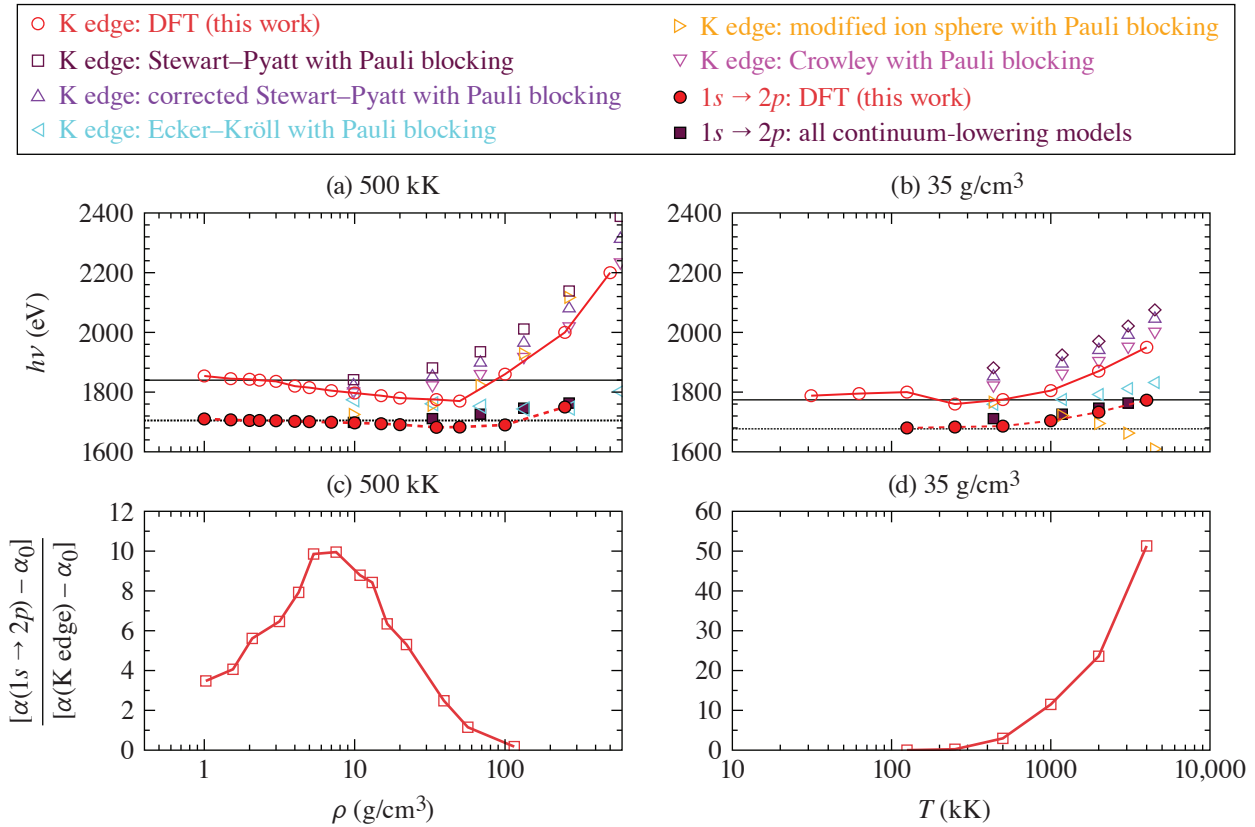
Figure 1

(a) Pressure-induced effect on the K-edge and $1s \rightarrow 2p$ absorption lines in silicon plasmas along the $T = 500$-kK isotherm; (b) temperature-induced effect on the K-edge and $1s \rightarrow 2p$ absorption line location in silicon plasmas along $\rho = 35.0$-g/cm^3 isochore; (c) the ratio of absorption coefficients between α (K–L) and α (K-edge) with subtracted L-tail background absorption α_0 along $T = 500$-kK isotherm; (d) similar to (c) for the $\rho = 35.0$-g/cm^3 isochore.

The total opacities from our DFT and astrophysical opacity table (AOT) calculations are further compared in Fig. 2. The total/gray Rosseland mean opacity K_R of Si is shown as a function of temperature for three representative cases: $\rho = 5$, 35, and 250 g/cm^3. Both DFT and AOT total opacities agree well for temperatures above a few tens of eV; however, the AOT model significantly underestimates the total opacity for $\rho = 5$ at temperatures below 10 eV. This finding is similar to the comparison between DFT and AOT for CH plasmas.[13] For densities $\rho = 35$ and 250 g/cm^3 at low temperatures (near 10 eV and below), the AOT total opacities are higher than the reference DFT values.

In conclusion, a novel free-energy DFT-based methodology has been developed that enables us to perform first-principles calculations of x-ray absorption in warm dense mid-/high-Z plasmas for a wide range of photon energies and plasma conditions. Applying the developed method to warm dense silicon plasmas, we revealed interesting red-to-blue shifts of K-edge and K–L absorption, which are explained by the competition between the free-electron screening of the K-shell core electrons and the screening of outer L-shell and M-shell electrons. Observing the fact that the relative magnitude of the K–L and K-edge absorption strongly depend on plasma environment, we propose using the ratio of $1s \rightarrow 2p$ absorption to the K-edge absorption to characterize the thermodynamic properties of dense plasmas through the x-ray spectroscopy technique. Novel methodology developed in this work was applied for systematic calculations of absorption and mean grouped opacity of silicon plasmas in a wide range of thermodynamic conditions. The resulting FPOT data were compared with the widely used AOT model. We found significant quantitative and qualitative discrepancies.

(a) 5 g/cm³ (b) 35 g/cm³ (c) 250 g/cm³

Opacity (cm²/g)

T (eV)
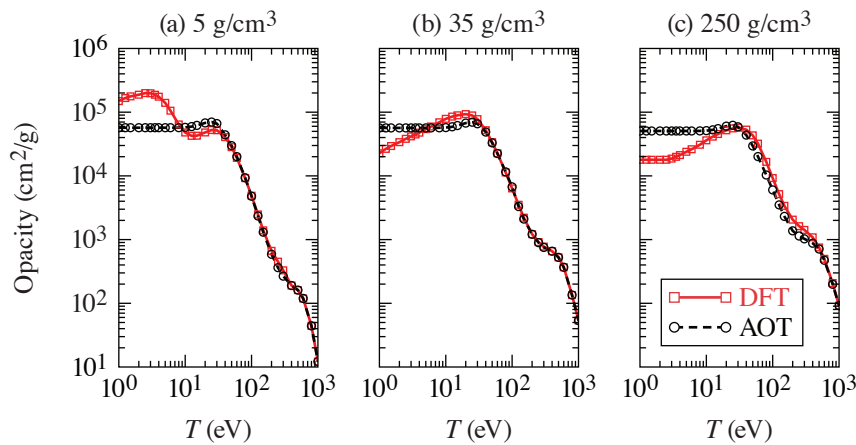
TC15624JR

Figure 2

Total Rosseland mean opacity of silicon at ρ = 5, 35, and 250 g/cm³ as a function of temperature as predicted by our first-principles DFT calculations and AOT model.

1. J. J. Fortney and N. Nettelmann, Space Sci. Rev. **152**, 423 (2010).

2. C. A. Iglesias, F. J. Rogers, and D. Saumon, Astrophys. J. Lett. **569**, L111 (2002).

3. S. X. Hu *et al.*, Phys. Rev. E **90**, 033111 (2014).

4. S. X. Hu *et al.*, Phys. Plasmas **22**, 056304 (2015).

5. O. Ciricosta *et al.*, Phys. Rev. Lett. **109**, 065002 (2012).

6. S. M. Vinko *et al.*, Nature **482**, 59 (2012).

7. D. J. Hoarty *et al.*, Phys. Rev. Lett. **110**, 265003 (2013).

8. G. Ecker and W. Kröll, Phys. Fluids **6**, 62 (1963).

9. J. C. Stewart and K. D. Pyatt, Jr., Astrophys. J. **144**, 1203 (1966).

10. B. J. B. Crowley, High Energy Density Phys. **13**, 84 (2014).

11. D. Liberman and J. Albritton, J. Quant. Spectrosc. Radiat. Transf. **51**, 197 (1994).

12. B. J. B. Crowley, Phys. Rev. A **41**, 2179 (1990).

13. S. X. Hu *et al.*, Phys. Rev. B **96**, 144203 (2017).

A Transmitted-Beam Diagnostic for the Wavelength-Tunable UV Drive Beam on OMEGA

J. Katz, D. Turnbull, B. E. Kruschwitz, A. L. Rigatti, R. Rinefierd, and D. H. Froula

Laboratory for Laser Energetics, University of Rochester

Understanding how light propagates through plasma is of great importance in many fields of physical science. In the absence of a critically dense surface, the majority of light incident into a plasma will pass through with little perturbation. Yet, much can be learned about the plasma by studying the properties of light that transmits through it. Measuring the power, spectrum, and spatial profile of transmitted light provides a means to investigate a number of key laser–plasma interactions (LPI's) such as filamentation, laser absorption, and cross-beam energy transfer (CBET). Figure 1 shows a new experimental platform developed on the OMEGA laser to explore these processes.[1] A wavelength-tunable (350- to 353-nm) UV drive beam (TOP9) has been added to OMEGA's 61st beamline in port P9 (Ref. 2) and a transmitted-beam diagnostic (P9TBD), located in the opposing port P4, characterizes the properties of the TOP9 beam after it propagates through the plasma. Together, these capabilities support a range of experiments designed to validate and constrain plasma-physics models and CBET mitigation strategies.
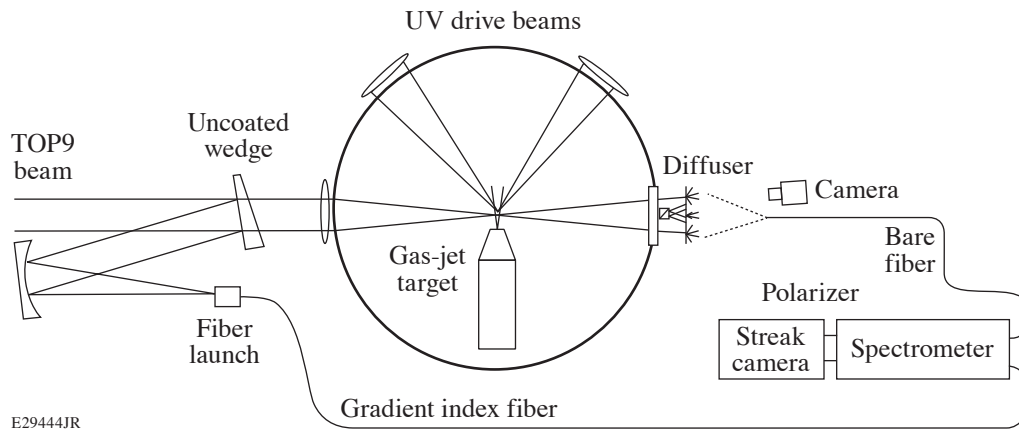
Figure 1

A charge-coupled–device (CCD) camera and fiber-coupled streaked spectrometer measure the energy, power, and near-field fluence of TOP9 after it transmits through an underdense plasma. The initial spectral power of the beam is also measured.

The P9TBD measures the energy, fluence, power, and spectrum of the TOP9 beam after it propagates through an undersense plasma. After passing through focus at target chamber center (TCC), the TOP9 beam expands and is projected on a semi-transparent diffuser. A fraction of the incident light transmits through the diffuser and forward scatters off the rear surface, generating an object that can be imaged. Internal scattering in the bulk of the 500-μm-thick diffuser limits the spatial resolution to 800-μm FWHM. Because the plasma and laser focus at TCC are small (~1 mm) and the diffuser is far away (1.9 m), a given position on the diffuser corresponds to the angle at which the light left the plasma. The vacuum window and diffuser have a 450-mm optical clear aperture that represents an f/4.2 angular field of view (Fig. 2). This allows one to observe plasma-induced refraction and filimentation[3,4] of the TOP9 beam beyond its native f/6.7 cone. A serviceable debris shield protects the thicker and more costly
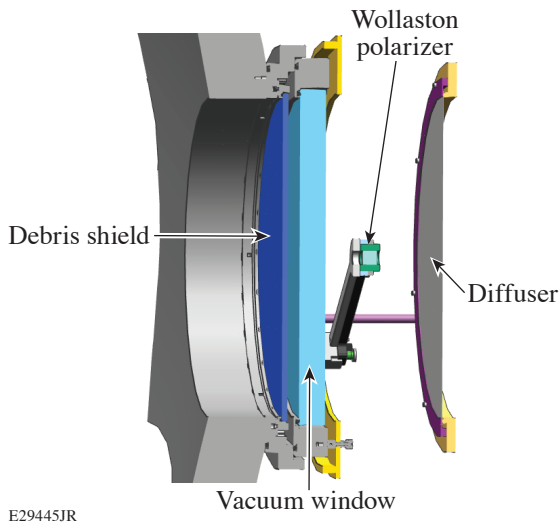
Figure 2

A cross-section view of the P4 port assembly. A 480-mm-diam debris shield protects the vacuum window and can be swapped prior to critical experiments to ensure nominal transmission through the optics. A Wollaston polarizer placed in front of the diffuser samples a 20-mm sub-aperture of the transmitted beam.

vacuum window from damage and particulate accumulation. The debris shield can be replaced prior to P9TBD experiments to restore nominal optical transmission. A Wollaston polarizer can be installed to measure the polarization of the central 20-mm subsection of the transmitted beam.

A CCD camera and imaging lens assembly is used to measure the time-integrated spatial profile of the transmitted beam (Fig. 3). The spectrally resolved power of the transmitted beam is measured using a fiber-coupled streaked spectrometer. A flat, cleaved optical fiber pointed at the center of the diffuser couples a spatially averaged sample of the incident light. The effective field of view at the diffuser plane is determined by the angular acceptance of the fiber optic. To improve sampling uniformity across the entire diffuser area, the fiber is positioned with a 3.5-m standoff distance, limiting the range of angles coupled to 0° to 3.8°. This also maintains the roll-off in sensitivity due to area foreshortening, which scales with $\cos^4(\theta)$, to a less-than-1% effect. The total power coupled into the fiber is given by $\Phi_{fiber} = \Phi_{in} \sin^2(\theta_{max}) A_f * T/A_d$, where Φ_{in} is the power incident on the diffuser, T is the diffuser transmission (0.1), A_f is the area of the fiber core (430-μm-diam core), and A_d is the diffuser area.
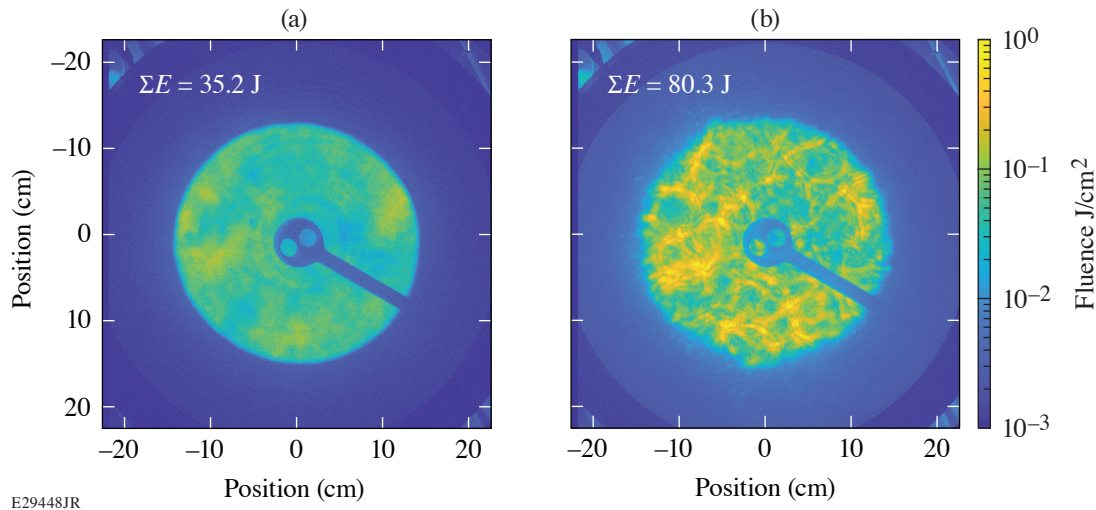
Figure 3

(a) The spatial profile of the TOP9 beam is imaged after terminating on a semi-transparent diffuser. The P9TBD instruments are photometrically calibrated to the laser system calorimetry by taking a blow-through shot with no plasma present at TCC. (b) The TOP9 beam refracted as it propagated through a preformed, underdense plasma. The spatial resolution of the recorded image corresponds to the angular distribution of energy that left TCC. In this experiment, LPI's produced high-frequency variations in the transmitted beam's intensity.

Together, this results in a coupling efficiency of $\sim 4 \times 10^{-10}$. This approach is lossy compared to an image relay but avoids issues with the high numerical apertures required to demagnify a large object onto a small fiber core.

The initial power and spectrum of the TOP9 beam are measured prior to entering the target chamber using a full-aperture, uncoated wedged optic located in front of the final focusing lens. The pickoff beam is focused into a dual-diffuser–based fiber launcher and is routed to the streaked spectrometer. Samples of both the input and transmitted beam are recorded simultaneously on the same streaked image using a custom-built multichannel fiber input head. The standard spectrometer entrance slit assembly is replaced with a V-groove array that positions up to 20 individual fibers in discrete locations offset horizontally along the axis of dispersion.

The P9TBD uses a 1.0-m-focal-length Czerny–Turner spectrograph (McPherson, 2061) and a 4320-grooves/mm grating that produces a linear dispersion of 8.0 mm/nm at the streak camera photocathode. A mask attached to the front of the V-groove array positions a series of laser-cut, vertical slits in front of each fiber face, allowing optimization of slit width for each channel. A typical streaked image, shown in Fig. 4, demonstrates P9TBD's ability to directly observe CBET, in this case from an OMEGA drive beam to the TOP9 beam. The temporal resolution of the streaked image is approximately 100-ps FWHM limited by contributions from optical path length differences from TCC to the fiber input, modal dispersion in the fiber transport, pulse-front tilt in the spectrometer, and streak camera temporal resolution.

E29449JR
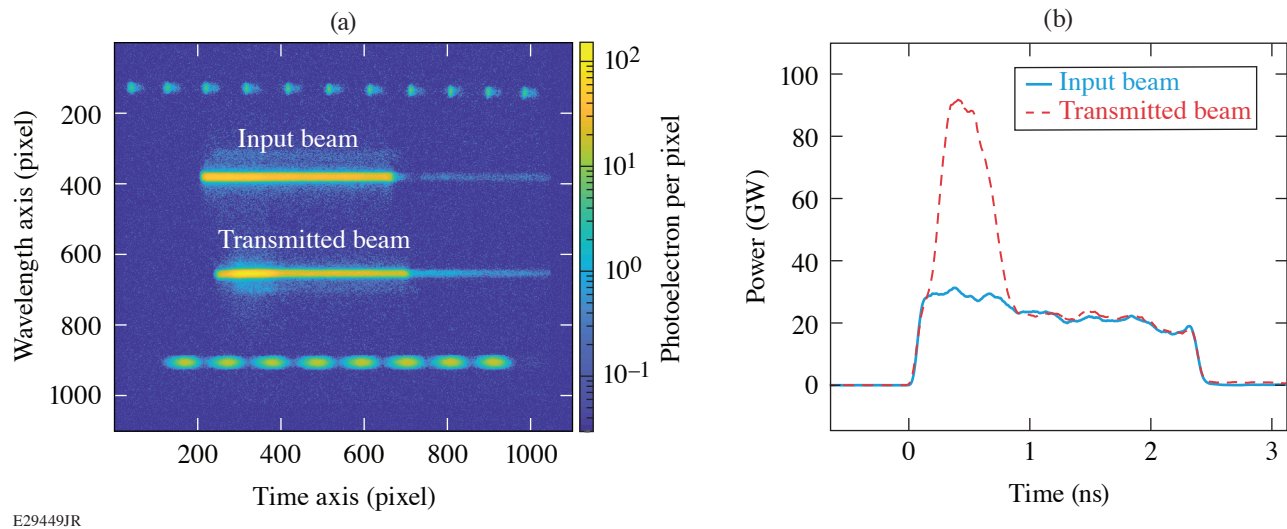
Figure 4

(a) An example of the raw data produced by the streaked spectrometer. For this shot, both channels used 500-μm slits to maximize measurement of the dynamic range. At peak power, a 100-ps time bin contains approximately 40,000 photoelectrons. (b) Cross-beam energy transfer can be measured directly by comparing the input and transmitted power of the TOP9 beam. In this experiment, a 500-ps, 0.4-TW OMEGA beam interacted with the TOP9 beam in a preformed plasma, producing 27 J of energy transfer.

The P9TBD instruments are cross-calibrated, in absolute terms, to the OMEGA EP Laser System's calorimetry by taking a full-energy shot with no plasma present at TCC [Fig. 3(a)]. This generates a calibration factor relating the total energy that leaves TCC to the total ADU's in the CCD and streaked image. Fluence and power can then be determined from the image magnification and sweep rate.

Understanding and managing LPI processes are necessary to produce deterministic and reliable plasmas. The next generation of fusion class lasers will likely make use of broadband ($\Delta \omega > 1\%$) or multicolor drive beams to mitigate CBET. TOP9 and P9TBD provide experimental access to this parameter space and a means to validate advanced LPI models. Terminating the transmitted beam onto a semi-transparent diffuser enables an imaging CCD camera and fiber-coupled streaked spectrometer to characterize its spatial profile, polarization, power, and spectrum.

1. D. Turnbull *et al.*, Nat. Phys. **16**, 181 (2020).
2. B. E. Kruschwitz *et al.*, Proc. SPIE **10898**, 1089804 (2019).
3. D. H. Froula *et al.*, Phys. Rev. Lett. **98**, 085001 (2007).
4. A. M. Hansen *et al.*, Phys. Plasmas **26**, 103110 (2019).

Reconstructing Three-Dimensional Asymmetries in Laser-Direct-Drive Implosions on OMEGA

O. M. Mannion,[1] K. W. Woo,[1] A. J. Crilly,[2] C. J. Forrest,[1] J. A. Frenje,[3] M. Gatu Johnson,[3] V. Yu. Glebov,[1] J. P. Knauer,[1] Z. L. Mohamed,[1] M. H. Romanofsky,[1] C. Stoeckl,[1] W. Theobald,[1] and S. P. Regan[1]

[1]Laboratory for Laser Energetics, University of Rochester
[2]Centre for Inertial Fusion Studies, Imperial College, UK
[3]Plasma Science and Fusion Center, Massachusetts Institute of Technology

Neutron spectroscopy is a key diagnostic tool in inertial confinement fusion experiments. The primary fusion neutron energy spectrum is used to infer the fusion yield, hot-spot apparent ion temperature, and hot-spot velocity, while the scattered neutron energy spectrum is used to infer the areal density of the compressed DT fuel. These measurements are key to understanding and identifying sources of 3-D asymmetries and the effect that these asymmetries have on target performance.

Over the past decade, a suite of neutron spectrometers have been fielded to measure the neutron energy spectrum emitted in laser-direct-drive implosions on the OMEGA laser. The detectors have been strategically positioned around the OMEGA target chamber such that each detector provides unique data that can be used to reconstruct the 3-D conditions of the compressed target. The current detector suite on OMEGA consists of neutron time-of-flight (nTOF)[1] detectors positioned along seven different lines of sight (LOS's),[2] a magnetic recoil spectrometer (MRS),[3] and two charged-particle spectrometers (CPS's).[4] The configuration of the nTOF and charged-particle spectrometers around the OMEGA target chamber is shown in Fig. 1. Measurements of the neutron energy spectrum are made using the nTOF and MRS detectors, while measurements of the knock-on deuteron spectrum are made with the CPS detectors.
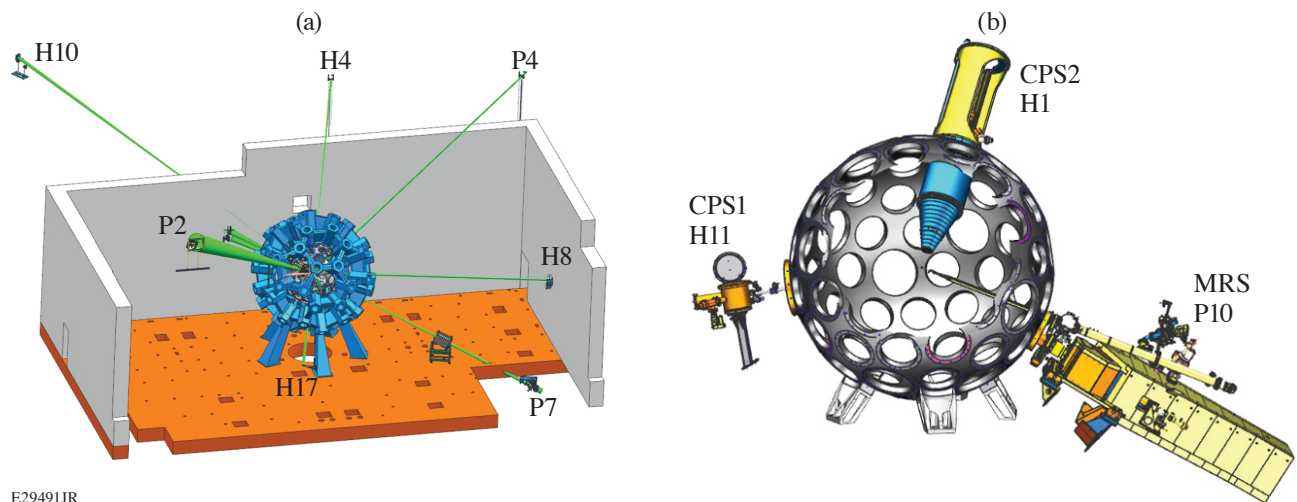
Figure 1
The lines of sight along which (a) nTOF detectors and (b) charged-particle spectrometers are fielded on OMEGA.

The neutron spectrometers on OMEGA measure either the fusion yield, apparent ion temperature, hot-spot velocity, or the areal density along a particular direction of the target. To make use of these individual LOS measurements, 3-D reconstruction algorithms have been developed[5] that combine the individual measurements into a holistic 3-D view of the hot spot and dense fuel conditions. In this work, models for the hot-spot velocity, apparent ion temperature,[6] and areal density[7] are used to fit the measured values along each LOS. Once the optimal parameters are found in each model, the results can be used to gain a greater understanding of the implosion symmetry.

The reconstruction algorithms that have been developed were applied to OMEGA shot 94660. This shot was known to have a large mode-one drive asymmetry due to anomalous laser beam-pointing errors.[8] This experiment is therefore a good candidate for testing these reconstruction algorithms since the asymmetries in the hot spot and DT fuel are exacerbated, in a known direction, and can be resolved with the current measurement uncertainties. Three-dimensional radiation-hydrodynamic simulations predict that experiments with large mode-one drive asymmetries will have large hot-spot flow velocities (>100 km/s) in the direction of the mode-one drive asymmetry.[8] Additionally, simulations predict that a large apparent ion temperature (>1.0-keV) asymmetry and areal-density asymmetry will be present and aligned with the hot-spot velocity and mode-one direction.[8–10] Therefore, we can use these experimental results to check if the reconstruction techniques are consistent with the expectation from radiation-hydrodynamic simulations.

The hot-spot velocity reconstruction for this experiment had a magnitude of 155±11 km/s. The direction of the velocity was $\theta = 74\pm6°$ and $\phi = 139\pm5°$ in the OMEGA coordinate system. This direction was nearly aligned with the direction of the known mode-one drive asymmetry,[8] $(\theta,\phi) = (51°,122°)$. The mode-one drive-asymmetry direction was determined using a hard sphere laser illumination calculation using the measured beam pointing, target offset, and laser energies on the experiment.[6]

The apparent ion temperature reconstruction was performed for this shot, and the velocity variances and covariances were determined. The square root of the reconstructed velocity covariance matrix elements were large (>100 km/s), indicating large residual motion within the hot spot. The magnitude of these values is consistent with those found in highly perturbed radiation-hydrodynamic simulations.[11] The principle eigenvector of the flow velocity's covariance matrix is along the direction $(\theta,\phi) = (53°,135°)$ and represents the direction of maximum flow-velocity variance. This direction is consistent with the direction of the hot-spot velocity reconstruction. The apparent ion temperature reconstruction is shown in Fig. 2.
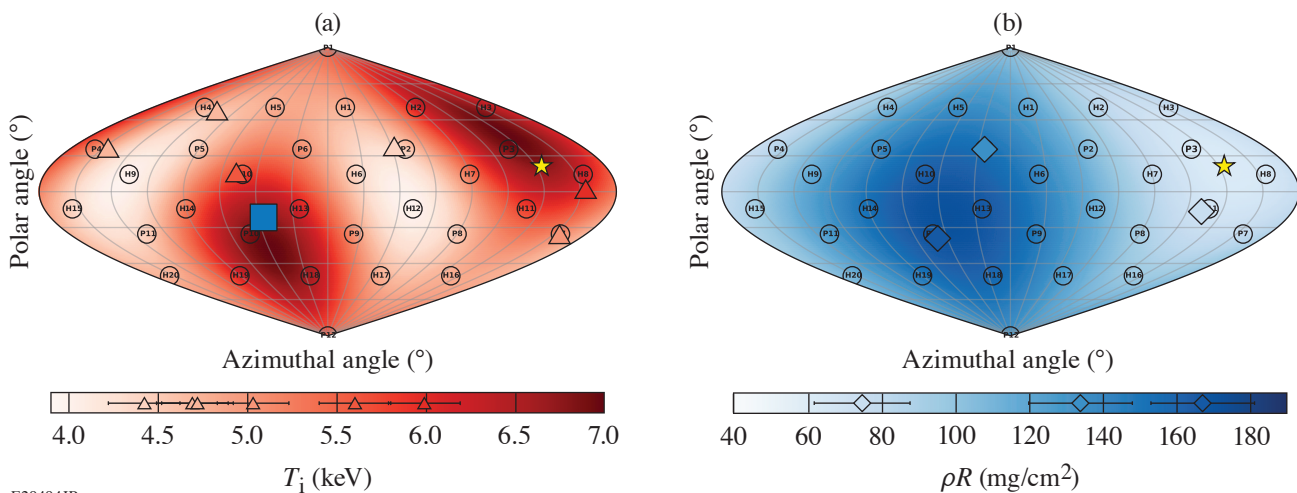
Figure 2

(a) A sinusoidal projection of the OMEGA target chamber's coordinate system showing the reconstructed hot-spot velocity direction (yellow star), the antipodal direction of the hot-spot velocity (blue square), the measured DT apparent ion temperatures (triangles), and the apparent ion temperature reconstruction (red color map) for shot 94660. (b) A sinusoidal projection of the OMEGA target chamber's coordinate system showing the reconstructed hot-spot velocity (yellow star), measured areal densities (diamonds), and areal-density reconstruction (blue color map) for shot 94660.

The areal-density reconstruction has been performed for shot 94660 and the average areal density and areal-density variation were determined. Due to the limitations of the current detector suite, a mode-one areal-density model was used, and the direction of the asymmetry was assumed to be along the direction of the hot-spot velocity. From the reconstruction, the average 4π areal density was inferred to be $\rho R_0 = 115 \pm 9$ mg/cm^2, while the variation in the areal density was found to be $\Delta\rho R = 54 \pm 12$ mg/cm^2. The areal-density reconstruction is shown in Fig. 2, where we see that the areal-density measurements are consistent with the apparent ion temperature and hot-spot velocity data.

The techniques described in this work can now be used to diagnose low-mode asymmetries in laser-direct-drive implosions on OMEGA. Future work will focus on extending these reconstructions by incorporating more measurements. In particular, recent theoretical work[11] has demonstrated that if the DD apparent ion temperature measurements are included in the apparent ion temperature reconstruction, the thermal ion temperature can be inferred. A more-general areal-density reconstruction will be developed so that the direction of the areal-density asymmetry need not be assumed along the direction of the hot-spot velocity. This will require the inclusion of more areal-density measurements. Additional areal-density measurements can be obtained from measurements of the knock-on deuteron spectrum measured by the CPS detectors already fielded on OMEGA (see Fig. 1) but will require that a more-advanced analysis of the knock-on deuteron spectrum be developed that can be used at an areal density >100 mg/cm^2.

1. R. A. Lerche *et al.*, Appl. Phys. Lett. **31**, 645 (1977).
2. O. M. Mannion *et al.*, Nucl. Instrum. Methods Phys. Res. A **964**, 163774 (2020).
3. D. T. Casey *et al.*, Rev. Sci. Instrum. **84**, 043506 (2013).
4. D. G. Hicks, "Charged Particle Spectroscopy: A New Window on Inertial Confinement Fusion," Ph.D. thesis, Massachusetts Institute of Technology, 1999.
5. O. M. Mannion *et al.*, Rev. Sci. Instrum. **92**, 033529 (2021).
6. K. M. Woo *et al.*, Phys. Plasmas **25**, 102710 (2018).
7. A. J. Crilly *et al.*, Phys. Plasmas **28**, 022710 (2021).
8. O. M. Mannion *et al.*, Phys. Plasmas **28**, 042701 (2021).
9. B. K. Spears *et al.*, Phys. Plasmas **21**, 042702 (2014).
10. K. M. Woo *et al.*, Phys. Plasmas **25**, 052704 (2018).
11. K. M. Woo *et al.*, Phys. Plasmas **27**, 062702 (2020).

Application of an Energy-Dependent Instrument Response Function to the Analysis of Neutron Time-of-Flight Data from Cryogenic DT Experiments

Z. L. Mohamed, O. M. Mannion, J. P. Knauer, C. J. Forrest, V. Yu. Glebov, and C. Stoeckl

Laboratory for Laser Energetics, University of Rochester

Neutron time-of-flight (nTOF) detectors are used to diagnose the conditions present in inertial confinement fusion (ICF) and basic laboratory physics experiments performed on an ICF platform. As detailed in Ref. 1, the instrument response function (IRF) of these detectors is constructed by the convolution of two components: an x-ray IRF and a neutron interaction response. The shape of the neutron interaction response varies with incident neutron energy, changing the shape of the total IRF. Analyses of nTOF data that span a broad range of energies must account for this energy dependence in order to accurately infer plasma parameters and nuclear properties in ICF experiments. This method is applied to synthetic data resembling symmetric cryogenic DT implosions to examine the effect of the energy-dependent IRF on the inferred areal density. Results of forward fits that infer ion temperatures and areal densities from nTOF data collected during cryogenic DT experiments on OMEGA are also discussed.

Areal density is a quantity that is used to diagnose the compressive performance of cryogenic DT ICF experiments. With the recent development of a second xylene nTOF line of sight (LOS) on OMEGA that uses the same detector design as an existing OMEGA nTOF,[2–4] an additional measurement of backscatter areal density is now available, enabling the study of implosion symmetry via variations in nTOF areal density.

Analysis of the nTOF data is conducted via forward fit. The standard forward-fit model[5] can be written as

$$V(t) = \left\{ \left[50\,\Omega \times k \times s(E) \times a(E) \times \frac{dN}{dE_{4\pi}} \frac{dE}{dt} \right] \otimes \mathrm{IRF}(E,t) \right\} + B(t), \tag{1}$$

where $V(t)$ represents the fit to the nTOF data in units of volts, k represents a charge calibration constant in units of nC/neutron, $50\,\Omega$ represents digitizer impedance, $s(E)$ represents detector sensitivity as calculated by MCNP[6] (a Monte Carlo code) simulations of the xylene detector, $a(E)$ represents beamline attenuation of neutrons as calculated using MCNP simulations of the detector and the LOS from the center of the OMEGA target chamber,[4] $dN/dE_{4\pi}$ represents the total neutron spectrum exiting the ICF target into 4π, dE/dt represents the relativistic Jacobian, IRF represents the total instrument response function, $\otimes$ represents convolution, and B is a background model. For these detectors, the background is represented by an exponential decay function and is mainly associated with the scattering of DT neutrons on structures near the detector's LOS. For cryogenic DT implosions, the energy spectrum $dN/dE_{4\pi}$ contains contributions from the DD primary, TT, and n(D,p)2n reactions as well as the neutrons that scatter elastically on D and T within either the hot spot or the cold fuel shell (i.e., nD and nT elastic single scatters). Since areal densities on OMEGA are relatively low (<350 mg/cm^2), a spectrum for multiple scatters is not currently included in this model.

The model spectra for nD and nT elastic single scatters are built such that

$$\frac{dN}{dE_{nT+nD}} = \rho L \times Y_{DT} \times \frac{\int_{3.3\,\mathrm{MeV}}^{4\,\mathrm{MeV}} \left[f_T \frac{d\sigma_{nT}}{dE} + f_D \frac{d\sigma_{nD}}{dE} \right] dE}{f_T m_T + f_D m_D}. \tag{2}$$

Note that the use of this equation assumes a point source of neutrons and uses the elastic scattering cross sections for DT neutrons on D and T. The model for the n(D,p)2n spectrum comes from the cross sections inferred in Ref. 7. This spectrum also scales with areal density and is calculated similarly to Eq. (2), but using the n(D,2n)p cross section in Ref. 7. In this model, it is assumed that the nT and nD elastic single scatters and the n(D,2n)p components represent the same areal density. An example of the total fit is shown in Fig. 1.

13-m 8 × 4 PMT D data, shot 96020
Fit from 480 to 790 ns (1.5 to 4 MeV), $\rho R \sim 70$ mg/cm^2
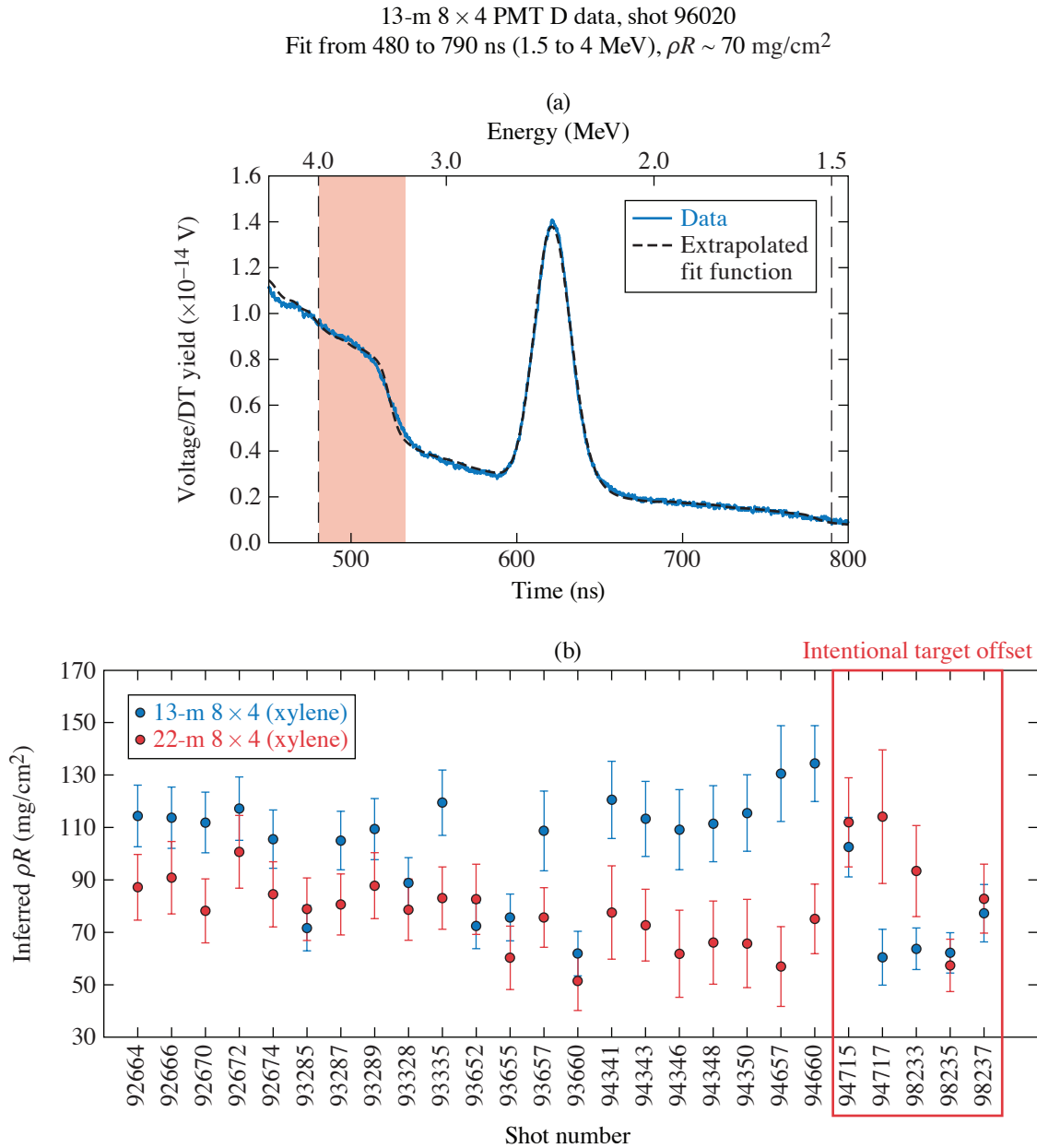
Figure 1

(a) Example of a forward fit to experimental nTOF data for the 13-m xylene detector. The blue curve represents the data while the black curve represents the fit. The vertical dashed lines indicate the range of the fit (1.5 to 4 MeV). The red shaded area represents the region in which nT and nD single-scatter components of the fit are integrated to calculate a backscatter areal density (3.5 to 4 MeV). (b) Areal densities for several shots as inferred by the forward fit outlined in this work. The 22-m LOS generally infers about 20 mg/cm^2 lower than the 13-m LOS. With imposed target offsets based on the measured flow velocities, the direction of the asymmetry can be reversed or the asymmetry can be minimized.

Recent developments in the analysis of nTOF data at the Omega Laser Facility include the analysis of a larger range of energies (1.5 to 4 MeV). Analysis over this wide range of energies allows one to more accurately determine the background, which affects the inferred spectra of nD and nT single elastic scatters. Because this analysis spans a wide range of energies, it is most accurate to use an energy-dependent IRF as detailed in Ref. 1. The final fit has six parameters. Four parameters are related to the neutron energy spectrum: DD ion temperature, DD mean energy, DD yield, and areal density. The background is modeled as an exponential decay. The remaining two parameters in the forward fit are the magnitude and time decay constant for the background. The final inferred areal density is calculated by inverting Eq. (2), where the integrated energy spectra are the best-fit spectra for the elastically scattered nD and nT neutrons. Note that this analysis focuses on the backscattered nT neutrons by integrating over 3.3 to 4 MeV.

This analysis has been benchmarked using synthetic data that represent symmetric, isobaric implosions. The neutron energy spectra were generated using an ice block model in *IRIS3D*.[8] Synthetic nTOF data were then generated using Eq. (1) along with these energy spectra. The data set involved here represents isobaric 2-keV implosions with areal densities from 50 to 250 mg/cm^2. The forward fits to the synthetic data were carried out using the method that was previously detailed, which is also applied to experimental data.

The forward-fit analysis with an energy-dependent IRF recovers the ρL calculated directly from the *IRIS3D* energy spectra almost exactly. If either the 2.45-MeV or 3.5-MeV monoenergetic IRF is used, ~2%–3% inaccuracy is introduced. This is a relatively small inaccuracy with the current analysis, which spans 1.5 to 4 MeV, because the only sharp features within this region are the DD signal (2.45 MeV) and the nT edge (3.5 MeV), which are relatively close in energy. For these detectors, the difference in the width of the IRF's is relatively small between 2.45 and 3.5 MeV (~0.7-ns difference in FWHM). The inaccuracy introduced with the use of a monoenergetic IRF is expected to grow substantially if the range of the fit is extended to 9 MeV, although the exact magnitude of the effect has not yet been predicted because a more-advanced energy spectrum model and a different method of determining the background will likely be required to reach this goal.

The forward fit described above is designed to be applicable for approximately symmetric implosions; however, asymmetric implosions can be more complicated. Since the n(D,p)2n spectrum is known to be forward-peaked while this analysis focuses on the elastically backscattered nD and nT neutrons, these spectra may not scale by the same areal densities as this analysis assumes. It is assumed that the differences between the realistic asymmetric spectrum and the modeled symmetric spectrum will go into the "background" component of the fit. It is for this reason that the background is not fixed. Changes in the background (i.e., background from environmental scattering + any asymmetric contributions) have been observed in experimental data.

The current analysis using the fit for background parameters along with the symmetric nD and nT elastic scatter and n(D,2n)p models has been applied to cryogenic data dating back to early 2019 (when the second nTOF LOS came online on OMEGA). With the standard beam-pointing procedure and no imposed target offset, the 22-m LOS, which views part of the lower hemisphere of the target, sees an average of 20 mg/cm^2 lower areal densities than the 13-m LOS, which views part of the upper hemisphere of the target. Variations in these inferred nTOF areal densities are consistent with measured variations in ion temperature.[9] As shown in Fig. 1, this trend has been reversed with intentionally imposed target offsets based on measured flow velocities. In other instances, strategic target offsets based on flow velocity[9,10] have been used to minimize the areal-density asymmetry. The ability to minimize or reverse the direction of the areal-density asymmetry indicates that the areal-density measurement responds as expected when a mode-one perturbation is minimized or reversed in direction. These instances of minimized differences in areal densities along the two LOS correspond to shots with minimal ion temperature asymmetries as well as flow velocities.[10]

Future work will include further benchmarking of this analysis with asymmetric synthetic data. This will test the current handling of the background as well as the scaling of the different components [i.e., nT elastic scatters versus nD elastic scatters versus n(D,2n)p, which originate from different parts of the shell] and should additionally reveal any sensitivities of the current analysis to the exact shape of the nT, nD, and n(D,2n)p spectra under asymmetric conditions.

1. Z. L. Mohamed *et al.*, J. Appl. Phys. **128**, 214501 (2020).
2. C. Stoeckl *et al.*, Rev. Sci. Instrum. **81**, 10D302 (2010).
3. V. Yu. Glebov *et al.*, Rev. Sci. Instrum. **85**, 11E102 (2014).
4. C. J. Forrest *et al.*, Nucl. Instrum. Methods Phys. Res. A **888**, 169 (2018).
5. R. Hatarik *et al.*, J. Appl. Phys. **118**, 184502 (2015).
6. X-5 Monte Carlo Team, Los Alamos National Laboratory, Los Alamos, NM, Report LA-UR-03-1987 (2008).
7. C. J. Forrest *et al.*, Phys. Rev. C **100**, 034001 (2019).
8. F. Weilacher, P. B. Radha, and C. Forrest, Phys. Plasmas **25**, 042704 (2018).
9. O. M. Mannion *et al.*, Rev. Sci. Instrum. **92**, 033529 (2021).
10. O. M. Mannion *et al.*, Nucl. Instrum. Methods Phys. Res. A **964**, 163774 (2020).

The Scattered-Light Time-History Diagnostic Suite at the National Ignition Facility

M. J. Rosenberg,[1] J. E. Hernandez,[2] N. Butler,[2] T. Filkins,[1] R. E. Bahr,[1] R. K. Junguist,[1] M. Bedzyk,[1] G. Swadling,[2] J. S. Ross,[2] P. Michel,[2] N. Lemos,[2] J. Eichmiller,[2] R. Sommers,[2] P. Nyholm,[2] R. Boni,[1] J. A. Marozas,[1] R. S. Craxton,[1] P. W. McKenty,[1] A. Sharma,[1] P. B. Radha,[1] D. H. Froula,[1] P. Datte,[2] M. Gorman,[2] J. D. Moody,[2] J. M. Heinmiller,[3] J. Fornes,[3] P. Hillyard,[3] and S. P. Regan[1]

[1]Laboratory for Laser Energetics, University of Rochester
[2]Lawrence Livermore National Laboratory
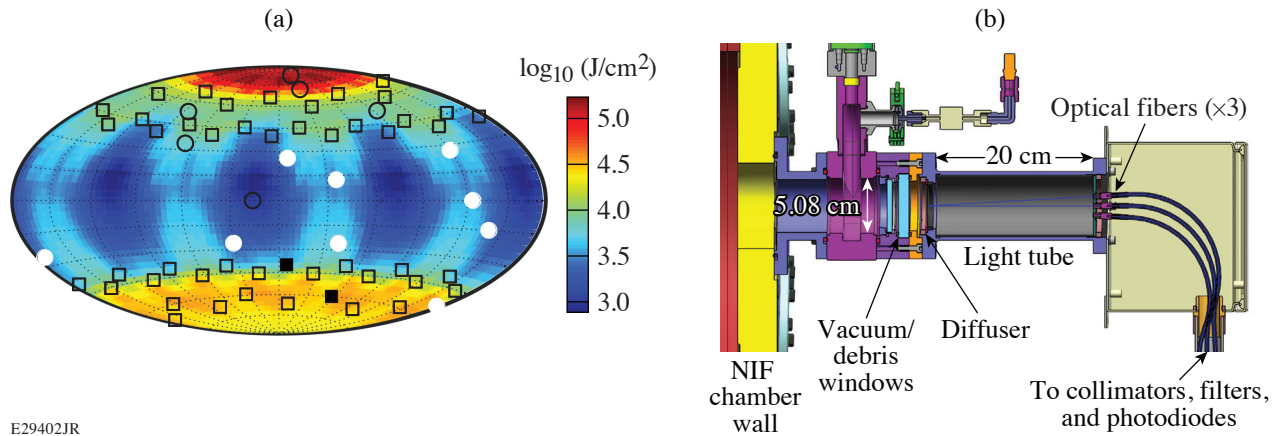[3]Nevada National Security Site

Measurements of scattered light are important diagnostics of laser energy coupling and laser–plasma instabilities (LPI's) such as stimulated Brillouin scattering (SBS), stimulated Raman scattering (SRS), or two-plasmon decay (TPD) in inertial confinement fusion (ICF) experiments. At the National Ignition Facility (NIF), scattered-light diagnostics were originally implemented only at limited beam-port (or "quad," collections of four beams) locations, and extrapolation to total scattered light is predicated on assumptions of predominantly backscattered light and symmetry in polar and azimuthal angles, which may not be valid. For polar-direct-drive (PDD) experiments in particular, the existing diagnostics are not adequate to capture the variation in scattered light.

These considerations motivate additional scattered-light measurements between beam ports to infer the total scattered-light distribution. Therefore, the scattered light time-history diagnostic (SLTD) has been developed to measure the time-resolved scattered light in three different wavelength bands—350 to 352 nm (SBS), 430 to 760 nm (SRS), and 695 to 745 nm ($\omega/2$, corresponding to SRS- or TPD-related scattered light at the quarter-critical density)—at 15 locations around the NIF target chamber outside the NIF beam-port envelope.

Figure 1(a) shows the simulated distribution of SBS scattered light in an example PDD implosion, the locations of NIF beam ports, and the locations of the SLTD suite. Figure 1(b) shows a schematic of the instrument. Light enters the SLTD through a set of vacuum and debris windows and is incident on an optical diffuser after being apertured down to a diameter of 5.08 cm. The 250-μm-thick diffuser, which is located around 590 cm from target chamber center, disperses the light forward in a near-Lambertian distribution with a transmission around 0.2. Three optical fibers positioned 20 cm from the diffuser, with a numerical aperture of 0.22 and a 400-μm core diameter, capture the light from the entire surface of the diffuser. The light is contained within a light tube coated black on the interior to minimize multiple reflections.

The light is transported through 2 m of fiber and relayed by a collimator through a set of bandpass filters that differentiate the three channels. The SRS channel is additionally filtered by a flattening filter with a wavelength-dependent transmission (0.1 at 532 nm) that compensates for the wavelength-dependent transmission of the diffuser and sensitivity of the photodiode. Neutral-density (ND) filters are also used to control light fluence on the photodiodes and are individually calibrated. The collimation system was designed so that the projected beam underfills the 10-mm-diam active area of the photodiodes. Filter and collimator transmissions were measured at the appropriate wavelengths and used in the overall photometric calculations.

Hamamatsu R1328U-52 and R1328U-53 fast photodiodes, with 60-ps rise and 90-ps fall times, detect the light over the wavelength bands of interest. Photodiode sensitivity ranges from ~65 mA/W at 351 nm for the SBS channel to ~4 mA/W at 730 nm for the SRS and $\omega/2$ channels and are calibrated individually. Current from the photodiodes is carried by coaxial cables (LMR400 or

(a)

(b)

Optical fibers (×3)

20 cm

5.08 cm

Light tube

Vacuum/ debris windows

Diffuser

NIF chamber wall

To collimators, filters, and photodiodes

E29402JR

log$_{10}$ (J/cm^2)

5.0
4.5
4.0
3.5
3.0

Figure 1
(a) Simulated distribution of SBS scattered light for a PDD experiment overlaid with the NIF laser quad port map (squares). Existing full-aperture backscatter stations are located in two quads (solid black squares), while SLTD's (circles) are being implemented. Out of an eventual 15 SLTD's, a total of six (black circles) have been implemented to date. (b) SLTD optical components include an optical diffuser and optical fibers at the back of a light tube assembly that relay the light to filtered photodiodes.

LMR600) over a distance of 35 to 65 m to a Tektronix MSO58LP 1-GHz digitizer with 12-bit resolution. The digitizer response determines the temporal resolution of the SLTD. The SLTD was designed to achieve measurement accuracy of better than ±15%, temporal resolution of 1.5 ns, and a signal-to-noise ratio >100.

The integrated throughput of the SLTD optical components, including the vacuum and debris windows, diffuser, light tube, and optical fibers, was calibrated at 532 nm using a 200-mJ, 5-ns pulsed source. The throughput was measured to be $5.93\pm0.41 \times 10^{-7}$ at 532 nm. Calibration of other SLTD components, including the filters, collimators, and photodiodes, was conducted individually using wavelength-tunable continuous sources between 300 and 800 nm. The total sensitivity of each channel, in terms of volts measured on the oscilloscope per watt incident on SLTD, before accounting for ND filters, is approximately 6.7×10^{-7} V/W (SBS), 6.7×10^{-8} V/W (SRS), and 1.8×10^{-7} V/W (ω/2).

The first six SLTD units, positioned between polar angles of $\theta = 7°$ and 90°, have collected data on a variety of NIF shots. A collection of sample data from the unit at $\theta = 18°$ is shown in Fig. 2, including SBS signal from PDD shot N200715-002, SRS signal from indirect-drive shot N200727-001, and ω/2 signal from x-ray diffraction shot N191016-001. The data demonstrate that requirements on temporal resolution and dynamic range or signal-to-noise ratio are satisfied.

(a) SBS
N200715-002

(b) SRS
N200727-001

(c) ω/2
N191016-001
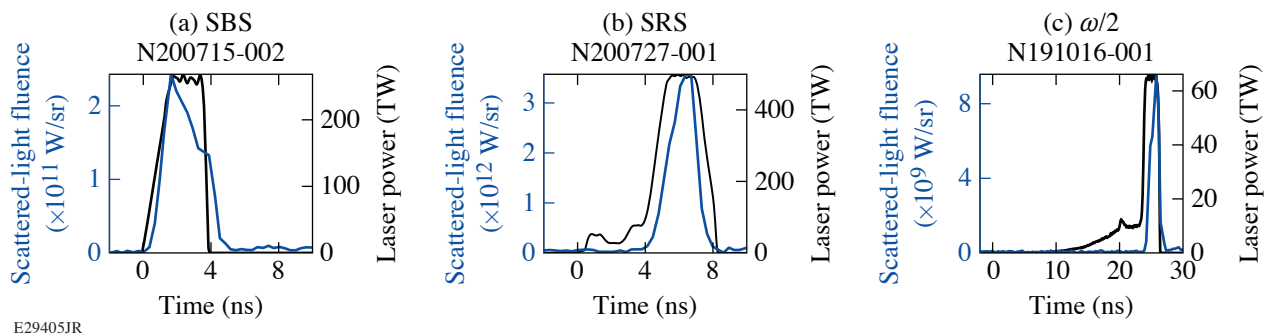
E29405JR

Figure 2
SLTD data obtained at $\theta = 18°$ on different NIF experiments in the (a) SBS, (b) SRS, and (c) ω/2 channels. The SLTD trace (blue curve) is overlaid with the total laser power (black curve).

On a given shot, SLTD data can be used to map out the angular dependence of the scattered-light distribution with an uncertainty in each measurement of ±9%. The measurements can be used to evaluate the relative angular distribution in radiation-hydrodynamic calculations of ICF implosions. A comparison of shot N200715-002 SBS data to *SAGE* calculations of unabsorbed light shows qualitative agreement in the relative angular variation, with a peak near $\theta = 40°$ and less unabsorbed light near the pole and equator, although with some quantitative differences in the trends.

In summary, the NIF SLTD suite is being implemented to diagnose time-resolved scattered light in three wavelength bands—SBS, SRS, and $\omega/2$. Six units have collected data, validating the diagnostic performance. Nine additional units will be installed. The SLTD suite will constrain models of laser energy coupling and LPI in direct-drive and indirect-drive ICF experiments.

Characterization of Partially Deuterated KDP Crystals Using Two-Wavelength Phase-Matching Angles

C. Dorrer, I. A. Begishev, S.-W. Bahk, and J. Bromage

Laboratory for Laser Energetics, University of Rochester

Large-aperture partially deuterated KDP crystals enable high-energy broadband parametric amplifiers pumped by frequency-converted, high-energy nanosecond Nd:glass lasers, opening the way for the generation of optical pulses with energy of hundreds of joules and bandwidth supporting sub-20-fs pulses.[1–5] The optimal noncollinear angle between signal and pump beams for broadband gain depends on the deuteration level. This optimization is practically difficult because of uncertainties in the deuteration level of grown DKDP crystals, as well as in the models used to calculate the wavelength-dependent and deuteration-dependent optical indices that are required for phase-matching calculations.

We present the concept and application of a novel two-wavelength phase-matching technique that precisely determines the deuteration level of a DKDP crystal consistent with known index models. The determined deuteration level and model are the much-needed combination required for performance modeling and experimental optimization of an optical parametric amplifier (OPA). By experimentally determining the deuteration level of a crystal consistent with a specific index model, the described technique allows for more-accurate performance simulations as well as better identification of optimal phase-matching conditions for experimental implementation.

Determining a deuteration level consistent with a specific index model relies on the measurements of phase-matching angles at two different wavelengths [Fig. 1(a)]. Combined monochromatic sources at λ_1 and λ_2 are used as the OPA seed to facilitate the measurement of the gain as a function of phase-matching angle and allow one to directly determine the crystal's deuteration
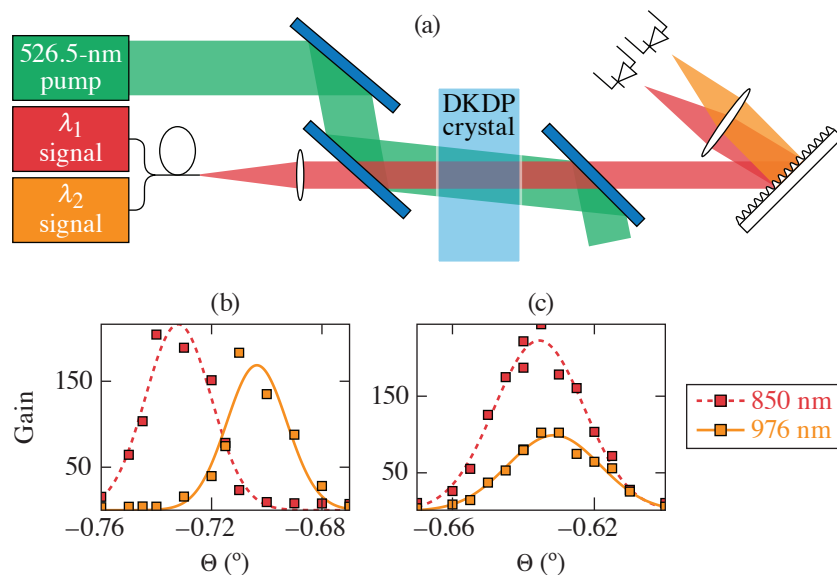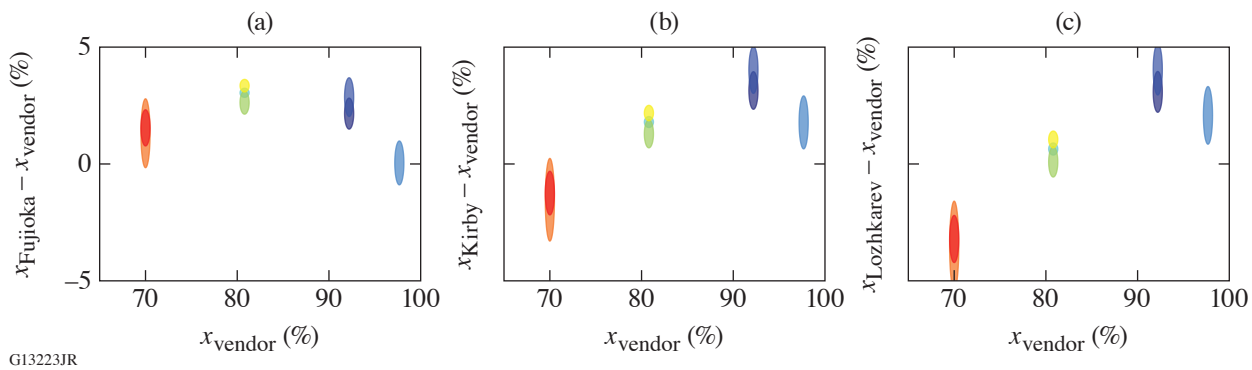

Figure 1
(a) Layout of the experimental setup. [(b),(c)] Measured gain versus rotation-stage angle for one crystal at $\alpha = 0.49°$ and $\alpha = 0.61°$, respectively. The data at each wavelength (squares) are fitted by a Gaussian function (solid and dashed curves).

level. Indeed, simulations and analysis of the phase-matching conditions for a noncollinear OPA show that there is a one-to-one relation between the difference $\theta_1-\theta_2$ in phase-matching angles and the deuteration level x for a given noncollinear angle and index model. Examples of measured small-signal gain curves at two wavelengths as a function of the crystal angle relative to normal incidence are shown in Fig. 1(b). For each wavelength, the optimal angle for phase matching is determined by fitting the data with a Gaussian function. The deuteration level consistent with the measured angle difference and a specific index model is then determined, as well as a confidence interval obtained from the fitting routines. The ordinary and extraordinary indices of DKDP are determined as a function of wavelength and deuteration level using interpolation or extrapolation of indices calculated from Sellmeier equations. These equations originate either from the Kirby model for non-deuterated KDP and 96% DKDP,[6] the combination of the Kirby model for 96% DKDP with the Zernike model for KDP (used for studies of broadband phase-matching in DKDP by Webb et al.[7] and then applied to broadband parametric amplification by Lozhkarev et al.[8]), or the Fujioka model for DKDP at various deuteration levels.[9]

Four DKDP crystals with a nominal deuteration level ranging from 70% to 98% have been characterized. For each crystal, a noncollinear angle was calculated using the nominal deuteration level and Fujioka index model to phase-match the two cw wavelengths at the same crystal angle. The actual difference in phase-matching angle $\theta_1-\theta_2$ measured during a first campaign was used to determine the deuteration level that is consistent with the data for each index model [see, for example, Fig. 1(b)]. For some crystals, an updated noncollinear angle was calculated from the determined deuteration level for $\theta_1-\theta_2 = 0$ and used for a second measurement campaign [see, for example, Fig. 1(c)]. Figure 2 presents the difference between the determined deuteration levels $x_{Fujioka}$, x_{Kirby}, and $x_{Lozhkarev}$ and the deuteration level x_{vendor} determined by the crystal's vendor from pycnometer measurements performed on the solution during crystal growth. The length of each marker in the vertical direction indicates the 95% confidence interval on the deuteration level determined during each campaign, which is 1.4% on average. The results show excellent consistency between campaigns. Whereas different models yield different deuteration levels from the same measured data, the calculated gain properties for a specific model and the corresponding deuteration level are in excellent agreement between models. This experimental technique has supported the development of broadband gain models and the determination of optimal phase-matching conditions for high-energy amplification on the MTW-OPAL Laser System, an optical parametric amplifier line (OPAL) pumped by the Multi-Terawatt (MTW) laser at the Laboratory for Laser Energetics.[5]

G13223JR

Figure 2
Determined deuteration level for the four crystals over eight campaigns using the index model from (a) Fujioka, (b) Kirby, and (c) Lozhkarev.

1. I. N. Ross et al., Opt. Commun. **144**, 125 (1997).

2. N. F. Andreev et al., J. Exp. Theor. Phys. Lett. **79**, 144 (2004).

3. O. V. Chekhlov et al., Opt. Lett. **31**, 3665 (2006).

4. V. V. Lozhkarev et al., Laser Phys. Lett. **4**, 421 (2007).

5. J. Bromage *et al.*, High Power Laser Sci. Eng. **7**, e4 (2019).

6. K. W. Kirby and L. G. DeShazer, J. Opt. Soc. Am. B **4**, 1072 (1987).

7. M. S. Webb, D. Eimerl, and S. P. Velsko, J. Opt. Soc. Am. B **9**, 1118 (1992).

8. V. V. Lozhkarev *et al.*, Laser Phys. **15**, 1319 (2005).

9. K. Fujioka *et al.*, J. Appl. Phys. **117**, 093103 (2015); **119**, 249902(E) (2016).

High-Efficiency, Fifth-Harmonic Generation of a Joule-Level Neodymium Laser in a Large-Aperture Ammonium Dihydrogen Phosphate Crystal

I. A. Begishev,[1] G. Brent,[1] S. Carey,[1] R. Chapman,[1] I. A. Kulagin,[2] M. H. Romanofsky,[1] M. J. Shoup III,[1] J. D. Zuegel,[1] and J. Bromage[1]

[1]Laboratory for Laser Energetics, University of Rochester
[2]Independent researcher

High-energy deep UV sources are required for high-density plasma diagnostics. The fifth-harmonic generation (5HG) of large-aperture neodymium lasers in ammonium dihydrogen phosphate (ADP) can significantly increase UV energies due to the availability of large ADP crystals. Noncritical phase matching in ADP for ($\omega + 4\omega$) was achieved by cooling a 65- $\times$ 65-mm crystal in a two-chamber cryostat to 200 K. The cryostat used helium as the thermally conductive medium between the crystal and the internal crystal chamber, which was surrounded by the high-vacuum external chamber with a liquid nitrogen reservoir. A temperature variation of 0.2 K across the crystal aperture was obtained. The total conversion efficiency from the fundamental to the fifth harmonic at 211 nm was 26%.

The higher harmonic provides better penetration of the plasma. An estimated 5ω beam energy of 10 J requires a large-aperture laser and, accordingly, large crystals. Recently we demonstrated a record 5HG efficiency of 30%, producing 335 mJ at 211 nm in a 12- $\times$ 12- mm beam, using a cesium lithium borate (CLBO) crystal.[1] CLBO has high second-order nonlinearity, can be grown in a relatively large size, and is phase matched at room temperature. Although a CLBO boule could be grown up to $146 \times 132 \times 118$ mm (Ref. 2), practically, the size of a finished optic does not exceed 5 cm. Furthermore, the extremely hygroscopic property of CLBO crystals requires that they be at high temperatures (~120°C). Finally, the cost of manufacturing large CLBO crystals is prohibitive for many applications. ADP crystals, which can be easily grown to much larger sizes, are an alternative way of generating a high-energy beam at 211 nm.

Potassium dihydrogen phosphate (KDP) and ADP crystals are popular nonlinear crystals because of their good nonlinear properties, wide range of transmission, and large sizes. For cascade 5HG, however, they have a significant limitation: phase-matching conditions for sum–frequency generation are not met at room temperature. Noncritical phase-matching conditions could be reached by cooling crystals to –140°C (KDP) and –70°C (ADP). This is not trivial, especially for large-aperture crystals, because a definite temperature must be strictly stabilized and maintained across the entire crystal. Any holder that keeps a crystal in a vacuum chamber and maintains the crystal temperature through thermally conductive contacts provides some temperature gradient across the crystal. The most effective way to stabilize an entire crystal at low temperature is a two-chamber cryostat.[3] In our two-chamber cryostat, shown in Fig. 1(a), the tank with liquid nitrogen is connected to the internal chamber through the solid copper (upper) and the hollow stainless-steel (lower) cylinders. The lower hollow cylinder has two 50-W flexible Kapton insulated heaters mounted on the outside surfaces to stabilize the internal chamber temperature. The internal chamber contains the crystal holder with minimized contacts with the crystal to improve the cooling uniformity from the 1 atm of helium that surrounds the crystal. Helium, the main thermal agent between the internal chamber and the crystal, was chosen because of its high (compared with other gases) thermal conductivity. Three silicon diode cryostat temperature sensors are located on two outside points of the internal chamber and on one side of the crystal inside the internal chamber. Two 120-mm-diam, 10-mm-thick fused-silica windows are located on opposite sides of the internal chamber coaxially to the crystal to pass input and output beams.

G13024JR
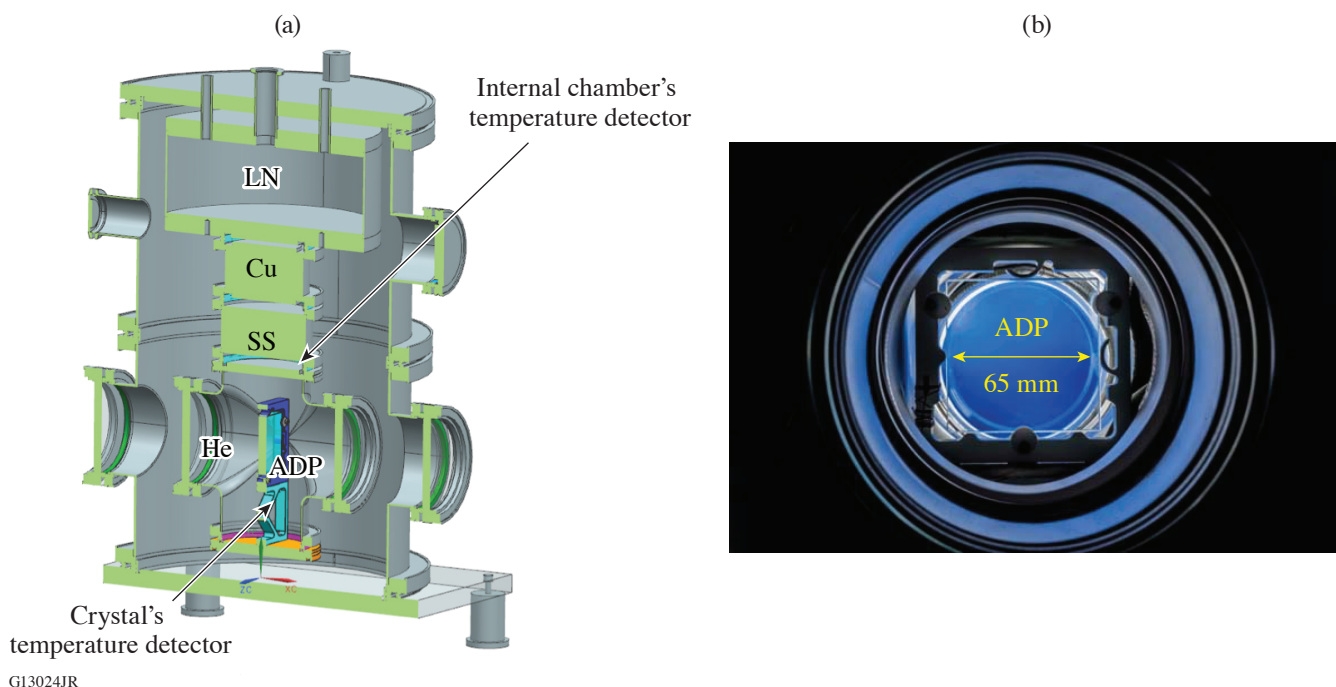
Figure 1

(a) The cross section of the two-chamber cryostat with the liquid nitrogen tank (LN), the copper cylinder (Cu), the stainless-steel cylinder (SS), and the internal chamber filled with helium (He) with an ADP crystal inside; (b) a photo of an ADP crystal inside the two-chamber cryostat through two input windows.

"Cold flow" goes down from the liquid nitrogen tank to the internal chamber; it then reaches the crystal through the helium. As soon as the temperature of the crystal reaches a chosen set point temperature, the heaters begin working to maintain that temperature through a temperature-stabilization loop with 0.01°C resolution controlled by a proportional integral derivative feedback loop. The feedback continually adjusts the output power to the heaters in order to keep the chosen temperature constant. The system has high thermal mass and reaches the target 200 K temperature in about 36 h.

The internal chamber is installed into the external chamber, which is pumped down to a vacuum of better than 5×10^{-7} Torr. The external chamber also has input and output windows, so the two-chamber cryostat has a total of four windows. The two input windows have sol-gel antireflection (AR) coatings at 266 nm (4ω), while the output windows are coated at 211 nm (5ω). The ADP crystal ($65 \times 65 \times 10$ mm, type I, $\theta = 90°$, $\phi = 45°$) has AR coatings at $l\omega$ and 4ω on the input face and an uncoated output face.

A special heavy-duty rotation stage was designed and fabricated to carry this large, heavy two-chamber cryostat and rotate it within an angular range of 5° with microradian accuracy. As a result, phase matching could be tuned by both crystal temperature and angle.

The thermal model was developed based on COMSOL Multiphysics® and was able to predict the lowest-reachable temperature of 170 K and the cooling time to reach that temperature.

There are two possible frequency-conversion schemes to optimize 5HG in a cascade of three nonlinear crystals, remembering that no type-II phase matching for 4HG (fourth-harmonic generation) and 5HG exists in KDP and ADP: $o_1o_1 \rightarrow e_2{:}o_2o_2 \rightarrow e_4{:}o_1o_4 \rightarrow e_5$ and $o_1e_1 \rightarrow e_2{:}o_2o_2 \rightarrow e_4{:}o_1o_4 \rightarrow e_5$, where o and e are ordinary and extraordinary waves in crystals. In the first case, we must detune sum-harmonic generation (SHG) down from the maximum by adjusting the length of the first crystal, while two

other processes (4HG and 5HG) should be maximized. In the second case, the required energy distribution between orthogonal polarizations could be set by rotating the input beam polarization. Here the energy distribution is adjustable for any given input energy, making the second case preferable.

The angle α between input-beam polarization and the horizontal plane was tuned by a half-λ wave plate in front of the first crystal. It changes the balance of energy between the ordinary and extraordinary axes in the first type-II doubler and preserves some fraction of the fundamental frequency beam through the first two crystals for the interaction in the last crystal. The first frequency doubler was a deuterated potassium dihydrogen phosphate (DKDP) crystal ($30 \times 30 \times 27$ mm), which was chosen instead of KDP to decrease linear absorption at the fundamental frequency. It was cut in a type-II configuration to convert $1\omega \rightarrow 2\omega$. A second frequency doubler, a type-I KDP crystal ($30 \times 30 \times 15.5$ mm), was used to convert $2\omega \rightarrow 4\omega$. The final crystal, made of ADP, was located at the image plane of a Nd:YLF laser[4] that was optimized to produce a flattopped, square-beam profile with a square pulse (1053 nm, 12×12 mm, from 1 ns to 2.8 ns, $\leq$1.5 J, 5 Hz, 0.1 Hz, or a single shot). A fused-silica prism separates the harmonic beams in space. The input and output beam energies were measured using identical cross-calibrated pyroelectric energy meters.

We reached 5HG at –73°C (200 K). The temperature acceptance of 5HG in ADP at a fixed crystal angle was measured (see Fig. 2). Each point was taken without temperature stabilization at a given temperature: 5ω energy was measured while the temperature of the ADP crystal was slowly drifting. "Red" data were taken while the crystal temperature was increasing, and "blue" data were taken while crystal temperature was decreasing. Note that the red curve was shifted down by 0.87 K to match the blue curve. This difference likely comes from the temperature gradient without stabilization and system lag because of the thermal mass.
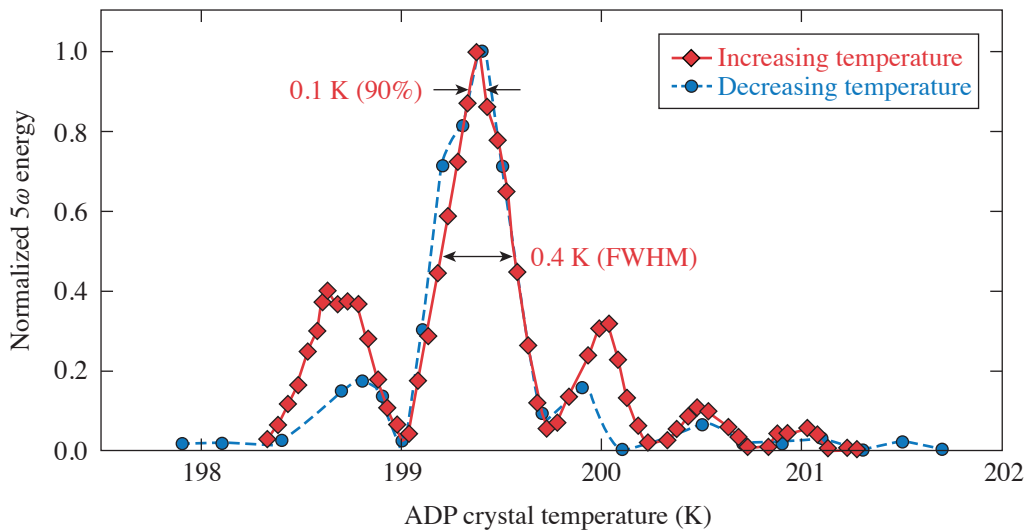
E28202JR

Figure 2
Fifth-harmonic energy temperature (T) acceptance at a fixed position angle of the ADP crystal.

An important point here is that the temperature acceptance is only 0.4 K (FWHM). To keep the system close to the maximum (>90%) of 5HG efficiency, an ADP crystal must be temperature stabilized with an accuracy better than 0.1 K. Figure 3 shows beam profiles of the input beam at the fundamental frequency (a) before the first crystals and (b) fifth-harmonic beam after the cryostat. Compared to the relatively uniform 1ω beam, the 5ω beam is slightly more spatially varied. Some residual radial nonuniformity of the 5ω beam was caused by a small phase mismatch inside the ADP crystal and corresponds to a temperature gradient over the ADP crystal. Overall conversion efficiency could be better with improved temperature uniformity of the ADP crystal.
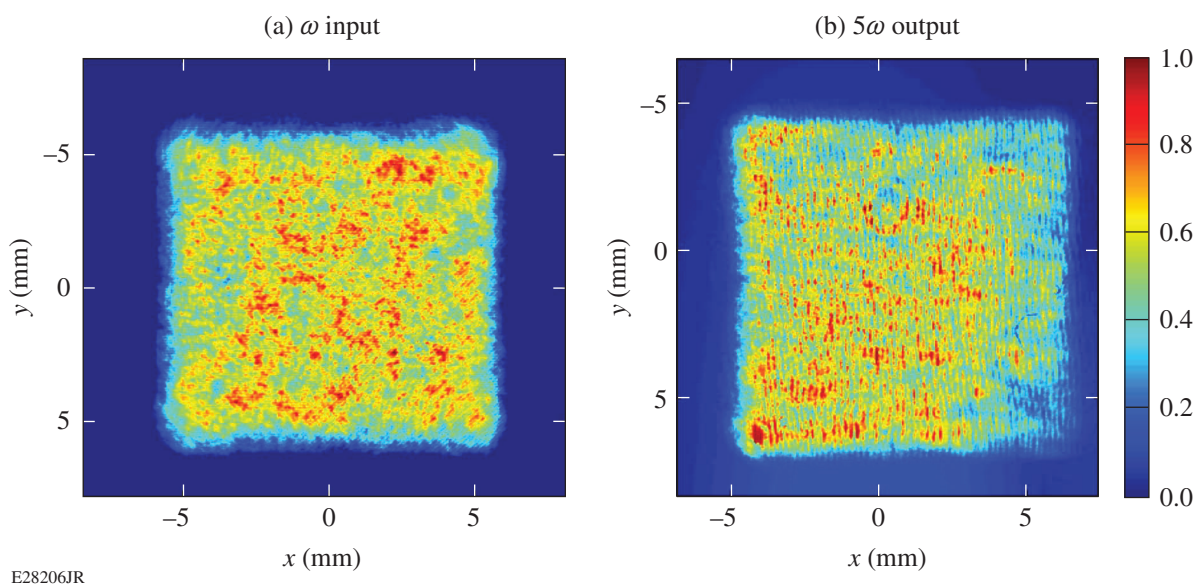
(a) ω input (b) 5ω output

E28206JR

Figure 3
Input beam image (a) at the fundamental frequency on the front of the cascade of crystals and fifth-harmonic output beam image (b) after the cryostat.

Because the ADP crystal is isolated in a helium atmosphere with very low direct conductivity to the chamber, even a small amount of energy absorption from the interaction laser beams cannot be rapidly dissipated. As a result, the ADP and other crystals in a gas cryostat work well in a single-shot regime (about one shot per minute) but cannot work at a high repetition rate because of phase mismatch caused by laser heating. Figure 4 shows the sequence of fifth-harmonic output beam images behind the cryostat taken after a various number of shots running at a 5-Hz repetition rate. Even a small amount of absorbed laser energy inside a crystal after the first shot makes the crystal warmer in the center and disturbs the temperature distribution, resulting in a spatially varying phase mismatch that grows as a series of radial rings. The 5ω beam almost disappears after 24 shots. This effect is negligible provided there is sufficient time for the crystal to thermalize. A one-minute interval between shots is enough to maintain the required temperature distribution of 0.1 K over the crystal aperture.

The angular acceptance of 5HG at a given temperature of the ADP crystal was measured as 8 mrad external (FWHM). After careful optimization, the 5HG efficiency became as high as 26% at a 0.1-Hz repetition rate with a 2.4-ns pulse and an input intensity of 0.3 GW/cm^2. This efficiency describes the portion of the input 1ω energy that has been transformed into the fifth harmonic and is available at the output of the cascade of crystals for use in any application, and includes linear and nonlinear loss mechanisms.

The energy balance is the ratio of the total energy of all beams after the cryostat to the 1ω energy at the input of the first crystal of the cascade. Therefore, it represents a fraction of energy transmitted from input to output through all three crystals and the cryostat. The initial balance is just 62% at very low input beam intensity and corresponds to passive losses, mostly coming from linear absorption and Fresnel reflections. It also demonstrates that the total conversion efficiency of 5HG could be increased by, for example, better AR coatings and crystalline windows. At high input beam intensity the total energy transmitted through the system and the energy balance drop due to significant nonlinear losses, which dramatically limits 5ω conversion efficiency. The energy balance at peak 5HG efficiency was 48%, with the additional losses coming mainly from two-photon absorption (TPA). We measured TPA at 211 nm in air (13.5 m) and in the longer (15-mm) ADP crystal cut at the x plane using the 5ω beam from the above-described setup. The TPA coefficient of ADP at 211 nm was measured as (1.2±0.2) cm/GW. Due to a relatively small dynamic range of the input energy, that measurement is not very accurate. The difference in TPA's of ADP along different crystal axes is within the error of the measurement. We also measured TPA in the air (0.0008±0.0002 cm/GW) and in fused silica (0.5±0.1 cm/GW) at 211 nm and in ADP at 263 nm (0.25±0.1 cm/GW).
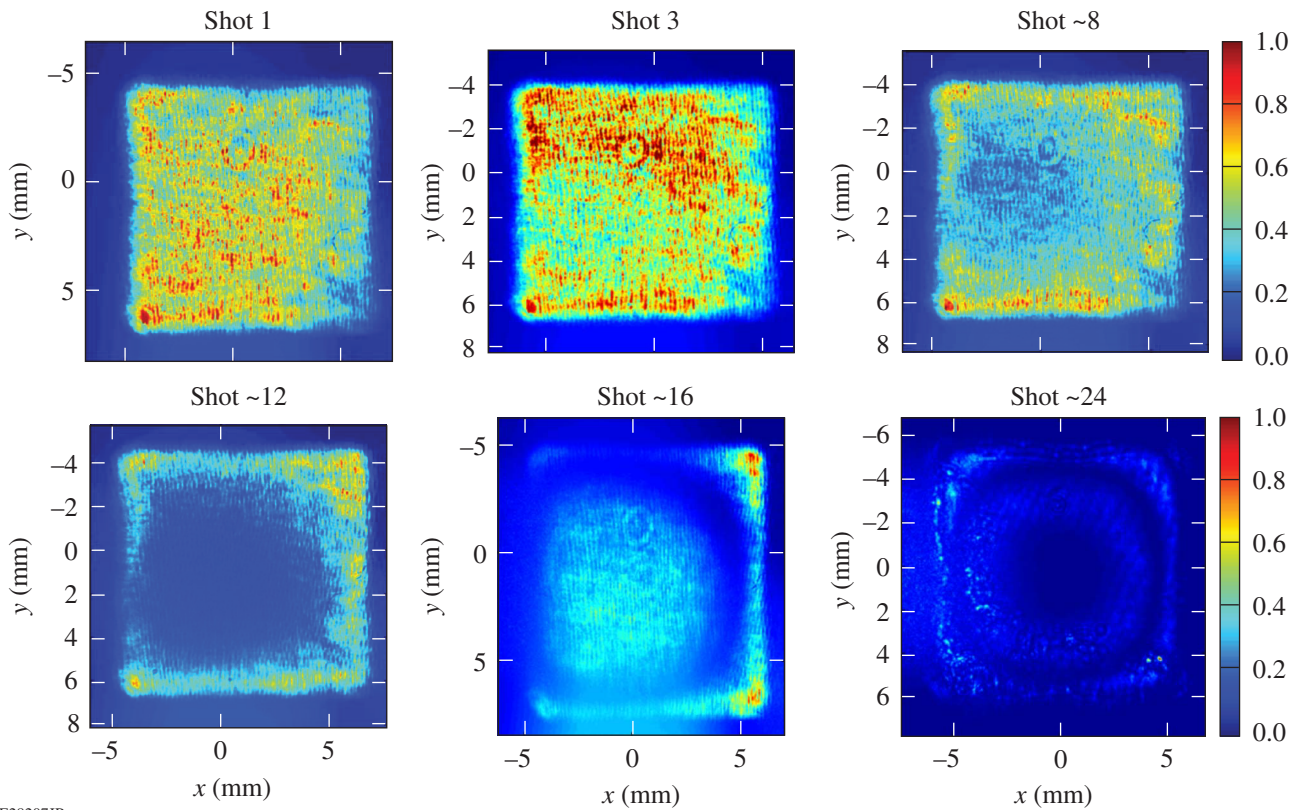
Figure 4
Fifth-harmonic output beam images after the cryostat taken after a various number of shots running at a 5-Hz repetition rate.

1. I. A. Begishev *et al.*, Opt. Lett. **43**, 2462 (2018).

2. X. Yuan *et al.*, J. Cryst. Growth **293**, 97 (2006).

3. I. A. Begishev *et al.*, J. Appl. Spectrosc. **51**, 1218 (1989).

4. V. Bagnoud *et al.*, Appl. Opt. **44**, 282 (2005).

Dynamics of Electronic Excitations Involved in Laser-Induced Damage in HfO_2 and SiO_2 Films

K. R. P. Kafka, B. N. Hoffman, A. A. Kozlov, and S. G. Demos

Laboratory for Laser Energetics, University of Rochester

Progress toward the development of thin-film–based optical components to meet the increasing demand for higher peak or average-power short-pulse laser systems requires improvements in their resistance to laser-induced damage. Understanding the dynamics of electron excitations associated with the initiation of laser-induced damage and the role of defects is of fundamental interest. The presence of native defects in a thin film is largely dependent on the manufacturing process.[1] Recent work has demonstrated that different defect species are responsible for damage initiation depending on the laser pulse length.[2] This suggests that the excitation and relaxation parameters of the precursor defects are directly expressed by the fluence where these defects can initiate damage for a given set of laser parameters. Pump–probe time-resolved experiments are a standard method being used to study the dynamics of electronic excitations. Such damage-testing experiments previously performed have provided important information (such as the relaxation time of the conduction band electrons and the presence of a delayed return to pre-exposure conditions).[3]

The present work aims to reveal information on the dynamics of the electronic excitation at the onset of damage initiation in plasma ion–assisted deposition silica and hafnia monolayers. The experiments employ a pump–probe damage-testing configuration using 1053-nm, 0.6-ps laser pulses. Special attention was given to the determination of damage-initiation conditions, which are defined by any observable material modification using differential-interference contrast (DIC) microscopy. In each set of data, the pump pulse intensity/fluence is kept constant and below that of the single-pulse laser-induced–damage threshold ($LIDT_1$), while the temporally delayed probe pulse fluence is independently adjusted to the onset of damage initiation. By analyzing the probe beam's damage threshold ($LIDT_{probe}$) as a function of delay, combined with detailed study of the resulting morphology, we aim to characterize the relaxation dynamics of defects that are involved in the damage process.

The measured $LIDT_{probe}$ values (markers) are shown in Fig. 1 for both hafnia and silica samples for the indicated pump fluence levels. The $LIDT_{probe}$ values increase with increasing delay toward the respective $LIDT_1$ values (horizontal lines). This behavior provides insight into the dynamics of the relaxation of electronic excitations associated with the damage initiation process that are activated by the pump pulse. The experimental results in hafnia show that the effective relaxation time of the pump-induced excitation depends on the pump fluence. For the lowest pump fluence, the $LIDT_{probe}$ returns to the single-pulse value by a 100-ps delay, while for the highest pump fluence, the $LIDT_{probe}$ value does not fully return within the 1-ns delay range of this experiment.

The morphology of the damage sites was studied using DIC and SEM microscopies. DIC microscopy images (not shown) demonstrate that when the pump and probe fluences are held constant, the density (severity) of damage significantly decreases as the delay increases for both materials. SEM analysis reveals that all damage sites of both materials (generated at damage threshold conditions) are composed of nanoscale pits, including sites formed by a single pulse. Characteristic images are shown in Fig. 2 for the case of silica. The SEM image of damage formed by a single pulse with fluence at $LIDT_1$ [Fig. 2(a)] demonstrates a nanopit damage density $>10^8$ cm^{-2}.

The series of SEM images at different delay times shown in Fig. 2 indicates that the morphology of the silica damage sites changes with pump–probe delay time, with their size being the most-characteristic attribute of this effect. There are two general types of pits, which for simplicity we will refer to as "smaller" (having a diameter <100 nm) and "larger" (having a diameter
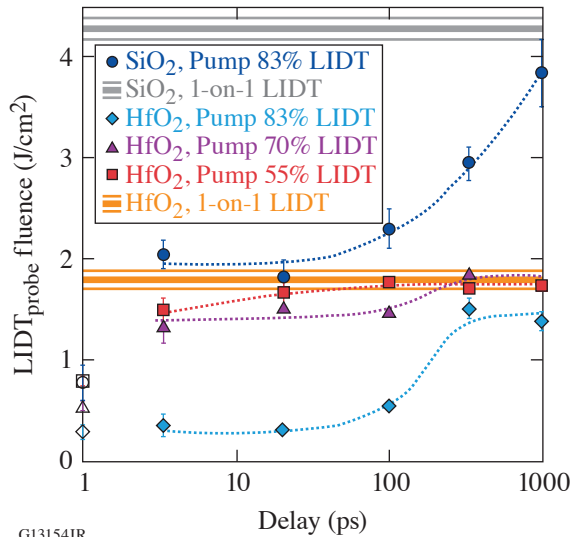
Figure 1
Double-pulse damage thresholds as a function of delay for indicated pump fluences. Horizontal lines indicate the one-pulse LIDT and uncertainty values for hafnia (orange lines) and silica (gray lines). Open markers represent the theoretical minimum value. Dotted lines are drawn to guide the eye.
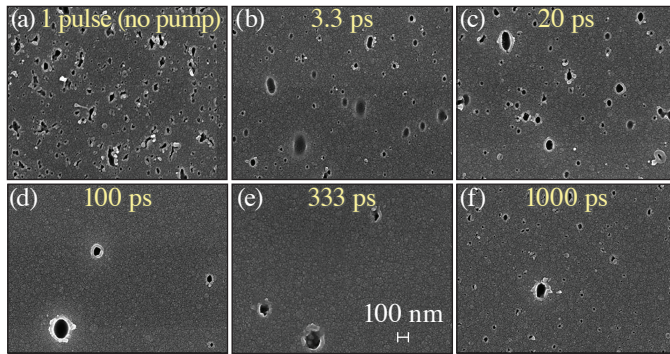
Figure 2
SEM images of damage sites on SiO_2 tested in vacuum at near-threshold fluences and indicated delay times. Fluences: (a) $\phi_{pump} = 0$, $\phi_{probe} = 4.5$ J/cm^2, [(b)–(f)] $\phi_{pump} = 83\%$ LIDT$_1$ with ϕ_{probe} values as follows: (b) 2.2 J/cm^2, (c) 2.0 J/cm^2, (d) 2.5 J/cm^2, (e) 3.2 J/cm^2, and (f) 3.8 J/cm^2.

>100 nm). Damage with a single pulse exclusively contains the smaller pits at very high damage density. These smaller pits are also observed for short delay times (3.3 ps and 20 ps) and reappear at 1000 ps, when the LIDT$_{probe}$ has returned to single-pulse damage behavior. In contrast, the larger pits were generated with much lower damage density and observed at all tested double-pulse delays (>3 ps) but not under single-pulse damage. Therefore, both types of pits were observed to coexist only at delays of 3.3 ps, 20 ps, and 1000 ps, as manifested in Fig. 2. SEM analysis of hafnia damage sites also shows the nanopit morphology but lacks any evidence suggesting a change in the damage morphologies as a function of the delay time.

Previous observations demonstrated that damage in silica/hafnia multilayer dielectric coatings is initiated by two different mechanisms as a function of the pulse duration, where the change in mechanism occurs at about 2.5 ps (Ref. 2). It was suggested that this may arise from defect populations having different properties, either physical (such as size) or stoichiometric/electronic. Following this line of reasoning, we postulate that the morphology behavior observed for silica in this work is due to two types of defects that have different relaxation times. This hypothesis requires further investigation that is outside the scope of this work.

Finally, it must be noted that the SEM images clearly show that damage initiates at distinct locations, even though some adjacent pits do merge together. Due to this high areal density of nanopits at damage initiation conditions with a single pulse, of the order of 10^8 cm^{-2}, it is not surprising that damage appears to be uniform at lower magnifications for subpicosecond laser pulses, giving rise to the widely adopted assumption that damage is "intrinsic." This perception becomes dominant in optical components employing multilayer dielectric coatings, when damage initiates below the top layer of the multilayer coating.

In conclusion, the results indicate that the relaxation time of electronic excitations associated with laser-induced–damage initiation depends on the pump fluence and extends up to about 1 ns. Furthermore, the damage morphology near $LIDT_1$ in all cases was observed to be a collection of nanopits. The results for silica show two different types of nanopit morphologies, arguably suggesting two types of defects, that manifest on different time scales: (1) <100 ps and (2) >3 ps, while observations for hafnia were unable to distinguish multiple morphologies. Future work identifying these defect structures could potentially enable subsequent material optimization for damage performance with subpicosecond lasers.

1. M. Chorel *et al.*, Opt. Express **27**, 16,922 (2019).
2. A. A. Kozlov *et al.*, Sci. Rep. **9**, 607 (2019).
3. D. N. Nguyen *et al.*, Appl. Phys. Lett. **97**, 191909 (2010); **98**, 079902(E) (2011).

FY21 Q1 Laser Facility Report

J. Puth, M. Labuzeta, D. Canning, and R. T. Janezic

Laboratory for Laser Energetics, University of Rochester

During the first quarter of FY21, the Omega Laser Facility conducted 326 target shots on OMEGA and 210 target shots on OMEGA EP for a total of 536 target shots (see Tables I and II). OMEGA averaged 10.9 target shots per operating day, averaging 92.7% Availability and 90.8% Experimental Effectiveness. OMEGA EP averaged 8.1 target shots per operating day averaging 92.7% Availability and 92.4 Experimental Effectiveness.

Table I: OMEGA Laser System target shot summary for Q1 FY21.

Program	Laboratory	Planned Number of Target Shots	Actual Number of Target Shots
ICF	LLE	71.5	71
	LANL	11	9
	LLNL	16.5	18
ICF Subtotal		99	98
HED	LLE	22	19
	LANL	11	11
	LLNL	33	31
	SNL	11	10
HED Subtotal		77	71
LBS	LLE	22	22
	LLNL	11	12
LBS Subtotal		33	34
AIBS		33	35
ARPA-E		22	24
NLUF		44	39
Calibration	LLE	11	25
Grand Total		319	326

Table II: OMEGA EP Laser System target shot summary for Q1 FY21.

Program	Laboratory	Planned Number of Target Shots	Actual Number of Target Shots
ICF	LLE	14	16
	LLNL	7	8
	NRL	7	11
ICF Subtotal		**28**	**35**
HED	LLE	28	35
	LANL	7	6
	LLNL	21	29
	SNL	7	10
HED Subtotal		**63**	**80**
LBS	LLE	14	20
	LLNL	7	7
LBS Subtotal		**21**	**27**
AIBS		14	15
Marvel		14	24
NLUF		17.5	19
Calibration	LLE	0	10
Grand Total		**157.5**	**210**

During this period, the OMEGA target chamber's vacuum pumps were reconfigured for improved vibration isolation to achieve better target stability. This upgrade will be particularly important for campaigns where target offsets are undesirable but reduces the probability of vibrations causing target damage for all users. The newly commissioned IR optical transmission inspection system (IR OTIS) is being employed to characterize components in the beamline path. Measurements have resulted in a better understanding of the small variations in polarization at the beamline splits and are helping operations determine strategies to mitigate. In the future, this diagnostic will be used regularly to identify damage issues for maintenance on the OMEGA Beamline System.

Project RemotePI: COVID-19 Mitigation-Compliant Operations on OMEGA and OMEGA EP

G. Pien, S. F. B. Morse, B. E. Kruschwitz, and T. J. Kessler

Laboratory for Laser Energetics, University of Rochester

The COVID-19 pandemic presented an unprecedented challenge to our highly productive experimental facility. While the Omega Laser Facility was in standby mode for "NY State on PAUSE," our operations team evaluated and modified the Omega operating processes to deliver "normal" operational throughput with most scientists and some support staff working remotely. Since the Omega user base is located around the globe, the experiment-planning process was already conducted largely via online, e-mail, and video conferencing methods; therefore, little change to that was necessary. However, shot-day operations required extensive changes. Shot-day transactions between the Principal Investigators (PI's) and the operations crew had been done in person only, requiring the PI's to be on-site. New travel restrictions meant this was seldom possible. Additionally, new occupancy restrictions to support social distancing limited the number of personnel on-site.

To address these new constraints, the remotePI protocol was implemented. The primary objective was to facilitate PI-to-Operations shot-day transactions while complying with COVID-19 mitigation rules (social distancing and travel limitations) by implementing a minimal set of changes to our existing processes—changes that were implementable on a very short development cycle, easy to learn, and used only existing and available equipment, particularly for the off-site participants. We achieved these goals while supporting efficient operations—meeting or exceeding "usual" Omega levels of effectiveness, availability, and flexibility.

Each OMEGA 60 or OMEGA EP shot cycle is governed by a series of transactions between the PI and the facility. The remotePI system eliminates PI location dependence by creating a virtual venue for these transactions using an intuitive platform and commonly available equipment. The centerpiece of remotePI is an all-day Zoom meeting for each facility, which we dubbed "ShotStream." ShotStream connects the PI to the facility, as well as to collaborators and technical staff. Each day there is one ShotStream opened for each facility, comprising two virtual rooms: one "main room" used as a collaboration space for PI's and another area (the "control room") used exclusively for communication between the PI and the operations crew (see Fig. 1). A simple rule set is implemented to allow concise communication between the PI and Operations crew.

ShotStream provides a venue for all the shot-day transactions between the PI and the facility (see Fig. 2). The audio channel from one of the ShotStream rooms is connected directly to a facility intercom channel, allowing the PI to communicate directly with any of the on-site staff. Screen sharing and video feeds allow the PI to receive important information such as target images, pulse-shape predictions, and shot configuration database changes. Also available on the Zoom are direct video from key diagnostics, such as VISAR/ASBO (velocity interferometer system for any reflector/active shock breakout) cameras, and real-time video of any piece of equipment can also be piped into ShotStream. Final approvals prior to the shot are conducted on ShotStream. Additionally, the PI conducts the pre-watch briefings to the Operations crew on ShotStream. The PI observes Control Room operations during the shot on ShotStream and can participate whenever appropriate. Regardless of their actual location in the world, ShotStream puts the PI into our Control Rooms during the shot. Data from each shot are posted online for the PI to review. Electronic data [e.g., charge-coupled device, image plate, or oscilloscope readouts] have been traditionally available online, but
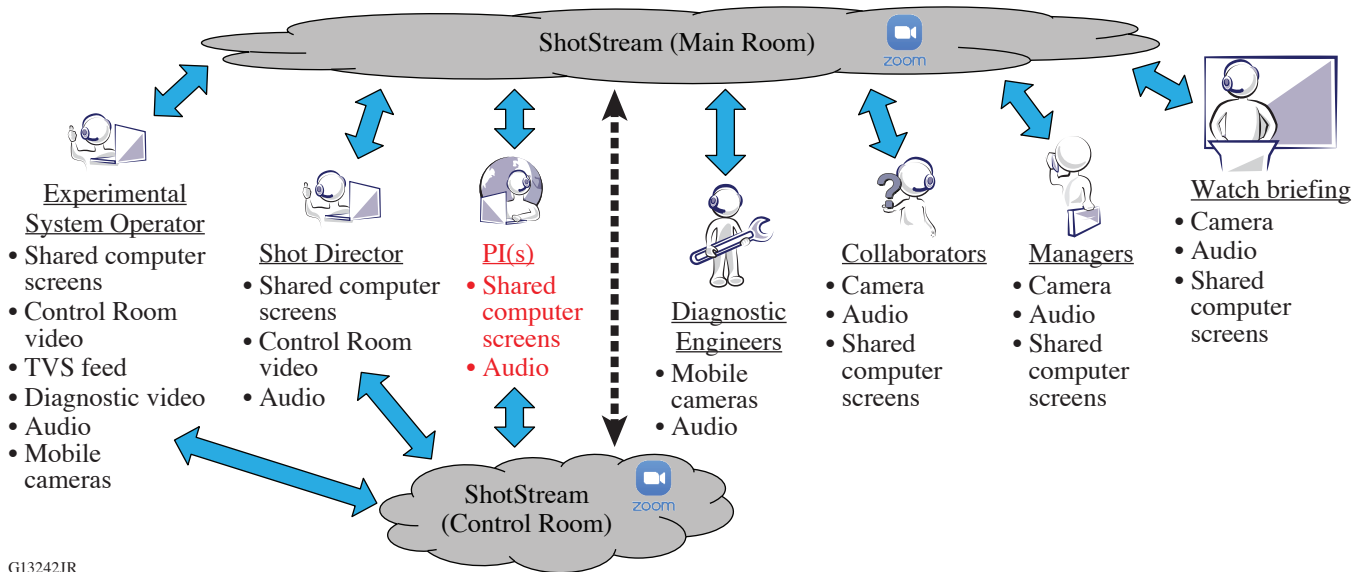
Figure 1

ShotStream virtual facility conceptual layout. The virtual main room is used by all participants as a collaboration area, for crew briefings, etc. The virtual control room is used for direct communication between the PI and shot crew.
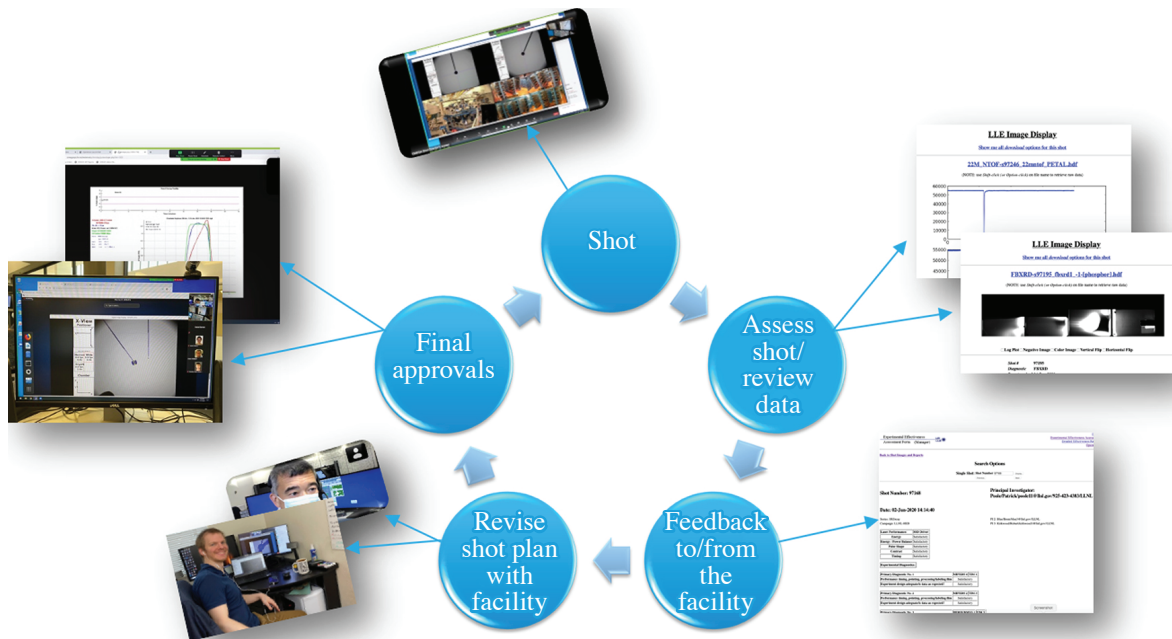
Figure 2

All of the shot-day transactions between the PI and the facility are supported by the remotePI process.

film data usually had been handled in person. Film data are now scanned and posted to the LLE website shortly after each shot. The post-shot feedback paper forms have been replaced with similar online forms for quick and precise feedback to the facility.

Additionally, mobile cameras can be deployed to the field and broadcast on ShotStream to allow on-demand video/audio communications between remote participants (PI's or technical staff) and on-site operators. This supports precise instrument setup and troubleshooting even when the system experts are not on-site.

Today, PI's as well as many support staff and managers use the remotePI system to participate in shot operations on OMEGA 60 and OMEGA EP on a daily basis while complying with the strict social distancing requirements that are essential to COVID-19 mitigation. While the modifications to the system to implement remotePI are modest in scope and now operate with little overhead cost, the software and hardware updates needed to initially deploy the system required participation by many of our support staff, most of whom were working remotely themselves. Key to the success of remotePI, only commonly available equipment (a PC or mobile device with an internet connection) is needed for a PI to fully participate in shot operations. A typical ShotStream user view is shown in Fig. 3.
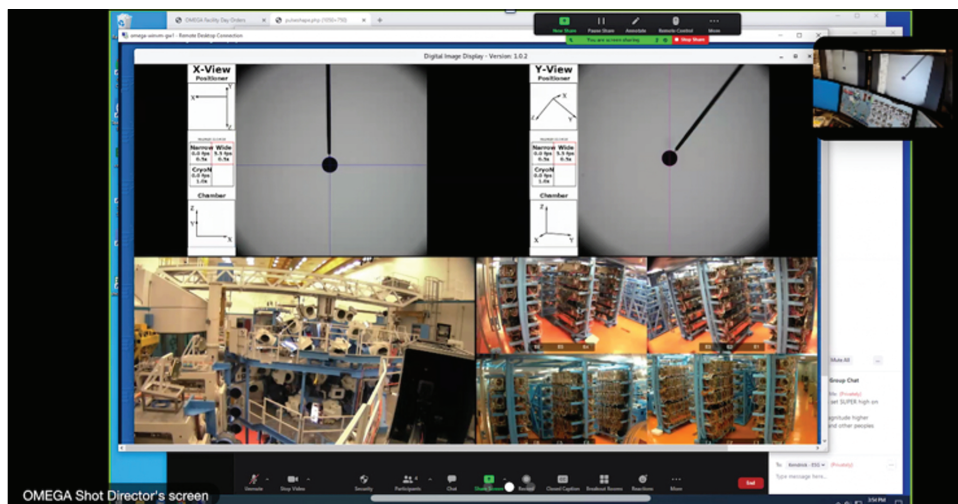
G13270JR

Figure 3
Typical ShotStream view shown on a mobile device.

Since resumption of shot operations in June 2020, all OMEGA 60 and OMEGA EP shots have used the remotePI system. Changing to the remotePI protocol does not appear to have adversely affected the availability or effectiveness of our facility. During our first seven months of operations, the effectiveness and availability results on both OMEGA 60 and OMEGA EP are comparable to those of the seven months leading up to the pandemic. After-action reports from PI's have been largely complimentary. Comparison of performance in legacy operations mode (9/1/19–3/22/20) and remote PI operations mode (6/3/20–12/14/20) are shown in Tables I and II. Because of the numerous benefits brought to the facility by remotePI and demonstrated over the past year, including enhanced scheduling flexibility and more efficient use of support resources, LLE plans to continue to make remotePI available in our operational toolkit even after the constraints of the Covid-19 pandemic are lifted.

Table I: Comparison of OMEGA 60 performance pre-/post-COVID-19.

Date Range	Number of Shots	Average Availability	Average Effectiveness
9/1/19 to 3/22/20	648	93.9%	94.9%
6/3/20 to 12/14/20	658	91.1%	94.5%

Table II: Comparison of OMEGA EP performance pre-/post-COVID-19.

Date Range	Number of Shots	Average Availability	Average Effectiveness
9/1/19 to 3/22/20	503	96.7%	95.7%
6/3/20 to 12/14/20	516	93.9%	95.4%

Publications and Conference Presentations

Publications

K. S. Anderson, C. J. Forrest, O. M. Mannion, F. J. Marshall, R. C. Shah, D. T. Michel, J. A. Marozas, P. B. Radha, D. Edgell, R. Epstein, V. N. Goncharov, J. P. Knauer, M. Gatu Johnson, and S. Laffite, "Effect of Cross-Beam Energy Transfer on Target-Offset Asymmetry in Direct-Drive Inertial Confinement Fusion Implosions," Phys. Plasmas **27**, 112713 (2020).

D. H. Barnak, M. J. Bonino, P.-Y. Chang, J. R. Davies, E. C. Hansen, D. R. Harding, J. L. Peebles, and R. Betti, "Characterizing Laser Preheat for Laser-Driven Magnetized Liner Inertial Fusion Using Soft X-Ray Emission," Phys. Plasmas **27**, 112709 (2020).

E. M. Campbell, T. C. Sangster, V. N. Goncharov, J. D. Zuegel, S. F. B. Morse, C. Sorce, G. W. Collins, M. S. Wei, R. Betti, S. P. Regan, D. H. Froula, C. Dorrer, D. R. Harding, V. Gopalaswamy, J. P. Knauer, R. Shah, O. M. Mannion, J. A. Marozas, P. B. Radha, M. J. Rosenberg, T. J. B. Collins, A. R. Christopherson, A. A. Solodov, D. Cao, J. P. Palastro, R. K. Follett, and M. Farrell, "Direct-Drive Laser Fusion: Status, Plans and Future," Phil. Trans. R. Soc. A **379**, 2020011 (2020).

L. E. Crandall, J. R. Rygg, D. K. Spaulding, T. R. Boehly, S. Brygoo, P. M. Celliers, J. H. Eggert, D. E. Fratanduono, B. J. Henderson, M. F. Huff, R. Jeanloz, A. Lazicki, M. C. Marshall, D. N. Polsin, M. Zaghoo, M. Millot, and G. W. Collins, "Equation of State of CO_2 Shock Compressed to 1 TPa," Phys. Rev. Lett. **125**, 165701 (2020).

R. Epstein, R. C. Mancini, D. T. Cliche, R. C. Shah, T. J. B. Collins, C. Stoeckl, P. W. McKenty, P. B. Radha, S. P. Regan, and V. N. Goncharov, "Self-Radiography of Imploded Shells on OMEGA Based on Additive-Free Multi-Monochromatic Continuum Spectral Analysis," Phys. Plasmas **27**, 122709 (2020).

F. García-Rubio, R. Betti, J. Sanz, and H. Aluie, "Self-Consistent Theory of the Darrieus–Landau and Rayleigh–Taylor Instabilities with Self-Generated Magnetic Fields," Phys. Plasmas **27**, 112715 (2020).

P. E. Grabowski, S. B. Hansen, M. S. Murillo, L. G. Stanton, F. R. Graziani, A. B. Zylstra, S. D. Baalrud, P. Arnault, A. D. Baczewski, L. X. Benedict, C. Blancard, O. Čertik, J. Clérouin, L. A. Collins, S. Copeland, A. A. Correa, J. Dai, J. Daligault, M. P. Desjarlais, M. W. C. Dharma-wardana, G. Faussurier, J. Haack, T. Haxhimali, A. Hayes-Sterbenz, Y. Hou, S. X. Hu, D. Jensen, G. Jungman, G. Kagan, D. Kang, J. D. Kress, Q. Ma, M. Marciante, E. Meyer, R. E. Rudd, D. Saumon, L. Shulenburger, R. L. Singleton Jr., T. Sjostrom, L. J. Stanek, C. E. Starrett, C. Ticknor, S. Valaitis, J. Venzke, and A. White, "Review of the First Charged-Particle Transport Coefficient Comparison Workshop," High Energy Density Phys. **37**, 100905 (2020).

B. M. Haines, R. C. Shah, J. M. Smidt, B. J. Albright, T. Cardenas, M. R. Douglas, C. Forrest, V. Yu. Glebov, M. A. Gunderson, C. Hamilton, K. Henderson, Y. Kim, M. N. Lee, T. J. Murphy, J. A. Oertel, R. E. Olson, B. M. Patterson, R. B. Randolph, and D. Schmidt, "The Rate of Development of Atomic Mixing and Temperature Equilibration in Inertial Confinement Fusion Implosions," Phys. Plasmas **27**, 102701 (2020).

D. R. Harding, M. D. Wittman, N. P. Redden, D. H. Edgell, and J. Ulreich, "Comparison of Shadowgraphy and X-Ray Phase-Contrast Methods for Characterizing a DT Ice Layer in an Inertial Confinement Fusion Target," Fusion Sci. Technol. **76**, 814 (2020).

A. J. Harvey-Thompson, M. R. Weis, D. E. Ruiz, M. S. Wei, A. B. Sefkow, T. Nagayama, E. M. Campbell, J. A. Fooks, M. E. Glinsky, and K. J. Peterson, "The Effect of Laser Entrance Hold Foil Thickness on MagLIF-Relevant Laser Preheat," Phys. Plasmas **27**, 113301 (2020).

G. W. Jenkins, C. Feng, and J. Bromage, "Overcoming Gas Ionization Limitations with Divided-Pulse Nonlinear Compression," Opt. Express **28**, 31,943 (2020).

D. Kawahito, M. Bailly-Grandvaux, M. Dozieres, C. McGuffey, P. Forestier-Colleoni, J. Peebles, J. J. Honrubia, B. Khiar,

S. Hansen, P. Tzeferacos, M. S. Wei, C. M. Krauland, P. Gourdain, J. R. Davies, K. Matsuo, S. Fujioka, E. M. Campbell, J. J. Santos, D. Batani, K. Bhutwala, S. Zhang, and F. N. Beg, "Fast Electron Transport Dynamics and Energy Deposition in Magnetized, Imploded Cylindrical Plasma," Phil. Trans. R. Soc. A **379**, 20200052 (2020).

J. Kim, A. Link, D. Canning, P. Fitzsimmons, J. A. Fooks, S. Kerr, T. Ma, M. J. E. Manuel, D. Mariscal, R. Wallace, G. J. Williams, L. Willingale, F. N. Beg, and H. Chen, "Dynamic Focusing of Laser Driven Positron Jets by Self-Generated Fields," New J. Phys. **22**, 123020 (2020).

T. Z. Kosc, H. Huang, T. J. Kessler, R. A. Negres, and S. G. Demos, "Determination of the Raman Polarizability Tensor in the Optically Anisotropic Crystal Potassium Dihydrogen Phosphate and Its Deuterated Analog," Sci. Rep. **10**, 16283 (2020).

R. H. Lehmberg, M. F. Wolford, J. L. Weaver, D. Kehne, S. P. Obenschain, D. Eimerl, and J. P. Palastro, "Stimulated Rotational Raman Scattering of Arbitrarily Polarized Broadband Light," Phys. Rev. A **102**, 063530 (2020).

C. A. McCoy, S. X. Hu, M. C. Marshall, D. N. Polsin, D. E. Fratanduono, Y. H. Ding, P. M. Celliers, T. R. Boehly, and D. D. Meyerhofer, "Measurement of the Sound Velocity and Grüneisen Parameter of Polystyrene at Inertial Confinement Fusion Conditions," Phys. Rev. B **102**, 184102 (2020).

B. Militzer, F. González-Cataldo, S. Zhang, H. D. Whitley, D. C. Swift, and M. Millot, "Nonideal Mixing Effects in Warm Dense Matter Studied with First-Principles Computer Simulations," J. Chem. Phys. **153**, 184101 (2020).

Z. L. Mohamed, O. M. Mannion, E. P. Hartouni, J. P. Knauer, and C. J. Forrest, "A Generalized Forward Fit for Neutron Detectors with Energy-Dependent Response Functions," J. Appl. Phys. **128**, 214501 (2020).

J. Nilsen, D. Åberg, H. D. Whitley, B. G. Wilson, L. H. Yang, P. A. Sterne, M. W. Daene, M. E. Martin, S. Zhang, and W. R. Johnson, "Role of Opacity at the 9 keV Back Lighter Energy Used in Measuring the Equation of State of Boron at Pressures up to a Gbar," High Energy Density Phys. **37**, 100880 (2020).

G. Pien, B. E. Kruschwitz, S. F. B. Morse, and T. J. Kessler, "Experimental Operations at the Omega Laser Facility Amid COVID-19," ICUIL News **11**, 10 (2020).

D. Ramsey, P. Franke, T. T. Simpson, D. H. Froula, and J. P. Palastro, "Vacuum Acceleration of Electrons in a Dynamic Laser Pulse," Phys. Rev. E **102**, 043207 (2020).

J. J. Ruby, J. R. Rygg, D. A. Chin, J. A. Gaffney, P. J. Adrian, D. Bishel, C. J. Forrest, V. Yu. Glebov, N. V. Kabadi, P. M. Nilson, Y. Ping, C. Stoeckl, and G. W. Collins, "Constraining Physical Models at Gigabar Pressures," Phys. Rev. E **102**, 053210 (2020).

J. J. Ruby, J. R. Rygg, D. A. Chin, J. A. Gaffney, P. J. Adrian, C. J. Forrest, V. Yu. Glebov, N. V. Kabadi, P. M. Nilson, Y. Ping, C. Stoeckl, and G. W. Collins, "Energy Flow in Thin Shell Implosions and Explosions," Phys. Rev. Lett. **125**, 215001 (2020).

B. Scheiner, M. J. Schmitt, D. Schmidt, L. Goodwin, and F. J. Marshall, "Two-Photon Polymerization Printed Lattices as Support Structures in Multi-Shell ICF Targets: Platform Development and Initial Assessment," Phys. Plasmas **27**, 122702 (2020).

T. T. Simpson, D. Ramsey, P Franke, N. Vafaei-Najafabadi, D. Turnbull, D. H. Froula, and J. P. Palastro, "Nonlinear Spatiotemporal Control of Laser Intensity," Opt. Lett. **28**, 38,516 (2020).

C. A. Thomas, E. M. Campbell, K. L. Baker, D. T. Casey, M. Hohenberger, A. L. Kritcher, B. K. Spears, S. F. Khan, R. Nora, D. T. Woods, J. L. Milovich, R. L. Berger, D. Strozzi, D. D. Ho, D. Clark, B. Bachmann, L. R. Benedetti, R. Bionta, P. M. Celliers, D. N. Fittinghoff, G. Grim, R. Hatarik, N. Izumi, G. Kyrala, T. Ma, M. Millot, S. R. Nagel, P. K. Patel, C. Yeamans, A. Nikroo, M. Tabak, M. Gatu Johnson, P. L. Volegov, and S. M. Finnegan, "Deficiencies in Compression and Yield in X-Ray Driven Implosions," Phys. Plasmas **27**, 112705 (2020).

C. A. Thomas, E. M. Campbell, K. L. Baker, D. T. Casey, M. Hohenberger, A. L. Kritcher, B. K. Spears, S. F. Khan, R. Nora, D. T. Woods, J. L. Milovich, R. L. Berger, D. Strozzi, D. D. Ho, D. Clark, B. Bachmann, L. R. Benedetti, R. Bionta, P. M. Celliers, D. N. Fittinghoff, G. Grim, R. Hatarik, N. Izumi, G. Kyrala, T. Ma, M. Millot, S. R. Nagel, P. K. Patel, C. Yeamans, A. Nikroo, M. Tabak, M. Gatu Johnson, P. Volegov, and S. M. Finnegan, "Experiments to Explore the Influence of Pulse Shaping at the National Ignition Facility," Phys. Plasmas **27**, 112708 (2020).

C. A. Thomas, E. M. Campbell, K. L. Baker, D. T. Casey, M. Hohenberger, A. L. Kritcher, B. K. Spears, S. F. Khan, R. Nora, D. T. Woods, J. L. Milovich, R. L. Berger, D. Strozzi, D. D. Ho, D. Clark, B. Bachmann, L. R. Benedetti, R. Bionta, P. M. Celliers, D. N. Fittinghoff, G. Grim, R. Hatarik, N. Izumi, G. Kyrala, T. Ma, M. Millot, S. R. Nagel, P. K. Patel, C. Yeamans, A. Nikroo, M. Tabak, M. Gatu Johnson, P. L. Volegov, and S. M. Finnegan, "Principal Factors in Performance of Indirect-Drive Laser Fusion Experiments," Phys. Plasmas **27**, 112712 (2020)

D. Turnbull, A. V. Maximov, D. Cao, A. R. Christopherson, D. H. Edgell, R. K. Follett, V. Gopalaswamy, J. P. Knauer, J. P. Palastro, A. Shvydky, C. Stoeckl, H. Wen, and D. H. Froula, "Impact of Spatiotemporal Smoothing on the Two-Plasmon–Decay Instability," Phys. Plasmas **27**, 102710 (2020).

H. Zhang, R. Betti, R. Yan, and H. Aluie, "Nonlinear Bubble Competition of the Multimode Ablative Rayleigh–Taylor Instability and Its Applications to Inertial Confinement Fusion," Phys. Plasmas **27**, 122701 (2020).

S. Zhang, M. C. Marshall, L. H. Yang, P. A. Sterne, B. Militzer, M. Däne, J. A. Gaffney, A. Shamp, T. Ogitsu, K. Caspersen, A. E. Lazicki, D. Erskine, R. A. London, P. M. Celliers, J. Nilsen, and H. D. Whitley, "Benchmarking Boron Carbide Equation of State Using Computation and Experiment," Phys. Rev. E **102**, 053203 (2020).

S. Zhang and M. A. Morales, "First-Principles Equations of State and Structures of Liquid Metals in Multi-Megabar Conditions," AIP Conf. Proc. **2272**, 090004 (2020).

S. Zhang, H. D. Whitley, and T. Ogitsu, "Phase Transformation in Boron Under Shock Compression," Solid State Sci. **108**, 106376 (2020).

A. B. Zylstra, C. Yeamans, S. Le Pape, A. MacKinnon, M. Hohenberger, D. N. Fittinghoff, H. Herrmann, Y. Kim, P. B. Radha, P. W. McKenty, R. S. Craxton, and M. Hoppe, "Enhanced Direct-Drive Implosion Performance on NIF with Wavelength Separation," Phys. Plasmas **27**, 124501 (2020).

Forthcoming Publications

I. A. Begishev, G. Brent, S. Carey, R. Chapman, I. A. Kulagin, M. H. Romanofsky, M. J. Shoup III, J. D. Zuegel, and J. Bromage, "High-Efficiency, Fifth-Harmonic-Generation of a Joule-Level Neodymium Laser in a Large-Aperture Ammonium Dihydrogen Phosphate Crystal," to be published in Optics Express.

F. Coppari, R. F. Smith, J. Wang, M. Millot, D. Kim, J. R. Rygg, S. Hamel, J. H. Eggert, and T. S. Duffy, "Implications of the Iron Oxide Phase Transition on the Interiors of Rocky Exoplanets," to be published in Nature Geoscience.

J. R. Davies, H. Wen, J.-Y. Ji, and E. D. Held, "Transport Coefficients for Magnetic-Field Evolution in Inviscid Magnetohydrodynamics," to be published in Physics of Plasmas.

F. García-Rubio, R. Betti, J. Sanz, and H. Aluie, "Magnetic-Field Generation and Effect on Ablative Rayleigh–Taylor Instability in Diffusive Ablation Fronts," to be published in Physics of Plasmas.

V. Yu. Glebov, C. Stoeckl, C. J. Forrest, J. P. Knauer, O. M. Mannion, M. H. Romanofsky, T. C. Sangster, and S. P. Regan,

"A Novel Photomultiplier Tube Neutron Time-of-Flight Detector," to be published in Review of Scientific Instruments.

K. R. P. Kafka, B. N. Hoffman, H. Huang, and S. G. Demos, "Mechanisms of Picosecond Laser-Induced Damage from Interaction with Model Contamination Particles on a High Reflector," to be published in Optical Engineering.

Y. Kim, H. W. Herrmann, N. M. Hoffman, M. J. Schmitt, G. Kagan, A. M. McEvoy, A. B. Zylstra, J. M. Smidt, S. Gales, A. Leatherland, M. Rubery, M. Gatu Johnson, J. A. Frenje, V. Yu. Glebov, and C. Forrest, "First Observation of Increased DT Yield over Prediction due to Addition of Hydrogen," to be published in Physics of Plasmas.

P. Koester, F. Baffigi, G. Cristoforetti, L. Labate, L. A. Gizzi, S. Baton, M. Koenig, A. Colaïtis, D. Batani, A. Casner, D. Raffestin, A. Tentori, J. Trela, C. Rousseaux, G. Boutoux, S. Brygoo, L. Jacquet, C. Reverdin, E. Le Bel, L. LeDeroff, W. Theobald, and K. Shigemori, "Bremsstrahlung Cannon Design for Shock Ignition Relevant Regime," to be published in Review of Scientific Instruments.

A. A. Kozlov, S. G. Demos, D. Canning, B. N. Hoffman, B. E. Kruschwitz, A. L. Rigatti, N. Savidis, and L. J. Waxer, "Long-Term Monitoring the Damage Performance of Multilayer Dielectric Grating Samples Residing Inside the Compressor Chamber of the OMEGA EP Laser," to be published in Optical Engineering.

L. Lamaignère, A. Ollé, M. Chorel, N. Roquin, A. A. Kozlov, B. N. Hoffman, J. B. Oliver, S. G. Demos, L. Gallais, R. A. Negres, and A. Melninkaitis, "Round-Robin Measurements of the Laser-Induced Damage Threshold with Sub-Picosecond Pulses on Optical Single Layers," to be published in Optical Engineering.

A. Lazicki, D. McGonegle, J. R. Rygg, D. G. Braun, D. C. Swift, M. G. Gorman, R. F. Smith, P. G. Heighway, A. Higginbotham, M. J. Suggit, D. E. Fratanduono, F. Coppari, C. E. Wehrenberg, R. G. Kraus, D. Erskine, J. V. Bernier, J. M. McNaney, R. E. Rudd, G. W. Collins, J. H. Eggert, and J. S. Wark, "Metastability of Diamond Ramp-Compressed to 2 Terapascals," to be published in Nature.

B. Militzer, F. González-Cataldo, S. Zhang, K. P. Driver, and F. Soubiran, "First-Principles Equation of State Database for Warm Dense Matter Computation," to be published in Physical Review E.

J. P. Palastro, B. Malaca, J. Vieira, D. Ramsey, T. T. Simpson, P. Franke, J. L. Shaw, and D. H. Froula, "Laser-Plasma Acceleration Beyond Wave Breaking," to be published in Physical Review Letters.

R. Sobolewski, "Optical Detectors and Sensors," to be published in the Handbook of Superconducting Materials.

J. U. Wallace, K. L. Marshall, D. J. Batesky, T. Z. Kosc, B. N. Hoffman, S. Papernov, L. Garrett, J. Shojaie, and S. G. Demos, "Highly Saturated Glassy Liquid Crystal Films Having Nano- and Microscale Thicknesses for High-Power Laser Applications," to be published in ACS Applied Nanomaterials.

Conference Presentations

B. E. Ugur, "Computational Modeling and Design of Liquid Crystal Materials for Applications in the Terahertz Regime," presented at the 2020 American Institute of Chemical Engineers Eckhardt Northeast Region Conference, virtual, 3–4 October 2020.

———

S. G. Demos, K. R. P. Kafka, B. N. Hoffman, A. A. Kozlov, H. Huang, J. B. Oliver, A. L. Rigatti, T. J. Kessler, T. Z. Kosc, N. Liu, R. Dent, A. A. Shestopalov, and J. C. Lambropoulos, "The Fundamental Mechanism of Laser-Induced Damage in Optical Components for Ultrashort-Pulse Laser Systems," presented at OSA Laser Congress, virtual, 12–16 October 2020.

———

N. D. Urban, J. U. Wallace, K. L. Marshall, and S. G. Demos, "Photoswitchable Liquid Crystal Beam Shapers for High-Power Laser Applications," presented at the Clarkson University Seminar, virtual, 13 October 2020.

———

C. J. Forrest, J. P. Knauer, W. U. Schröder, V. Yu. Glebov, O. M. Mannion, K. L. Marshall, Z. L. Mohamed, P. B. Radha,

S. P. Regan, M. Romanofsky, T. C. Sangster, A. Schwemmlein, M. Sickles, C. Sorce, C. Stoeckl, and J. Szczepanski, "Nuclear Science at the University of Rochester's Omega Laser Facility," presented at Ohio University, virtual, 20 October 2020.

———

B. Webb, "Next Generation Petawatt Laser Technology," presented at the 8th Texas STEM Conference, virtual, 24 October 2020.

———

The following presentations were made at the 4th Asia-Pacific Conference on Plasma Physics, virtual, 26–31 October 2020:

R. K. Follett, J. G. Shaw, C. Dorrer, D. H. Edgell, D. H. Froula, H. Wen, J. Bromage, E. M. Hill, T. J. Kessler, A. V. Maximov, A. A. Solodov, E. M. Campbell, J. P. Palastro, J. F. Myatt, J. W. Bates, and J. L. Weaver, "Broadband Mitigation of the Multibeam Two-Plasmon Decay and Stimulated Raman Scattering Instabilities."

A. A. Solodov, M. J. Rosenberg, M. Stoeckl, A. R. Christopherson, R. Betti, W. Seka, R. Epstein, C. Stoeckl, R. K. Follett, P. B. Radha, S. P. Regan, D. H. Froula, J. P. Palastro, V. N. Goncharov,

J. F. Myatt, M. Hohenberger, B. Bachmann, and P. Michel, "Scaling and Mitigation of Hot-Electron Preheat Polar-Direct-Drive Experiments at the National Ignition Facility."

H. Wen, R. K. Follett, A. V. Maximov, D. H. Froula, J. P. Palastro, and F. S. Tsung, "Kinetic Inflation of Stimulated Raman Scattering Driven by a Broadband Frequency-Modulated Laser Pulse."

———————

O. M. Mannion, K. S. Anderson, R. Betti, E. M. Campbell, D. Cao, C. J. Forrest, V. Yu. Glebov, V. N. Goncharov, V. Gopalaswamy, I. V. Igumenshchev, S. T. Ivancic, D. W. Jacobs-Perkins, J. P. Knauer, A. Lees, F. J. Marshall, Z. L. Mohamed, D. Patel, S. P. Regan, H. G. Rinderknecht, R. C. Shah, C. Stoeckl, W. Theobald, K. M. Woo, B. D. Appelbe, J. P. Chittenden, A. J. Crilly, W. Taitano, P. Adrian, J. A. Frenje, N. V. Kabadi, and M. Gatu Johnson, "Applications of Neutron Spectroscopy in High-Energy-Density Science," presented at the High Energy Density Science Association, virtual, 8 November 2020.

———————

J. Bromage, S.-W. Bahk, I. A. Begishev, S. Bucht, C. Dorrer, C. Feng, B. N. Hoffman, C. Jeon, C. Mileham, J. B. Oliver, R. G. Roides, M. J. Shoup III, M. Spilatro, B. Webb, and J. D. Zuegel, "MTW-OPAL: A Technology Development Platform for Ultra-Intense OPCPA Systems," presented at ELI-NP Autumn School (ELIAS 2020), virtual, 9 November 2020.

———————

The following presentations were made at the 62nd Annual Meeting of the American Physical Society Division of Plasmas Physics, virtual, 9–13 November 2020:

K. S. Anderson, W. Theobald, M. J. Rosenberg, J. A. Marozas, R. H. H. Scott, and K. Glize, "Cross-Beam Energy Transfer in Simulations of NIF-Scale Strong Spherical Shock Experiments."

J. Baltazar, R. C. Shah, S. X. Hu, K. Churnetski, R. Epstein, V. N. Goncharov, I. V. Igumenshchev, T. Joshi, W. Theobald, and S. P. Regan, "Feasibility Study of Measuring In-Flight Shell Thickness for a Laser-Direct-Drive DT Cryogenic Implosion."

Z. Barfield, D. H. Froula, J. P. Palastro, J. L. Peebles, D. Mastrosimone, A. M. Hansen, J. Katz, and P. Tzeferacos, "Thermal Transport in Low-Beta Laser-Produced Plasmas."

D. H. Barnak, M. J. Bonino, J. R. Davies, E. C. Hansen, D. R. Harding, L. S. Leal, J. L. Peebles, P.-Y. Chang, R. Betti, J. D. Moody, and B. B. Pollock, "Achieving an Azimuthal Uniform Cylindrical Implosion on OMEGA."

R. Betti, V. Gopalaswamy, J. P. Knauer, A. Lees, D. Patel, C. A. Thomas, and W. Theobald, "Exploring Pathways to Hydro-Equivalent Ignition on the OMEGA Laser."

D. T. Bishel, E. V. Marley, M. B. Schneider, D. A. Liedahl, R. F. Heeter, M. E. Foord, G. E. Kemp, Y. Frank, J. A. Emig, G. Perez-Callejo, J. R. Rygg, G. W. Collins, and P. M. Nilson, "Open L-Shell Spectroscopy of Non-Local-Thermodynamic-Equilibrium Plasmas."

G. Bruhaug, H. G. Rinderknecht, M. S. Wei, G. W. Collins, J. R. Rygg, Y. E. K. Garriga, and X. C. Zhang, "High-Power THz Sources for High-Energy-Density–Physics Applications."

D. Cao, R. C. Shah, R. Epstein, A. R. Christopherson, V. Gopalaswamy, S. P. Regan, W. Theobald, and V. N. Goncharov, "Analysis of Techniques to Infer Hot-Spot Mixing Using Absolute X-Ray Emission for OMEGA Direct-Drive Layered Implosions."

L. Ceurvorst, R. Betti, A. Bose, S. X. Hu, E. M. Campbell, S. P. Regan, J. L. Peebles, W. Theobald, A. Casner, C. A. McCoy, M. Karasik, and M. Tabak, "Imprint Mitigation with Hybrid Targets."

D. A. Chin, P. M. Nilson, J. J. Ruby, X. Gong, M. K. Ginnane, B. J. Henderson, L. Crandall, D. N. Polsin, T. R. Boehly, J. R. Rygg, G. W. Collins, D. Trail, A. Amouretti, M. Harmand, R. Torchio, F. Coppari, A. Coleman, and Y. Ping, "Using X-Ray Absorption Spectroscopy to Study Iron Oxides at Extreme Compressions."

K. Churnetski, W. Theobald, K. A. Woo, R. Ejaz, I. V. Igumenshchev, S. T. Ivancic, A. Kish, M. Michalko, R. C. Shah, R. Spielman, S. P. Regan, A. Raymond, P. Bell, A. Carpenter, A. McPhee, C. Trosseille, D. K. Bradley, J. D. Hares, A. K. L. Dymoke-Bradshaw, G. Rochau, L. Claus, M. Sanchez, and D. Garand "The Third Line-of-Sight Time-Gated X-Ray Imager for OMEGA DT Cryogenic Implosions."

T. J. B. Collins, M. Hohenberger, L. Divol, W. W. Hsing, J. A. Marozas, K. A. Bauer, R. S. Craxton, P. W. McKenty, P. B. Radha, S. P. Regan, M. J. Rosenberg, and E. M. Campbell, "Optimization of OMEGA Exploding-Pusher Performance Using Shaped Pulses."

L. E. Crandall, J. R. Rygg, T. R. Boehly, B. J. Henderson, M. F. Huff, D. N. Polsin, M. Zaghoo, G. W. Collins, D. K. Spaulding, S. Brygoo, P. M. Celliers, J. H. Eggert, D. E. Fratanduono, A. Lazicki, M. C. Marshall, M. Millot, and R. Jeanloz, "Equation of State and Transport of CO_2 Shock Compressed to 1 TPa" (invited).

R. S. Craxton, W. Y. Wang, and E. M. Campbell, "A New Beam Configuration to Support Both Spherical Hohlraums and Symmetric Direct Drive."

J. R. Davies, H. Wen, E. D. Held, and J.-Y. Ji, "Transport Coefficients for Magnetic-Field Evolution in Inviscid Magnetohydrodynamics."

D. H. Edgell, R. K. Follett, J. Katz, J. A. Marozas, D. Turnbull, and D. H. Froula, "Low-Mode Asymmetry due to Polarization Smoothing in OMEGA Implosions."

R. Epstein, A. Shvydky, I. E. Golovkin, and W.-F. Fong, "Non-equilibrium Thermodynamics of Plasma Under Collisional-Radiative Equilibrium."

R. K. Follett, J. G. Shaw, C. Dorrer, D. H. Edgell, D. H. Froula, H. Wen, J. Bromage, E. M. Hill, T. J. Kessler, A. V. Maximov, A. A. Solodov, E. M. Campbell, J. P. Palastro, J. F. Myatt, J. W. Bates, and J. L. Weaver, "Broadband Mitigation of the Multibeam Two-Plasmon Decay and Stimulated Raman Scattering Instabilities."

C. J. Forrest, V. Yu. Glebov, V. N. Goncharov, J. P. Knauer, O. M. Mannion, Z. L. Mohamed, P. B. Radha, S. P. Regan, R. C. Shah, C. Stoeckl, and K. M. Woo, "Evaluating the Residual Kinetic Energy in Direct-Drive Cryogenic Implosions on OMEGA."

P. Franke, J. P. Palastro, D. Ramsey, T. T. Simpson, D. Turnbull, and D. H. Froula, "Dynamically Guided Self-Photon Acceleration."

F. Garcia-Rubio, R. Betti, H. Aluie, and J. Sanz Recio, "Magnetic-Field Effect on Rayleigh-Taylor and Darrieus–Landau Instabilities."

M. K. Ginnane, D. N. Polsin, X. Gong, T. R. Boehly, J. R. Rygg, G. W. Collins, A. Lazicki, R. Kraus, J. H. Eggert, M. C. Marshall, D. E. Fratanduono, J.-P. Davis, C. A. McCoy, C. Seagle, and S. Root, "X-Ray Diffraction Measurements of Dynamically Compressed Platinum."

V. N. Goncharov, I. V. Igumenshchev, D. R. Harding, S. F. B. Morse, S. X. Hu, P. B. Radha, D. H. Froula, S. P. Regan,

T. C. Sangster, and E. M. Campbell, "Novel Hot-Spot-Ignition Designs for Inertial Confinement Fusion with Liquid Deuterium–Tritium Spheres."

V. Gopalaswamy, R. Betti, J. P. Knauer, A. Lees, D. Patel, A. R. Christopherson, K. M. Woo, D. Cao, C. A. Thomas, I. V. Igumenshchev, S. P. Regan, W. Theobald, R. C. Shah, P. B. Radha, and K. S. Anderson, "Inferring Degradation Mechanisms in OMEGA Cryogenic Implosions Through Statistical Modeling."

A. M. Hansen, K. L. Nguyen, D. Turnbull, R. K. Follett, R. Huff, J. Katz, D. Mastrosimone, A. L. Milder, J. P. Palastro, D. H. Froula, B. Albright, and L. Yin, "Cross-Beam Energy Transfer Saturation."

B. J. Henderson, T. R. Boehly, M. Zaghoo, J. R. Rygg, D. N. Polsin, X. Gong, L. Crandall, M. Huff, M. K. Ginnane, G. W. Collins, S. Ali, and P. M. Celliers, "Optical Spectroscopy Measurements of Decaying Shocks in Transparent Crystals."

J. Hinz, V. V. Karasiev, and S. X. Hu, "A Machine-Learned, Orbital-Free, Force-Correction Model: Extending the Thermo-dynamic Range of Affordable Kohn–Sham Level Accuracy."

S. X. Hu, P. M. Nilson, V. V. Karasiev, S. B. Hansen, T. Walton, and I. E. Golovkin, "Extreme Atomic Physics at 5- to 100-Gbar Pressures."

M. Huff, J. R. Rygg, G. W. Collins, T. R. Boehly, M. Zaghoo, D. N. Polsin, M. Nakajima, B. J. Henderson, L. E. Crandall, M. C. Marshall, D. E. Fratanduono, M. Millot, R. F. Smith, J. H. Eggert, P. M. Celliers, and C. A. McCoy, "Measurements of Sound Speed in Iron Shock-Compressed to ~4000 GPa."

I. V. Igumenshchev, O. M. Mannion, J. P. Knauer, R. Betti, E. M. Campbell, D. Cao, V. N. Goncharov, V. Goplaswamy, D. Patel, S. P. Regan, R. C. Shah, A. Shvydky, W. Theobald, D. S. Clark, M. M. Marinak, and B. M. Haines, "Modeling Effects of Ion Viscosity on Dynamics of OMEGA Direct-Drive Cryogenic Implosions."

V. V. Karasiev, D. I. Mihaylov, S. X. Hu, and S. B. Trickey, "Accurate Density Functional Theory Simulations Across Warm-Dense-Matter Regime: Thermal meta-GGA Exchange-Correlation and Nuclear-Quantum Effects."

J. P. Knauer, R. Betti, V. Gopalaswamy, D. Cao, D. Patel, A. Lees, A. Shvydky, M. J. Bonino, E. M. Campbell, T. J. B.

Collins, C. J. Forrest, V. Yu. Glebov, V. N. Goncharov, D. R. Harding, J. A. Marozas, F. J. Marshall, P. W. McKenty, J. L. Peebles, P. B. Radha, S. P. Regan, T. C. Sangster, C. Stoeckl, M. Gatu Johnson, J. A. Frenje, and R. D. Petrasso, "A Systematic Study of Laser Imprint for Direct Drive—From Seeds to Integrated Implosions."

L. S. Leal, A. V. Maximov, E. C. Hansen, J. R. Davies, D. H. Barnak, J. L. Peebles, A. B. Sefkow, and R. Betti, "Simulations of Laser Preheat Effects on Yield in Mini-MagLIF Implosions on OMEGA."

A. Lees, R. Betti, J. P. Knauer, V. Gopalaswamy, D. Patel, R. Epstein, J. Carroll-Nellenback, A. R. Christopherson, K. M. Woo, O. M. Mannion, Z. L. Mohamed, F. J. Marshall, C. Stoeckl, V. Yu. Glebov, S. P. Regan, R. C. Shah, D. H. Edgell, D. Cao, V. N. Goncharov, I. V. Igumenshchev, P. B. Radha, T. J. B. Collins, T. C. Sangster, E. M. Campbell, M. Gatu Johnson, R. D. Petrasso, C. K. Li, and J. A. Frenje, "Understanding the Fusion Yield and All of Its Dependencies Using Statistical Modeling of Experimental Data" (invited).

O. M. Mannion, K. S. Anderson, R. Betti, E. M. Campbell, D. Cao, C. J. Forrest, V. Yu. Glebov, V. N. Goncharov, V. Gopalaswamy, I. V. Igumenshchev, S. T. Ivancic, D. W. Jacobs-Perkins, J. P. Knauer, A. Lees, F. J. Marshall, Z. L. Mohamed, D. Patel, S. P. Regan, H. G. Rinderknecht, R. C. Shah, C. Stoeckl, W. Theobald, K. M. Woo, and M. Gatu Johnson, "Mode One Asymmetry in Laser-Direct-Drive Inertial Confinement Fusion Implosions" (invited).

O. M. Mannion, C. J. Forrest, V. Yu. Glebov, J. P. Knauer, P. W. McKenty, Z. L. Mohamed, S. P. Regan, C. Stoeckl, B. D. Appelbe, A. J. Crilly, W. Taitano, P. J. Adrian, J. A. Frenje, N. V. Kabadi, and M. Gatu Johnson, "Measurements of the DT and DD Neutron Energy Spectrum in High Temperature Fusing Plasmas."

J. A. Marozas, K. S. Anderson, R. Betti, T. R. Boehly, R. Boni, M. J. Bonino, E. M. Campbell, D. Canning, D. Cao, T. J. B. Collins, R. S. Craxton, A. K. Davis, J. A. Delettrez, W. R. Donaldson, D. H. Edgell, R. Epstein, C. J. Forrest, D. H. Froula, V. Yu. Glebov, V. N. Goncharov, D. R. Harding, S. X. Hu, H. Huang, I. V. Igumenshchev, R. T. Janezic, D. W. Jacobs-Perkins, J. Katz, R. L. Keck, J. H. Kelly, T. J. Kessler, B. E. Kruschwitz, J. P. Knauer, T. Z. Kosc, S. J. Loucks, F. J. Marshall, A. V. Maximov, P. W. McKenty, S. F. B. Morse, P. M. Nilson, J. C. Puth, P. B. Radha, S. P. Regan, H. G. Rinderknecht, M. J. Rosenberg, T. C. Sangster, R. Shah, W. T. Shmayda,

R. W. Short, A. Shvydky, M. J. Shoup III, S. Skupsky, A. A. Solodov, C. Sorce, S. Stagnitto, C. Stoeckl, W. Theobald, D. Turnbull, J. Ulreich, M. D. Wittman, V. Gopalaswamy, J. D. Zuegel, J. A. Frenje, M. Gatu Johnson, R. D. Petrasso, H. Sio, B. Lahmann, P. Bell, B. E. Blue, S. Bhandarkar, D. K. Bradley, D. A. Callahan, A. Carpenter, D. T. Casey, J. Celeste, M. Dayton, C. S. Goyon, M. Hohenberger, O. A. Hurricane, G. E. Kemp, S. Le Pape, L. Masse, P. Michel, J. D. Moody, S. R. Nagel, A. Nikroo, R. Nora, L. Pickworth, J. E. Ralph, R. P. J. Town, R. J. Wallace, Z. B. Walters, P. Wegner, H. D. Whitley, C. B. Yeamans, M. Farrell, P. Fitzsimmons, C. Gibson, A. Greenwood, L. Carlson, T. Hilsabeck, H. Huang, J. D. Kilkenny, R. W. Luo, N. Rice, M. Schoff, W. Sweet, A. Tambazidis, T. Bernat, N. Petta, J. Hund, S. P. Obenschain, J. W. Bates, M. Karasik, A. J. Schmitt, J. Weaver, J. Hares, T. Dymoke-Bradshaw, R. E. Olson, M. J. Schmitt, S. Hsu, G. Rochau, L. Claus, Q. Looker, J. Porter, G. Robertson, M. Sanchez, and W. J. Garbett, "Laser-Direct-Drive Inertial Confinement Fusion—A Pathway to Ignition" (invited).

M. C. Marshall, M. Millot, D. E. Fratanduono, P. C. Myint, J. L. Belof, Y.-J. Kim, F. Coppari, J. H. Eggert, R. F. Smith, J. M. McNaney, D. M. Sterbentz, J. R. Rygg, and G. W. Collins, "Probing the Metastability Limit of Liquid Water Under Dynamic Compression."

A. V. Maximov, D. Turnbull, D. H. Edgell, J. G. Shaw, R. K. Follett, H. Wen, D. H. Froula, and J. P. Palastro, "Nonlinear Absorption of Multiple Laser Beams due to the Two-Plasmon–Decay Instability."

P. W. McKenty, M. J. Rosenberg, F. J. Marshall, D. R. Harding, R. S. Craxton, J. A. Marozas, T. J. B. Collins, R. Epstein, E. M. Campbell, S. Schiaffino, B. E. Blue, C. B. Yeamans, W. W. Hsing, C. Shuldberg, and M. Farrell, "Evaluation of Polar-Direct-Drive, Contoured-Shell Experiments at the National Ignition Facility."

B. McLellan and S. Zhang, "Kinetic Transition Pathway of Pressure Driven Structural Transformations: The Case of Magnesium Oxide."

D. I. Mihaylov, V. V. Karasiev, and S. X. Hu, "Progress in Development of Thermal Hybrid Exchange-Correlation Density Functionals for Improving the Description of Warm Dense Matter."

A. Milder, J. Katz, R. Boni, D. Nelson, D. Turnbull, J. P. Palastro, K. Daub, R. K. Follett, D. H. Froula, M. Sherlock,

T. Chapman, and W. Rozmus, "Measurements of Electron Distribution Functions in Laser-Produced Plasmas Using Angularly Resolved Thomson Scattering" (invited).

S. C. Miller, V. N. Goncharov, T. J. B. Collins, and J. Carroll-Nellenback, "A Study of 2D Internal Perturbation Evolution in Inertial Confinement Fusion Implosions."

Z. L. Mohamed, O. M. Mannion, C. J. Forrest, J. P. Knauer, and E. P. Hartouni, "Construction and Implementation of an Energy-Dependent Instrument Response Function for Accurate Analysis of Neutron Time-of-Flight Data."

K. L. Nguyen, A. M. Hansen, D. Turnbull, R. K. Follett, D. H. Froula, J. P. Palastro, L. Yin, and B. J. Albright, "Nonlinear Saturation of Cross-Beam Energy Transfer."

P. M. Nilson, F. J. Marshall, J. Kendrick, J. J. Ruby, D. A. Chin, D. Bishel, D. Guy, S. T. Ivancic, C. Stoeckl, R. F. Earley, D. R. Harding, M. Bedzyk, G. Gates, D. W. Jacobs-Perkins, V. N. Goncharov, T. J. B. Collins, and R. Epstein, "Imaging of Hydrodynamic Perturbation Evolution Using a Fresnel Phase Zone Plate."

J. P. Palastro, D. H. Froula, M. V. Ambat, R. Boni, E. M. Campbell, R. K. Follett, P. Franke, V. N. Goncharov, J. B. Oliver, D. Ramsey, J. L. Shaw, T. T. Simpson, D. Turnbull, H. Wen, S. Jolly, F. Quere, C. Benedetti, E. Esarey, G. Geddes, C. Schroeder, R. Bingham, S. Stoller, N. Vafaei-Najafabadi, G. Gregori, B. Malaca, A. Helm, J. Vieira, A. DiPiazza, A. Howard, K. Weichman, A. Arefiev, T. M. Antonsen, Jr., and Z. Li, "Laser–Plasma Interactions Driven by Spatiotemporally Structured Light Pulses" (invited).

D. Patel, R. Betti, K. M. Woo, V. Gopalaswamy, J. C. Carrol, and A. Bose, "Hydrodynamic Scaling Relations for OMEGA Cryogenic Implosions."

J. L. Peebles, J. R. Davies, D. H. Barnak, M. J. Bonino, T. Cracium, R. Betti, and P.-Y. Chang, "Axial Proton Radiography of Electric and Magnetic Fields Inside Laser-Driven Coils."

H. Poole, D. Cao, J. R. Rygg, S. X. Hu, I. E. Golovkin, T. Walton, R. Epstein, M. Kasim, S. Vinko, G. Gregori, and S. P. Regan, "A Feasibility Study of Using X-Ray Thomson Scattering to Diagnose the Plasma Conditions of Laser-Direct-Drive, DT Cryogenic Implosions."

P. B. Radha, W. Theobald, R. Betti, D. Cao, R. S. Craxton, C. J. Forrest, V. Yu. Glebov, V. N Goncharov, V. Gopalaswamy,

I. V. Igumenshchev, S. T. Ivancic, T. Joshi, J. P. Knauer, O. M. Mannion, F. J. Marshall, S. Miller, Z. L. Mohamed, D. Patel, S. P. Regan, H. G. Rinderknecht, T. C. Sangster, R. C. Shah, C. Stoeckl, C. A. Thomas, E. M. Campbell, M. Gatu Johnson, J. A. Frenje, and R. D. Petrasso, "Understanding the Performance of Polar-Drive Cryogenic Implosions on OMEGA."

D. Ramsey, P. Franke, T. T. Simpson, M. V. Ambat, D. H. Froula, and J. P. Palastro, "Vacuum Acceleration of Electrons in a Dynamic Laser Pulse."

S. P. Regan, W. Theobald, P. B. Radha, R. Betti, M. J. Rosenberg, R. S. Craxton, A. A. Solodov, A. Shvydky, K. S. Anderson, J. A. Marozas, T. J. B. Collins, V. N. Goncharov, D. Turnbull, E. M. Campbell, C. M. Shuldberg, R. W. Luo, R. Heredia, B. Bachmann, T. Döppner, M. Hohenberger, R. Scott, K. Glize, A. Colaïtis, and A. Casner, "Laser-Direct-Drive Energy-Coupling Experiments Using Spherical Solid-Plastic Targets at the National Ignition Facility."

H. G. Rinderknecht, J. P. Knauer, W. Theobald, R. Fairbanks, B. Brannon, V. Kobilansky, R. Peck, J. Armstrong, M. Weisbeck, J. Brown, P. B. Radha, S. P. Regan, J. Kunimune, P. J. Adrian, M. Gatu Johnson, J. A. Frenje, F. H. Séguin, and B. Bachmann, "Knock-on Deuteron Imaging of the Hot Spot and Compressed Fuel in Direct-Drive Cryogenic ICF Implosions."

M. J. Rosenberg, A. A. Solodov, A. R. Christopherson, R. Betti, P. B. Radha, C. Stoeckl, C. J. Forrest, V. Yu. Glebov, F. J. Marshall, S. P. Regan, T. J. B. Collins, D. H. Froula, J. P. Palastro, V. N. Goncharov, M. Hohenberger, B. Bachmann, G. N. Hall, P. Michel, and C. Kauland, "Hot-Electron Preheat in Hydrodynamically Scaled Direct-Drive Implosions at the National Ignition Facility and OMEGA."

J. J. Ruby, J. R. Rygg, D. A. Chin, C. J. Forrest, V. Yu. Glebov, C. Stoeckl, G. W. Collins, B. Bachmann, J. A. Gaffney, Y. Ping, N. V. Kabadi, and P. J. Adrian, "Bayesian Inference of Energy Transfer in Gigabar Convergent Experiments" (invited).

A. K. Schwemmlein, C. Stoeckl, W. T. Shmayda, C. J. Forrest, J. P. Knauer, S. P. Regan, and W. U. Schröder, "Controllable Target-Normal Sheath Acceleration Deuteron Beams Using Titanium Targets Toward Generating a Tritium Beam."

A. B. Sefkow, B. G. Logan, and J. H. Nuckolls, "Directly Driven Magnetized Targets with Steep Density Gradients for Inertial Fusion Energy."

R. C. Shah, S. X. Hu, I. V. Igumenshchev, J. Baltazar, D. Cao, C. J. Forrest, V. N. Goncharov, V. Gopalaswamy, D. Patel, W. Theobald, S. P. Regan, and F. Philippe, "In-Flight Shell Breakup in Direct-Drive DT Cryogenic Implosion."

J. L. Shaw, M. A. Romo-Gonzalez, G. Bruhaug, C. Dorrer, B. E. Kruschwitz, L. J. Waxer, M. V. Ambat, M. M. McKie, J. P. Palastro, D. H. Froula, N. Lemos, P. M. King, G. J. Williams, H. Chen, F. Albert, M. D. Sinclair, and C. Joshi, "Microcoulomb-Class Laser-Plasma Accelerator on OMEGA EP."

A. Shvydky, D. Haberberger, J. P. Knauer, S. X. Hu, S. T. Ivancic, J. Carroll-Nellenback, D. Cao, I. V. Igumenshchev, V. V. Karasiev, P. B. Radha, A. V. Maximov, S. P. Regan, T. C. Sangster, R. Boni, P. M. Nilson, V. N. Goncharov, D. H. Froula, M. D. Rosen, and V. A. Smalyuk, "Shock-Release Experiments on OMEGA EP."

T. T. Simpson, D. Ramsey, P. Franke, M. V. Ambat, D. Turnbull, D. H. Froula, J. P. Palastro, and N. Vafaei-Najafabadi, "Nonlinear Spatiotemporal Control of Laser Intensity."

A. A. Solodov, M. J. Rosenberg, M. Stoeckl, A. R. Christopherson, R. Betti, W. Seka, R. Epstein, C. Stoeckl, R. K. Follett, P. B. Radha, S. P. Regan, D. H. Froula, J. P. Palastro, V. N. Goncharov, J. F. Myatt, M. Hohenberger, B. Bachmann, and P. Michel, "Scaling and Mitigation of Hot-Electron Preheat in Polar-Direct-Drive Experiments at the National Ignition Facility."

Z. K. Sprowal, L. E. Crandall, J. R. Rygg, T. R. Boehly, D. N. Polsin, G. W. Collins, D. G. Hicks, and P. M. Celliers, "Double Shock Compression in Polystyrene to ~8 Mbar."

C. Stoeckl, M. J. Bonino, C. Mileham, S. P. Regan, W. Theobald, T. Ebert, and S. Sander, "Optimization of a Short-Pulse–Driven Si He$_\alpha$ Soft X-Ray Backlighter."

W. Theobald, P. B. Radha, S. P. Regan, K. S. Anderson, R. Betti, E. M. Campbell, D. Cao, R. S. Craxton, C. J. Forrest, V. Yu. Glebov, V. N. Goncharov, V. Gopalaswamy, I. V. Igumenshchev, T. Joshi, S. T. Ivancic, J. P. Knauer, A. Lees, O. M. Mannion, F. J. Marshall, M. Michalko, Z. L. Mohamed, D. Patel, R. C. Shah, C. Stoeckl, C. A. Thomas, and M. Gatu Johnson, "OMEGA Subscale Cryogenic Implosions in Symmetric and Polar-Direct-Drive Beam Geometry."

C. A. Thomas, D. Cao, W. Theobald, R. Betti, K. S. Anderson, K. A. Bauer, E. M. Campbell, A. R. Christopherson, T. J. B. Collins, R. S. Craxton, D. H. Edgell, R. Epstein, C. J. Forrest,

V. Yu. Glebov, V. Gopalaswamy, I. V. Igumenshchev, S. T. Ivancic, D. W. Jacobs-Perkins, R. T. Janezic, T. Joshi, J. P. Knauer, J. Kwiatkowski, A. Lees, O. M. Mannion, F. J. Marshall, M. Michalko, Z. L. Mohamed, D. Patel, J. L. Peebles, P. B. Radha, S. P. Regan, H. G. Rinderknecht, M. J. Rosenberg, S. Sampat, T. C. Sangster, R. C. Shah, C. Stoeckl, and V. N. Goncharov, "Quantifying the Effects of Scale and Illumination Geometry in Laser Direct Drive."

D. Turnbull, A. V. Maximov, D. Cao, A. R. Christopherson, D. H. Edgell, R. K. Follett, V. Gopalaswamy, J. P. Knauer, J. P. Palastro, A. Shvydky, C. Stoeckl, H. Wen, and D. H. Froula, "Impact of Spatiotemporal Smoothing on the Two-Plasmon–Decay Instability."

P. Tzeferacos, R. Betti, J. R. Davies, F. Garcia-Rubio, E. C. Hansen, D. Michta, C. Ren, A. C. Reyes, W. Scullin, A. B. Sefkow, J. G. Shaw, H. Wen, and K. M. Woo, "A Simulation Resource Team for Innovative Fusion Concepts in the BETHE Program."

W. Y. Wang and R. S. Craxton, "A Proposal for Spherical Hohlraum Experiments on OMEGA Using Seven Laser Entrance Holes."

H. Wen, R. K. Follett, A. V. Maximov, D. H. Froula, J. P. Palastro, and F. S. Tsung, "Kinetic Inflation of Stimulated Raman Scattering Driven by a Broadband Frequency-Modulated Laser Pulse."

K. M. Woo and R. Betti, "Impact of Low-Mode Areal Density Asymmetry on Loss of Confinement for Igniting Capsules."

S. Zhang and S. X. Hu, "Large-Scale Molecular-Dynamics Studies on the Release of Shocked Polystyrene Under Inertial Confinement Fusion Conditions."

Y. Zhang, C. Ren, J. R. Davies, and P. Heuer, "Kinetic Simulation Study of Magnetized Collisionless Shock Formation Using OMEGA EP."

———————

M. Sharpe, W. T. Shmayda, J. Wermer, and C. A. Bond, "Permeation of Isotopes through FeCrAl Alloys," presented at Technology of Fusion Energy (TOFE) 2020, virtual, 15–19 November 2020.

———————

D. H. Froula, "Progress in Flying Focus," presented at High-Intensity Lasers and High-Field Phenomena, virtual, 16–20 November 2020 (invited).

———————

B. E. Ugur and K. L. Marshall, "Computational Modeling and Design of Liquid Crystal Materials for Applications in the Terahertz Regime," presented at the 2020 American Institute of Chemical Engineers Annual Meeting, virtual, 16–20 November 2020.

———————

M. S. Wei, "OMEGA EP Laser Facility," presented at the LaserNetUS Town Hall, virtual, 19 November 2020.

———————

The following presentations were made at the Office of Experimental Science, FY2021 Annual Program Review, virtual, 1–3 December 2020:

E. M. Campbell, "ICF Facility Operations—LLE 10.7."

S. P. Regan, "ICF Diagnostics and Instrumentation: LLE."

T. C. Sangster, "LLE MTE 10.8."

———————

The following presentations were made at the Advanced Accelerator Concepts Seminar Series, virtual, 2 December 2020:

P. Franke, J. P. Palastro, J. L. Shaw, D. Ramsey, T. T. Simpson, M. V. Ambat, K. Daub, J. B. Oliver, R. Boni, C. Dorrer, J. Katz, and D. H. Froula, "Dephasingless Laser Wakefield Acceleration."

J. L. Shaw, M. A. Romo-Gonzalez, G. Bruhaug, C. Dorrer, B. E. Kruschwitz, L. J. Waxer, M. V. Ambat, M. M. McKie, J. P. Palastro, D. H. Froula, N. Lemos, P. M. King, G. J. Williams, H. Chen, F. Albert, M. D. Sinclair, and C. Joshi, "Microcoulomb-Class Laser-Plasma Accelerator on OMEGA EP."

———————

G. W. Collins, M. Zaghoo, M. Hiuff, L. Crandall, G. Tabak, B. J. Henderson, X. Gong, D. A. Chin, Z. K. Sprowal, J. J. Ruby,

M. K. Ginnane, P. M. Nilson, D. N. Polsin, M. Marshall, J. R. Rygg, and R. Jeanloz, "Exploring Extrasolar Planets in the Laboratory," presented at the American Geophysical Union Fall Meeting, virtual, 7–11 December 2020.

———————

E. M. Campbell, "Direct-Drive Laser Fusion: Status, Plans, and the Future," presented at the Freeman Dyson Seminar, virtual, 10 December 2020.

———————

The following presentations were made at the 23rd Topical Conference on High-Temperature Plasma Diagnostics, virtual, 13–17 December 2020:

D. H. Barnak, J. R. Davies, J. P. Knauer, and P. M. Kozlowski, "Soft X-Ray Spectrum Unfold of K-Edge–Filtered X-Ray Diode Arrays Using Cubic Splines."

D. T. Bishel, E. V. Marley, M. B. Schneider, D. A. Liedahl, R. F. Heeter, M. E. Foord, G. E. Kemp, Y. Frank, J. A. Emig, G. Perez-Callejo, J. R. Rygg, G. W. Collins, and P. M. Nilson, "Open L-Shell Spectroscopy of Nonlocal Thermodynamic Equilibrium Plasmas."

D. H. Edgell, A. Hansen, J. Katz, D. Turnbull, and D. H. Froula, "Unabsorbed Light Beamlets for Diagnosing Coronal Density Profiles and Absorption Nonuniformity in Direct-Drive Implosions on OMEGA."

S. T. Ivancic, W. Theobald, C. Sorce, M. Bedzyk, F. J. Marshall, C. Stoeckl, R. C. Shah, M. Lawrie, S. P. Regan, T. C. Sangster, E. M. Campbell, T. J. Hilsabeck, K. Englehorn, J. D. Kilkenny, T. M. Chung, J. D. Hares, A. K. L. Dymoke-Bradshaw, P. Bell, J. Celeste, A. C. Carpenter, M. Dayton, D. K. Bradley, M. C. Jackson, E. Hurd, L. Pickworth, S. R. Nagel, G. Rochau, J. Porter, M. Sanchez, L. Claus, G. Robertson, and Q. Looker, "Improving Time-Resolved X-Ray Hot-Spot Image Fidelity with Composite Imaging Using a Multiple Pinhole Imager."

J. Katz, D. Turnbull, B. E. Kruschwitz, A. Rigatti, R. Rinefierd, and D. H. Froula, "A Transmitted Beam Diagnostic for the Wavelength Tunable UV Drive Beam on OMEGA."

O. M. Mannion, C. J. Forrest, V. Yu. Glebov, I. V. Igumenshchev, S. T. Ivancic, D. W. Jacobs-Perkins, J. P.

Knauer, Z. L. Mohamed, S. P. Regan, H. G. Rinderknecht, R. C. Shah, C. Stoeckl, W. Theobald, K. M. Woo, J. A. Frenje, M. Gatu Johnson, and A. J. Crilly, "Diagnosing 3-D Asymmetries in Laser-Direct-Drive Implosions on OMEGA" (invited).

F. J. Marshall, S. T. Ivancic, C. Mileham, P. M. Nilson, J. J. Ruby, C. Trejan, J. Kendrick, B. S. Schiener, and M. J. Schmitt, "High-Resolution X-Ray Radiography with Fresnel Zone Plates at the University of Rochester's OMEGA Laser Systems" (invited).

Z. L. Mohamed, O. M. Mannion, J. P. Knauer, C. J. Forrest, V. Yu. Glebov, and C. Stoeckl, "Application of an Energy-Dependent Instrument Response Function of nTOF Data from DT Cryogenic DT Experiments."

M. J. Rosenberg, T. Filkins, R. E. Bahr, R. Jungquist, M. Bedzyk, S. P. Regan, J. Hernandez, N. Butler, G. Swadling,

J. Eichmiller, R. Sommers, P. Nyholm, P. Datte, and J. S. Ross, "SLTD: A Time-Resolved Scattered-Light Diagnostic Array at the National Ignition Facility."

———————

S. Zhang, R. Paul, and M. A. Morales, "Benchmarking Phase Transitions in Periclase Under Multi-Megabar Pressures," presented at the American Geophysical Union Fall Meeting, virtual, 16 December 2020.

———————

E. M. Campbell, "Laboratory for Laser Energetics Update," presented at the Fusion Power Associates 41st Annual Meeting and Symposium, virtual, 16–17 December 2020.